ELECTRIC DIPOLE MOMENTS, CLUSTER METALLICITY, AND THE MAGNETISM OF RARE EARTH CLUSTERS

A Thesis
Presented to
The Academic Faculty

by

John Bowlan

In Partial Fulfillment
of the Requirements for the Degree
Doctor of Philosophy in the
School of Physics

Georgia Institute of Technology
August 2010

ELECTRIC DIPOLE MOMENTS, CLUSTER METALLICITY, AND THE MAGNETISM OF RARE EARTH CLUSTERS

Approved by:

Walter A. de Heer, Committee Chair
School of Physics
Georgia Institute of Technology

Walter A. de Heer, Advisor
School of Physics
Georgia Institute of Technology

Mei-Yin Chou
School of Physics
Georgia Institute of Technology

Robert L. Whetten
School of Physics and School of Chemistry & Biochemistry
Georgia Institute of Technology

Mostafa El-Sayed
School of Chemistry & Biochemistry
Georgia Institute of Technology

Phillip First
School of Physics
Georgia Institute of Technology

Date Approved: 28 April 2010

DEDICATION

This thesis is dedicated to my Mother and Father

ACKNOWLEDGEMENTS

I acknowledge the assistance of many people during my years in graduate school. Thanks to: My advisor Walt de Heer for tirelessly running the lab and providing the essential background ideas for this work. I deeply admire his empirical approach to physics. Xiaoshan Xu and Shuangye Yin both provided me with detailed training on running experiments and data analysis. Much of the work on sodium must be credited to Anthony Liang who was a close colleague. I thank my committee members for agreeing to participate in my thesis defense. I also acknowledge Walt de Heer, Philippe Poncharal, Patrice Keghelian, Ramiro Moro and others, for the development of the early stages of the experimental apparatus. Andrei Kirilyuk and Chris van Dijk made important contributions to the rhodium and rare-earth magnetism experiments. I acknowledge Robert Whetten, Mei-Yin Chou, André Fielicke, Hannu Häkkinen, James Bradshaw, Domenico Lippolis, John Papapolymerou, and Guy Lebanon for many helpful discussions on clusters and other topics of interest. I acknowledge the staff of the CoS and GTRI machine shops, especially Sam Mize, for their patience and insight. I also thank the staff of the School of Physics: Felicia Goolsby, Keith Garner, Debbie James, Valera Pate, Samantha King, and others. Finally, I thank my best friend and wife Pamela for her constant advice and support.

TABLE OF CONTENTS

LIST OF TABLES

LIST OF FIGURES

SUMMARY

One of the fundamental properties of bulk metals is the cancellation of electric fields. The free charges inside of a metal will move until they find an arrangement where the internal electric field is zero. This implies that the electric dipole moment of a metal particle should be exactly zero, because an electric dipole moment requires a net separation of charge and thus a nonzero internal electric field.

This thesis is an experimental study to see if this property continues to hold for tiny sub-nanometer metal particles called clusters (2 - 200 atom, $R < 1$ nm). We have measured the electric dipole moments of metal clusters made from 15 pure elements using a molecular beam electric deflection technique. We find that the observed dipole moments vary a great deal across the periodic table. Alkali metals have zero dipole moments, while transition metals and lanthanides all have dipole moments which are highly size dependent. In most cases, the measured dipole moments are independent of temperature (T = 20 - 50 K), and when there is a strong temperature dependence this suggests that there is a new state of matter present. Our interpretation of these results are that those clusters which have a non-zero dipole moment are non-metallic, in the sense that their electrons must be localized and prevented from moving to screen the internal field associated with a permanent dipole moment.

This interpretation gives insight to several related phenomena and applications. We briefly discuss an example cluster system Rh_N where the measured electric dipole moments appear to be correlated with a the N_2O reactivity.

Finally, we discuss a series of magnetic deflection experiments on lanthanide clusters (Pr, Ho, Tb, and Tm). The magnetic response of these clusters is very complex and highly sensitive to size and temperature. We find that Pr_N (which is non-magnetic in the bulk)

becomes magnetic in clusters and Tm_N clusters have magnetic moments lower than the atomic value as well as the bulk saturation value implying that the magnetic order in the cluster involves non-collinear or antiferromagnetic order. Ho_N and Tb_N show very similar size dependent trends suggesting that these clusters have similar structures.

CHAPTER I

INTRODUCTION

One of the fundamental properties of bulk metals is the cancellation of electric fields. The free charges inside of a metal will move until they find an arrangement where the internal electric field is zero. This implies that the electric dipole moment of a metal particle should be exactly zero, because an electric dipole moment requires a net separation of charge and thus a nonzero internal electric field. Is there a lower size limit, below which this property no longer holds? This thesis is an experimental study to see if this property continues to hold for tiny sub-nanometer metal particles called clusters (2 - 200 atom, $R < 1$ nm)

1.1 Overview of Cluster Physics

A fundamental theme of metal cluster research [39] is the emergence of bulk properties as a material is constructed one atom at a time. This line of research has provided valuable insights into the emergence of bulk and surface properties such as the work function [132, 76, 140, 160], optical plasma resonances [143, 142, 165, 42, 99], electronic band structure [100, 98, 163, 148, 30, 104, 7], and ferromagnetism [12, 13, 89, 36] to name a few of many examples.

Molecular beam experiments on free metal clusters allow the physical properties of clusters to be studied in an environment free of interactions, and mass spectroscopy enables the physical properties to be studied as an explicit function of the number of atoms.

These experimental investigations have found that clusters also have many properties which cannot be simply extrapolated from bulk or surface properties. Many of these effects such as the shell structure (first identified in alkali clusters [92, 120]) involve an interaction between the confinement quantization of the electronic states [94] and the degeneracy due to the near spheroidal symmetry of the clusters. These shell filling effects have been

observed in other elements and provide an elegant condensed matter manifestation of a phenomenon familiar from atomic and nuclear physics.

Another complementary approach to cluster physics emphasizes the strong size dependence and structural properties of clusters. This line of research typically involves a close comparison between quantum chemical calculations and experiment [70, 84, 63, 54, 62, 52, 173, 69, 131, 117, 116, 166, 156, 157]. Much of this work is motivated by the potential for applications of size-selected metal clusters to catalysis or magnetic storage.

1.2 Cluster Metallicity

1.2.1 The Bulk Metallic State

We will quickly review the properties of bulk metals and review some simple models used to account for their properties in the quantum theory of solids. Most of this material is taken from textbooks and reviews on the topic [6].

Metals have high electrical conductivity (10^7 S/m for Au), high thermal conductivity, are highly reflective in the infrared and visible regions of the spectrum, and are mostly paramagnetic (with the exception of Fe, Co, and Ni). The strength of their bonding and binding energies varies a great deal. Sodium metal can be cut with a kitchen knife and melts at 370 K, while tungsten can remain solid up to temperatures of 3695 K, second only to carbon among the pure elements. Thus, the melting points of metals can vary by a factor of 10!

Many of these physical properties can be explained qualitatively by a model which describes a metal as a gas of delocalized electrons moving freely in a crystal lattice. Because the density of the valence electrons is very large, it is necessary to account for the effects of the Pauli exclusion principle and Fermi-Dirac statistics. In this model the free electron states are filled one-by-one up to an energy E_F called the Fermi energy. The electronic properties (e.g. electrical and thermal conductivity, paramagnetism) are dominated by the

contribution of the electronic states near E_F, because unoccupied electronic states are accessible to the these electrons with thermal energies.

The structure and symmetry of the ionic lattice plays also has an essential role by scattering the electrons. Destructive interference from this scattering opens gaps in the electronic dispersion (k vs. E), and scattering from lattice vibrations is one of the major contributions to the electrical resistivity.

The free electron picture described above is most effective for metals whose valence electrons are strongly delocalized, such as alkali and noble metals (Cu, Ag, and Au). Many of the valence electrons in transition metals are derived from d orbitals, and they show evidence of partial localization. The wavefunctions for these states can be better described as a linear combination of the atomic orbitals which are localized on individual lattice sites. This point of view (which also applies to non-metals) has been elegantly described by Hoffmann [74], and is of great utility in the study of surfaces. In this picture the bands of electronic states come from the splitting of overlapping atomic orbitals. The bandwidth of a band increases with the overlap, and thus strongly delocalized electrons are associated with very broad electronic bands, while localized electronic states inhabit crowded narrow peaks in the density of states.

In the band theory, the essential difference between a metal and an insulator is determined by electron counting. A crystal with a partially filled electronic band has unoccupied electronic states infinitesimally close to E_F and so these electrons are free to move in response to voltage and thermal gradients. This picture fails in some cases because the band theory doesn't account for the mutual interaction of electrons[113], or instabilities of the crystal lattice to distortions which can open gaps at E_F.

In classical electromagnetism a metal is defined to be a region of space where the electric field is zero ($E = 0$). What is the motivation behind this definition?

If we assume that a material is electrically neutral overall but consists of a equal numbers of positive and negative charges that are free to move throughout the volume, then we

can write an equation of motion for the charges using Maxwell's equations

$$\nabla \cdot E = \rho/\epsilon_0 \tag{1.1}$$

$$\nabla \cdot j = \frac{\partial}{\partial t}\rho \tag{1.2}$$

Now if we use the constitutive relation $j = \sigma E$ (Ohm's law which relates the current to the electric field then we find that

$$\frac{\partial}{\partial t}\rho = \nabla \cdot (\sigma E) \tag{1.3}$$

$$\frac{\partial}{\partial t}\rho = -\frac{\sigma}{\epsilon_0}\rho \tag{1.4}$$

Thus the charge density approaches zero exponentially with a time constant equal to σ/ϵ_0. How rapid is this decay? For typical values of σ and ϵ the excess charge will decay with in *femtoseconds* .

1.2.2 What Definition of Metal is Appropriate for a Cluster?

The properties discussed in the previous section which were most strongly associated with bulk metallicity - the delocalization, the electrical and thermal conductivity, the optical reflectance, the specific heat. Not all of these can be practically measured for a free cluster in a beam, so there is a need for a simple experimental test for metallic behavior. The distinction is not just of idle interest. There is some evidence (see chapter 4) that the metal non-metal distinction carries real implications for the chemical activity of metal clusters [95].

We give several examples of different experimental attempts to characterize the metallic state of finite cluster systems. The experimental record is definitely mixed. We first discuss attempts to define cluster metallicity based on band gaps determined from photoelectron spectroscopy. Then we discuss tests for metallicity based on the screening property of metals.

1.2.3 Cluster Metallicity from Band Gaps

The Fermi energy E_F depends only on the density of valence electrons. It is thus an intensive physical quantity that is independent of the size of a metal cluster. Since the electron density of metal clusters is very close to that of bulk materials, the Fermi energy should be the same. If there are only N valence electrons, this implies that the average energy gap between the single electron energy levels should scale as E_F/N or E_F/R^3. If the electronic levels are uniformly distributed between 0 and E_F then every electronic level will have a gap of this size to its neighbors.

Thus every cluster should be considered an insulator, because every cluster should have a finite energy-gap at E_F, due to the discreteness of the electronic energy levels.

Von Issendorff and Cheshnovsky proposed [153] that a cluster should be considered a metal if the experimentally measured energy gap at E_F is less than the Kubo gap [94], and an insulator if the gap is larger. They measure the gaps using anion photoelectron spectroscopy, which is a direct probe of the density of states and thus the band gap. The choice of the Kubo gap is simple, but beyond this there isn't much motivation for it. The pattern in the data is very clear for the case of mercury clusters, but the metal / nonmetal distinction is not clear for the other cases. Other groups have studied metals with similar results[148].

Band gaps are an apparently attractive criteria for metallicity because of the clear connection with bulk metallicity. They are also practical to measure experimentally using anion photoelectron spectroscopy. The review article [153] summarizes the evidence gathered over many years of experimental work on cluster systems made of a variety of different elements. For most elements the band gap oscillations above and below the Kubo gap with size and there is no clear size where a metal to insulator transition takes place.

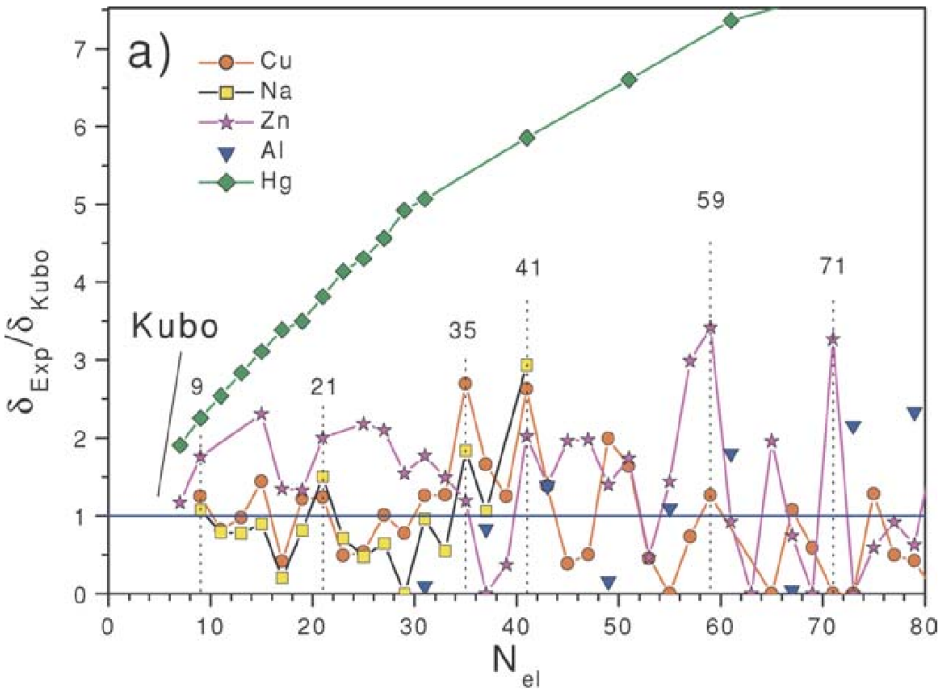

Figure 1.1: Experimentally measured band gaps from anion photoelectron spectroscopy for Cu, Na, Zn, Al, and Hg. From von Issendorff and Cheshnovsky [153]. The measured gaps are compared with the Kubo band gap. Materials where the band gap is larger than the Kubo gap are considered to be insulators and those with a smaller gap are considered metallic. With the exception of Hg there are no smooth trends and metallicity, by this definition, is size dependent.

1.2.4 Cluster Metallicity from Screening

Defining metallicity by the size of gaps in the spectrum doesn't seem to give a clear picture of the emergence of the metallic state. (with the exception of Hg) The plot in the previous section shows that the experimentally measured band gaps are highly size dependent and they oscillate around the Kubo gap.

An alternative to band-gaps and anion photoelectron spectroscopy is to define a metal as a sample of matter which screens electric fields so that $E = 0$ everywhere in its interior. There have been several proposed ideas to test cluster metallicity by experimentally measuring the screening as a function of cluster size. It is interesting to see if they give consistent answers.

1.2.5 Dipole Moments and Internal Fields

How can we test to determine if the internal electric field is zero? A nonzero internal electric field implies a separation of charge and therefore an electric dipole moment. An electric dipole moment can be measured in a molecular beam deflection experiment described below.

Figure 1.2 illustrates the relationship between the dipole moment and internal electric field.

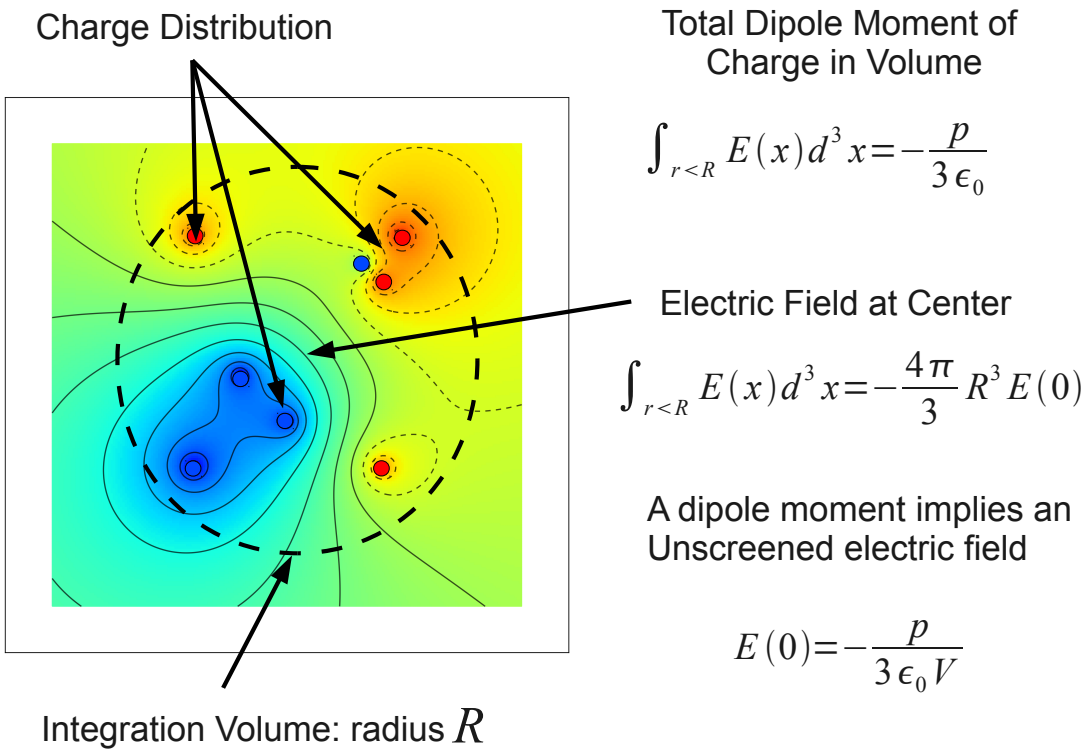

Figure 1.2: Relationship between the dipole moment of the charge contained in the region of space and the internal electric field at the center of the region

1.2.6 Core-Hole Screening vs. Dipole Measurements

The first test for metallicity is based on the screening of a core-hole [144]. A high energy 20 eV photon is directed at a beam of size selected Pb cluster anions. The 20 eV photon neutralizes the Pb cluster by removing a 5d electron. The 5d electron is localized on one atomic site, so the delocalized 6s valence electrons will quickly move to screen the localized charge. If the core hole is perfectly screened then the kinetic energy distribution of the emitted photoelectrons should reflect the work done against the image charge to remove them from the cluster (which is modeled as a metal sphere) $E = -\frac{1}{2}\frac{e^2}{R}$

The experimental result is shown in Figure 1.3. The photoelectrons show serious divergences from the prediction of the metal sphere model for sizes smaller than $N = 20$. Which suggests that sizes larger than this are able to effectively screen the core-hole and thus are metallic.

The second test for metallicity is the measurement of the electric dipole moment in an electric deflection experiment due to Schäfer et. al. [134]. The results of the measure (plotted as dipole moment per atom are shown in Figure 1.3. Pb clusters show electric dipole moments on the order of 0.01 D / atom, up to sizes as large as $N = 40$ and there is little sign that the dipole moments are converging to zero as would be expected for a metallic sphere.

Which criteria more accurately captures the essence of a metal? Both the electron affinity (of an unscreened core hole) and the electric dipole moment can have implications for cluster chemistry. The apparent contradiction between these two experimental results will be interesting to resolve!

1.3 Background on Molecular Beam Cluster Experiments

Much of the detailed knowledge we have about the behavior of atoms and molecules is derived from molecular beam experiments, like the two described above. While the apparatus looks sophisticated and has evolved over 100 years, at the core a molecular beam is

nothing more than a controlled leak into a vacuum system.

The laboratory of Otto Stern was the first to use the molecular beam method to measure the distribution of speeds followed by gas molecules. This experimental work confirmed the correctness of the theory of Maxwell and Boltzmann.

Next the method was famously used by Stern and Gerlach to demonstrate "space quantization". They showed that a beam of silver atoms projected through an inhomogeneous magnetic field deflected into two discrete directions rather than the continuous distribution of deflections which was predicted from the classical theory of the atom. This experiment was historically significant as it was the first proof of the quantization of angular momentum.

Another milestone was the laboratory of I.I. Rabi at Columbia university in the 1920's who demonstrated the molecular beam magnetic resonance method. Rabi and his colleagues were able to use magnetic fields oscillating at radio-frequencies to excite transitions between the discrete states demonstrated in Stern and Gerlach's laboratory. This method was refined and used to make precise measurements of nuclear magnetic moments.

Lamb and Retherford used an experimental setup very similar to Rabi's, combined with an electron bombardment source to measure the fine structure of the Hydrogen atom. This demonstration that the g-factor of the electron was slightly less than 2, was very significant for theoretical and particle physics.

Ramsey improved the resolution of Rabi's method by introducing the separated oscillating field method, this enabled high precision measurements of the nuclear magnetic moments and was until recently the foundation of the cesium atomic clock.

In the present molecular beams continue to be of importance for reactive scattering experiments and there has been remarkable recent progress in the slowing and trapping of neutral polar molecules.

The experimental techniques that apply molecular beams to the study of metal clusters are discussed in the next chapter.

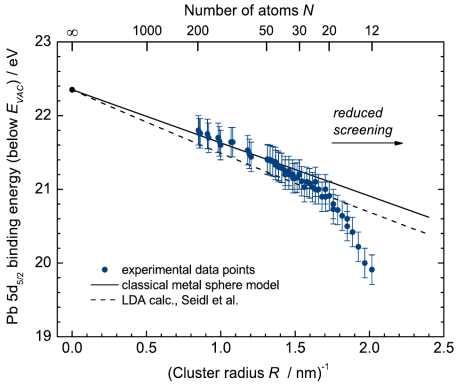

(a) Kinetic energy of photoelectrons emitted from core levels of Pb anion clusters. From an experiment with 200 eV laser FLASH. [144]

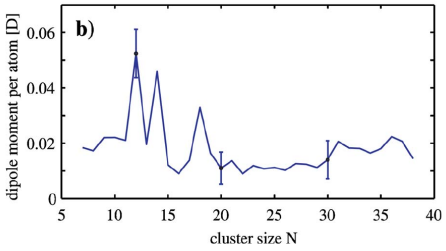

(b) Electric dipole moments of Pb clusters measured from an electric deflection experiment of Schäfer et. al. [134]

Figure 1.3: Comparison between two alternative measures of cluster metallicity based on screening. The first graph shows the result of an experiment to measure the efficiency of core hole screening. A 200 eV free-electron-laser removes a 5d core electron from a lead anion cluster. The detached cluster is neutralized and if the cluster is metallic then the valence electrons should efficiently screen the core hole. The screening of the core hole is determined by measuring the kinetic energy distribution of the detached electron.

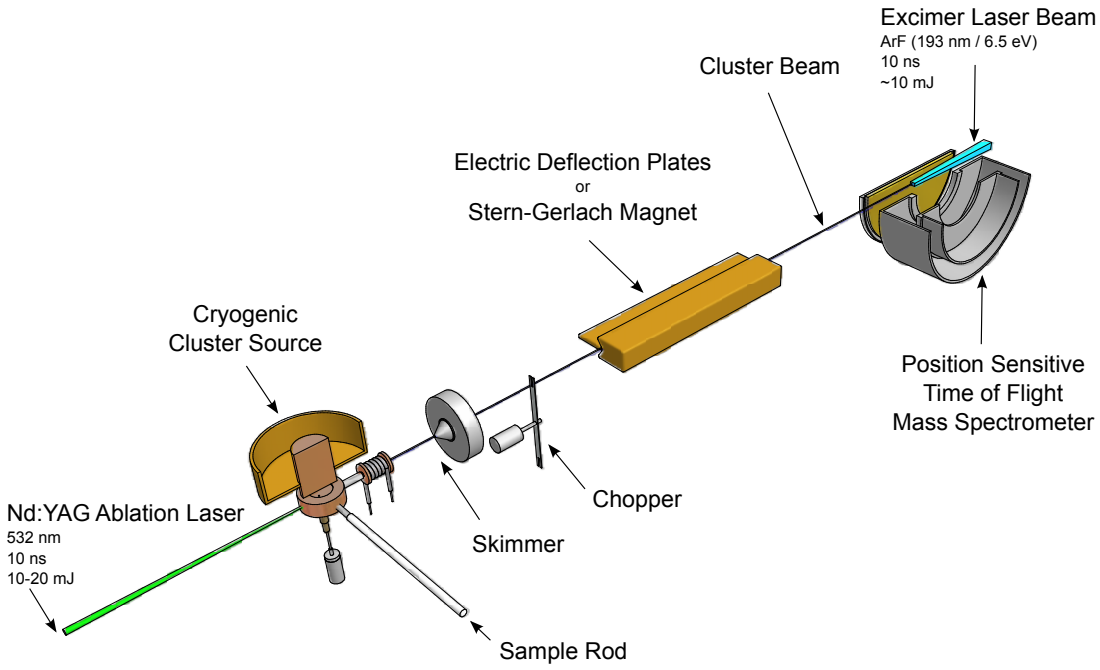

Figure 1.4: Schematic illustrating the elements of a molecular beam deflection experiment. The clusters are produced by laser ablation in a cryogenically cooled cluster source. The cluster leave the source in a gas-expansion into a vacuum and are extracted by a skimmer. Synchronization with mechanical chopper allows measurement of the beam's velocity. The beam passes through the plates of an electric deflector or Stern-Gerlach magnet and the clusters are deflected. The clusters are ionized by a UV laser pulse from an excimer laser, and are separated by mass in a time-of-flight mass spectrometer. The sensitivity of the mass spectrometer to the position of the ion in the ionization volume allows for the deflections to be measured.

CHAPTER II

EXPERIMENTAL METHODS

In this chapter, we discuss the details of the experimental methods used to measure the electric and magnetic dipole moments of metal clusters. It is important to understand how the clusters are produced by laser vaporization, and why we believe that the clusters are in thermal equilibrium with the source. These points are crucial for the correct interpretation of the experiments.

2.1 Molecular Beam Machine

An illustration of the cluster beam machine is shown in Figures 2.1, and 2.2. Compared with the simple schematic of the molecular beam experiment shown in the first chapter (Figure 1.4) we see that a lot of extra equipment is required to for a molecular beam experiment. During an experiment the pressure in the cluster source chamber is maintained at 10^{-3} Torr, the pressure in the electric and magnetic deflection chambers is 10^{-6} Torr, and the pressure in the TOF mass spectrometer is 10^{-9} Torr. Maintaining this pressure difference against the constant pulsed flux of He gas from the beam requires many stages of differential pumping. The cluster chamber itself is pumped by a 140 L/s dual stage roots pump. The rest of the chambers are differentially pumped by 500 L/s turbo pumps. After including the oil-sealed vane pumps which provide backing vacuum for the turbo pumps the apparatus contains 9 vacuum pumps.

2.1.1 Cluster Source

2.1.1.1 Background on Growth of Clusters

Metals in thermal equilibrium at room temperature will be in the solid state. Thus metal clusters have a strong tendency to aggregate. In order to isolate and study metal clusters

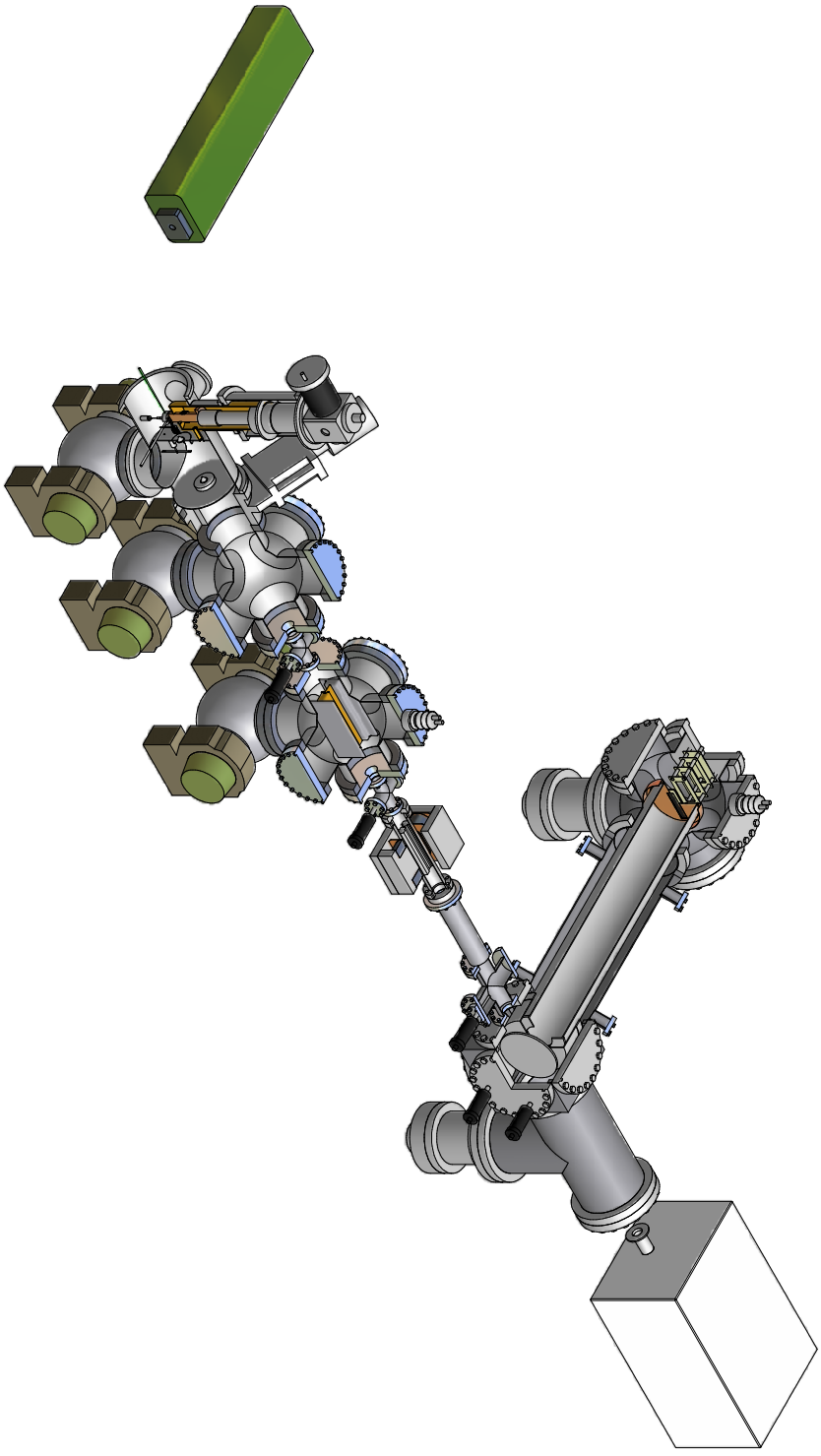

Figure 2.1: Orthoview of the cluster beam machine

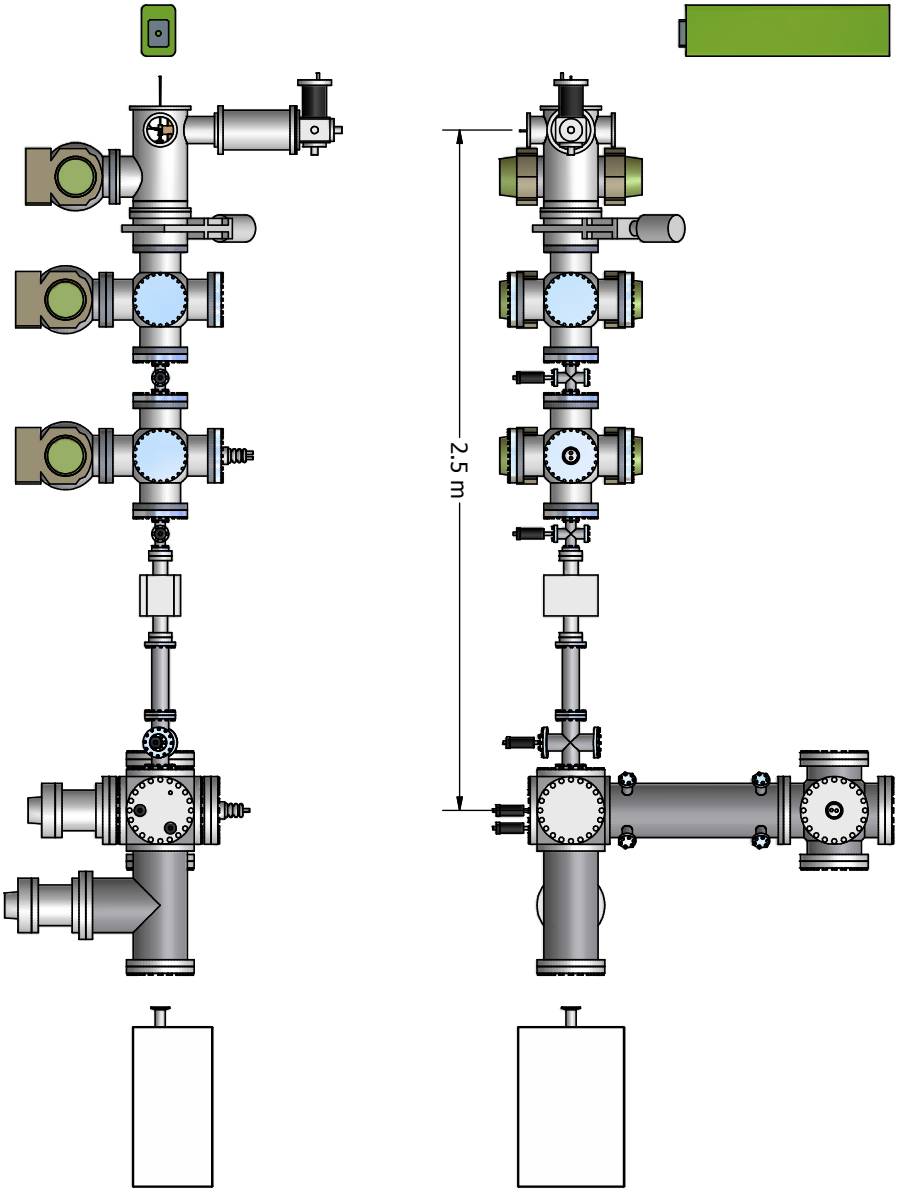

Figure 2.2: Profile view of the cluster beam

the process of growth and aggregation must be interrupted and the clusters must be isolated and passivated before the growth of the bulk material is complete.

Growth of metal clusters takes place at the boundary of the transition between the vapor phase and the condensed phase (solid or liquid). If the partial pressure of metal vapor exceeds the saturation vapor pressure then the metal vapor will condense into the solid or liquid bulk phases. This condensation takes place through a non-equilibrium process of nucleation and aggregation which can described by a variety of kinetic models with varying levels of realism [145]. This nucleation process is generic and it also occurs in the growth of clouds [8], surface monolayers, and magnetic domains [9]. (see ref. [145] for a modern treatment)

Every cluster growth method has the following ingredients:

1. Production of a supercritical vapor of monomers

2. Nucleation and growth of clusters

3. Isolation of growing clusters

Alkali metals and some other materials (e.g. Bi) have low melting points (370 K for Na) and a significant vapor pressure can be produced by heating a sample of alkali metal with a resistive tungsten filament. It is impractical (but not impossible) to produce clusters of harder transition metals in this way because it is very difficult to design a crucible which can contain the material when it is heated to the 3000 K temperatures needed for cluster growth. For these materials, it is preferable to produce the metal vapor by other methods which quickly deposit a large amount of energy onto the target material - either sputtering of vapor by collision with an energetic beam of charged particles, vaporization of monomers in an arc discharge, or intense local heating with a short laser pulse.

The metal vapor produced by these methods is so hot that many of the atoms are doubly or triply ionized. This metal plasma must be cooled to enable the growth of clusters. This cooling can be accomplished by quenching the metal plasma in an inert buffer gas

(He or Ar). The collisions of the metal vapor and growing clusters with the buffer gas atoms removes the heat of condensation from the cluster and thus inhibits re-evaporation of monomers.

2.1.1.2 Laser Vaporization Source

In our experiments, metal clusters are produced by the laser vaporization method. This method was pioneered by [43, 18]. Milani and de Heer [109] improved this source in several ways, and our implementation of the source is illustrated in Figure 2.3.

The principle of a laser vaporization source is simple: A small target of metal is ablated by a 10 ns pulse from a doubled Nd:YAG laser (532 nm, 30 mJ / pulse). The hot metal plasma expands into a flow of cryogenically cooled He gas, and the metal condenses into clusters. The He / cluster mixture expands through a nozzle into a vacuum, and a beam is extracted from the centerline of the expansion by multiple stages of skimming and differential pumping. The source temperature (15 - 60 K) determines the population of the energy levels of the clusters in the beam. Once a cluster leaves the source it is isolated from any heat bath and thus each individual cluster is a microcanonical ensemble with fixed total energy and angular momentum.

The clusters dwell in the source chamber for a time on the order of 1-3 ms. During this dwell time the clusters experience millions of collisions with the He buffer gas and come to thermal equilibrium with it. The expansion of the cluster/gas mixture into the vacuum can also cool the clusters even further. It is known from experiments with molecular beams formed in supersonic jets, that the cooling from expansion is more effective for rotations and translations that it is for vibrations. This is mostly due to the fact that a cluster has only 3 rotational degrees of freedom while there are 3N vibrational normal modes. The diameter of the nozzle is 1-2 mm, and the backing pressure of He is 3 bar at room temperature. Under these conditions the expansion into the vacuum is not supersonic, so little rotational cooling is expected.

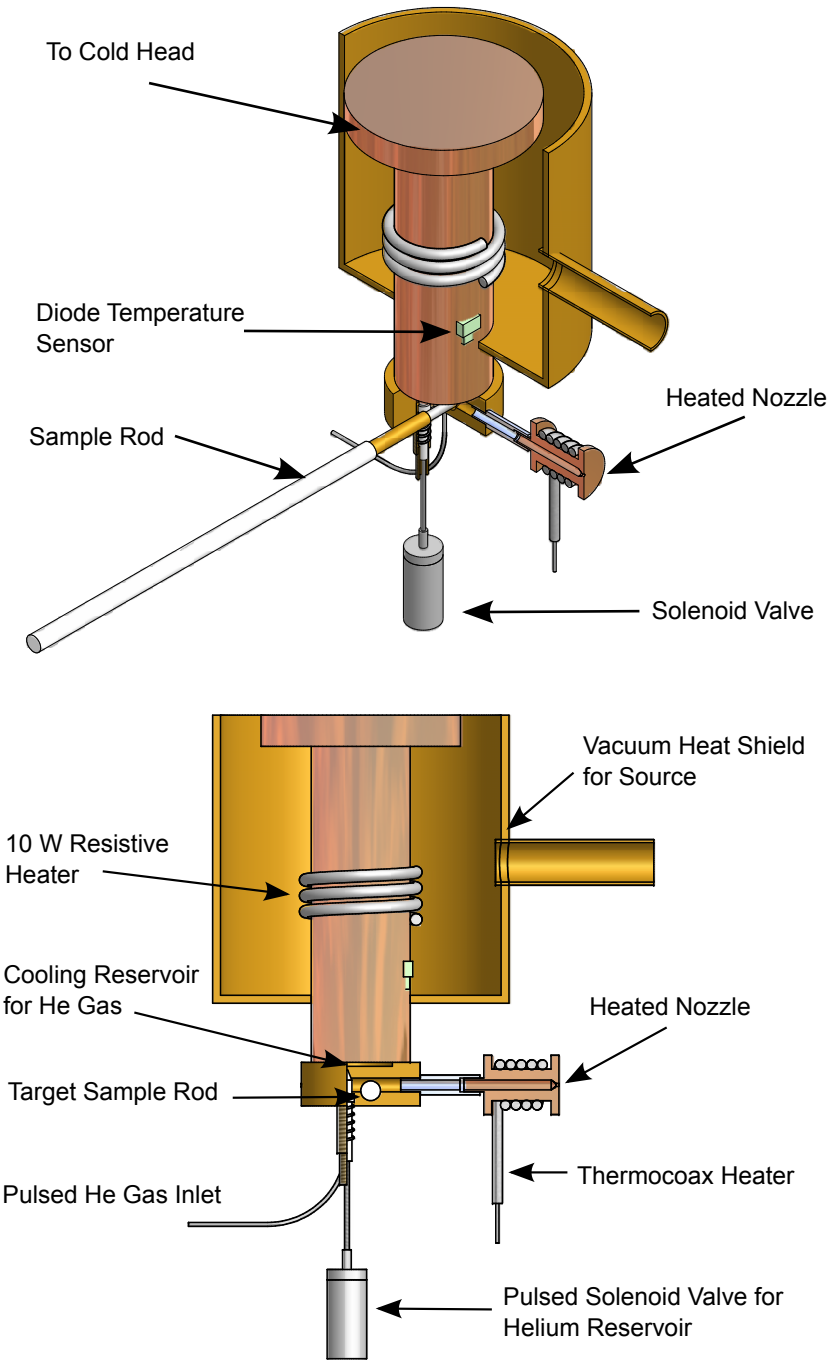

Figure 2.3: Three dimensional view of the laser vaporization cluster source

2.1.1.3 *Cryogenic System*

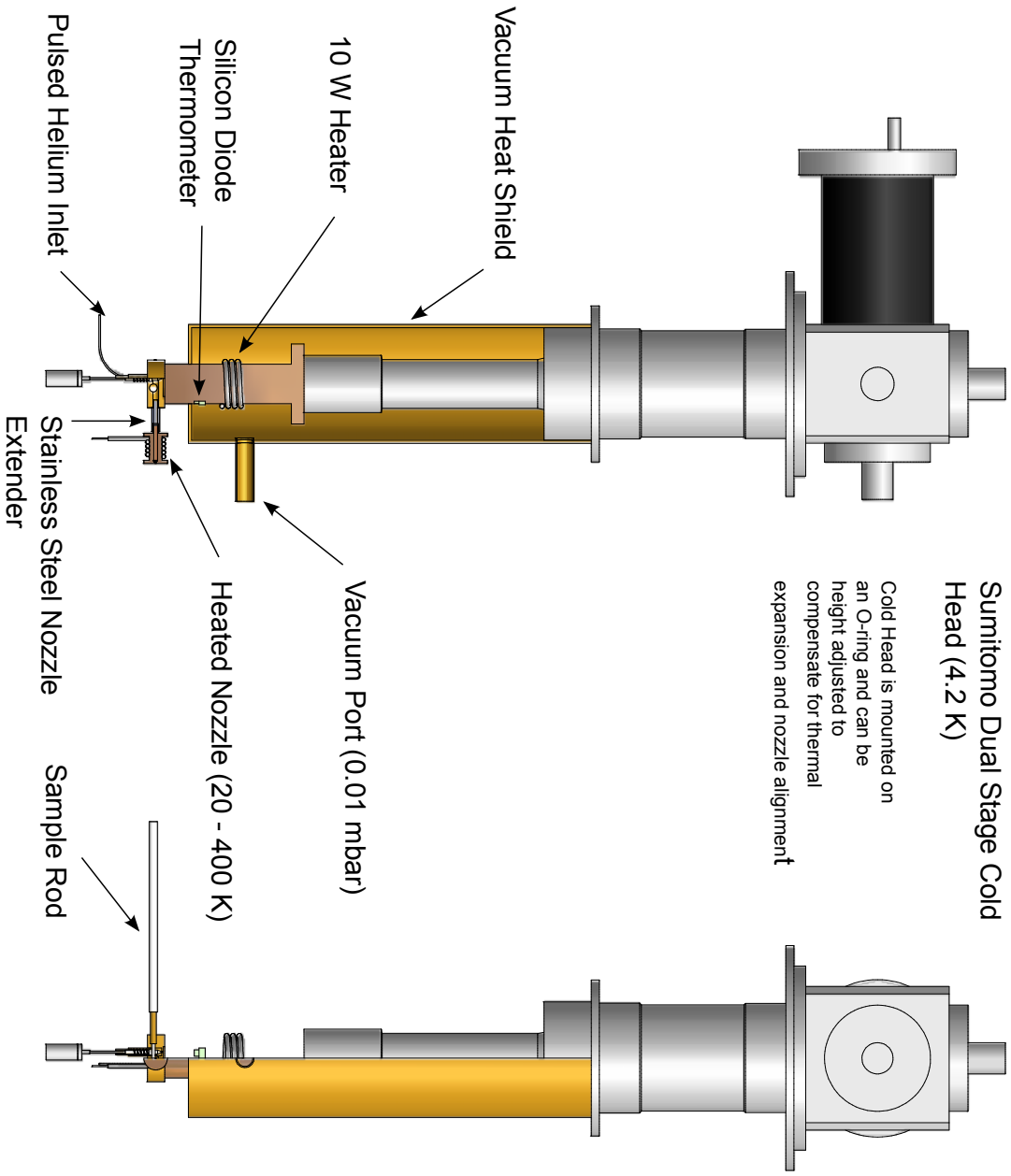

Figure 2.4: View of the cluster source attached to the cryocooler

To cool the cluster source to temperatures as low as 10 K, a closed cycle cryocooler

is used. The principle of refrigeration is similar to the well-known Sterling cycle, and the design is derived from the work of Gifford and McMahon[56]. High pressure helium gas is supplied to a cold head by a compressor, the gas does work against and displacer and absorbs heat from the cluster source.

The cryocooler is able to provide 30 W of cooling power at 40 K, and around 1 W of cooling power at 4.2 K. The lowest temperature is limited by the different heat loads onto the source. The main contributions include conduction by the gas, and radiation with the surfaces of the vacuum chamber which is at room temperature. Both of these heat loads can be reduced by enclosing most of the source at a vacuum pressure of 10^{-6} Torr. The radiative heat load is reduced by making use of polished brass and copper surfaces which have low emissivity in the infrared.

The remaining heat load comes from the buffer gas for the beam itself, which is delivered to the reservoir at room temperature in a train of 0.5-1 ms pulses at 20 Hz.

2.1.1.4 Pulsed Valves and He Reservoir

While the cluster source must be cooled to a temperature of 20 K to produce clusters at this temperature, this is not sufficient, because the buffer gas in which the clusters grow and must also be cooled to this temperature. If the He buffer gas was admitted directly to the source chamber it would be in thermal contact with the 20 K source walls for around 1-2 ms before flowing out through the nozzle. This is not enough time for this volume of He gas to cool from room temperature to 20 K. In order to ensure that the buffer gas is at the source temperature the He gas is first admitted to a small reservoir in the source where it dwells for 40-50 ms, after which it is injected into the cluster growth chamber by a second pulse valve.

The cooling reservoir and the dual pulse valve arrangement is illustrated in Figure 2.5.

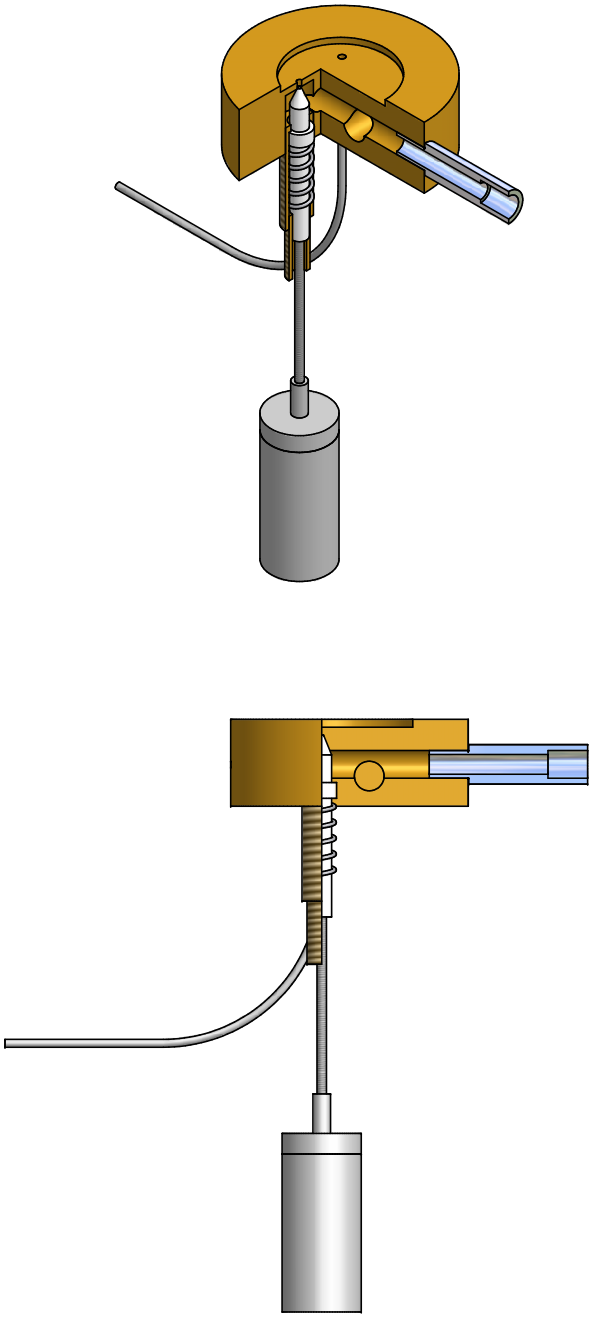

Figure 2.5: Close-up view of interior of the cluster source showing the He cooling reservoir, and the tandem pulse valve arrangement which supplies the He pulse to the cluster growth chamber.

2.1.1.5 Temperature Controlled Nozzle

While the system described in the previous section is very convenient for the production of clusters in the temperature range 10 - 60 K. Producing clusters at larger temperatures is difficult because the cooling power of the cryocooler dominates the 10 W heater which regulates the temperature of the source.

To produce clusters at higher temperatures we attach a second heated chamber to the cluster source at the end of the nozzle. This chamber is thermally insulated from the source by a thin walled stainless steel tube, which has low thermal conductivity at cryogenic temperatures. This chamber has a heater made from thermocoax which allows it to be warmed to temperatures as high as room temperature while adding only a modest heat load to the source. This setup has the advantage that much of the cluster growth takes place at a temperature of 20 K, where impurities in the carrier gas or laser ablation plasma are frozen out.

2.1.2 Velocity Measurement

The velocity is measured by placing chopper in front of the beam. The period of the chopper and all other distances and delays are known, so by synchronizing the chopper and the gas pulse so that the beam travels through a slit in the middle of the chopper, both the velocity of the beam and the dwell time of the clusters in the source can be calculated. The measurement of the dwell time allows us to verify that the clusters are in thermal equilibrium with the cluster source. The nozzle expansion is not supersonic so there is little cooling of the rotational degrees of freedom.

2.1.3 Electric Deflection Plates

The electric deflection plates have a coaxial geometry ($R_{\text{inner}} = 2.4\text{mm}$, $R_{\text{outer}} = 5.1\text{mm}$) the length of the deflection field is 22.5 cm, and the distance between the end of the electric deflection plates and the ionization volume of the mass spectrometer is 1.25 m. The voltage

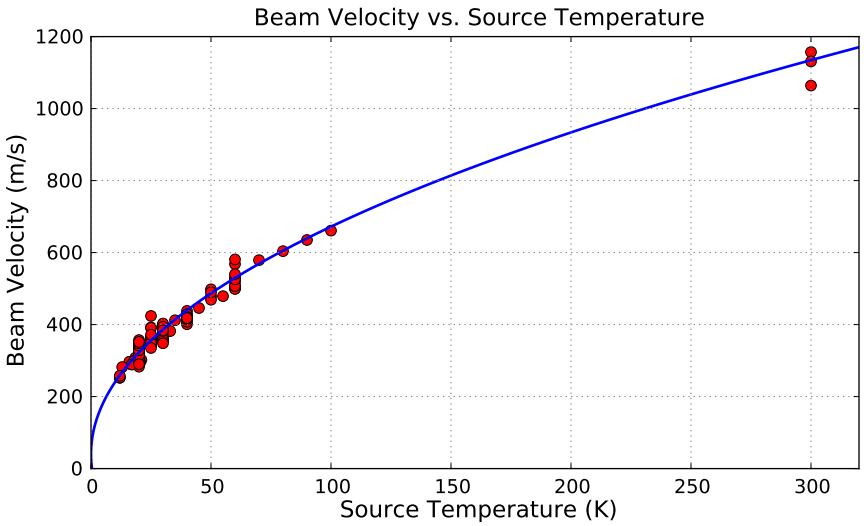

Figure 2.6: Plot of the empirical relation between the beam velocity and the source temperature derived from over 200 experimental runs. The temperature derived from the velocity of the beam is not necessarily equal to the temperature of the clusters, because the different cluster degrees of freedom are cooled at different rates by the growth and expansion process.

across the two electrodes can be set as high as 25 kV. This corresponds to an average electric field and field gradient of $9.25 \times 10^6 V/m$. The trajectory of the beam through the electric deflection plates is not known precisely this dependence can be captured by a calibration constant, which can be determined from a deflection experiment on a species with a known polarizability such as the Al, or Li atom.

2.1.4 Stern Gerlach Magnet

The design for the deflection magnetic is shown in Figure **??**. The pole faces of the electromagnet are shaped to match the equipotentials of the magnetic field due to two parallel line currents separated by a distance $2a$. This "two-wire" magnet design originates in the laboratory of I.I. Rabi [126]. The equipotentials are circles which pass through the two wires and are centered on the line bisecting them. This geometry of the two-wire field is shown in Figure 2.8.

To derive expressions for the potential, field, and gradient we make use of the fact that

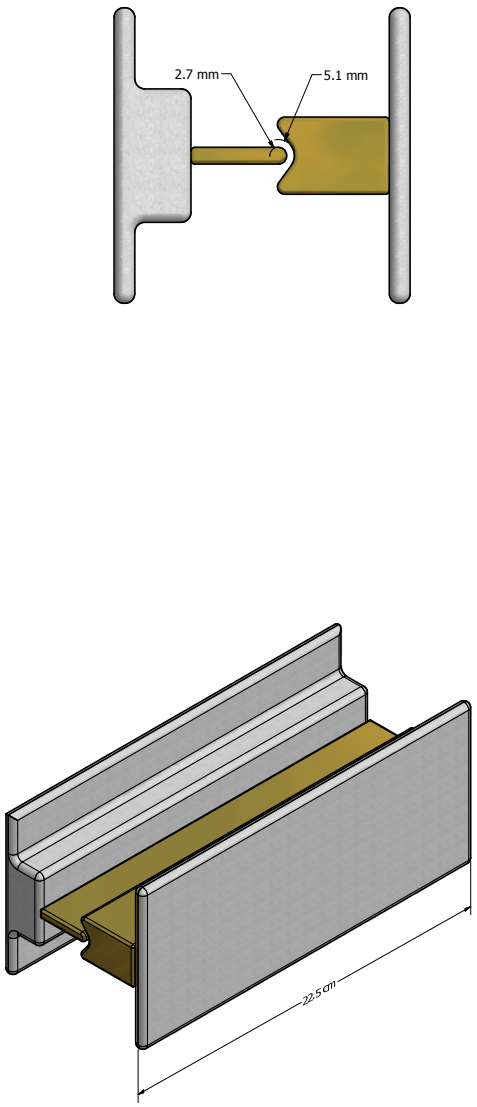

Figure 2.7: Geometry of the electric deflection plates

the field is chosen to be equivalent to that of two line currents. In free space this field can be written as the gradient of a scalar potential $B = -\nabla\psi$.

In the Cartesian coordinate system shown in Figure 2.8 the potential is:

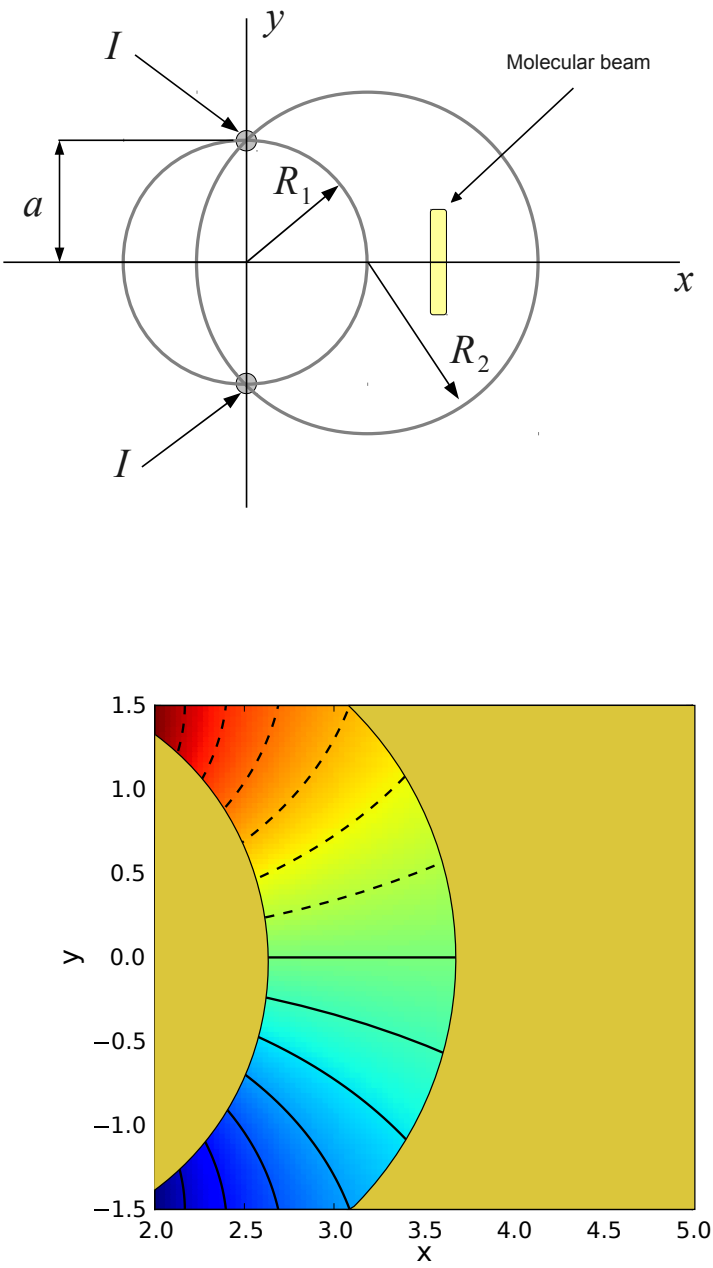

Figure 2.8: Geometry and field lines of the Rabi two-wire field

$$\psi(x,y) = C \log \frac{(y+a)^2 + x^2}{(y-a)^2 + x^2} \tag{2.1}$$

The x and y components of the magnetic field are:

$$B_x(x,y) = \frac{\partial \psi}{\partial x} \tag{2.2}$$

$$B_x(x,y) = -\left[\frac{x}{(y+a)^2+x^2} - \frac{x}{(y-a)^2+x^2}\right] \tag{2.3}$$

$$B_y(x,y) = \frac{\partial \psi}{\partial y} \tag{2.4}$$

$$B_y(x,y) = -\left[\frac{y+a}{(y+a)^2+x^2} - \frac{y-a}{(y-a)^2+x^2}\right] \tag{2.5}$$

$$\tag{2.6}$$

The exact value of the field and field gradient experienced by the cluster beam depends on the alignment of beam with the magnet. Because this can be measured with low precision, we calibrate the field and field gradient by performing a deflection experiment on the ${}^2P_{1/2}$ ground state of the aluminum atom. This state has a magnetic moment of $\mu_B/3$. The deflection profile for the atom is shown in Figure 2.11.

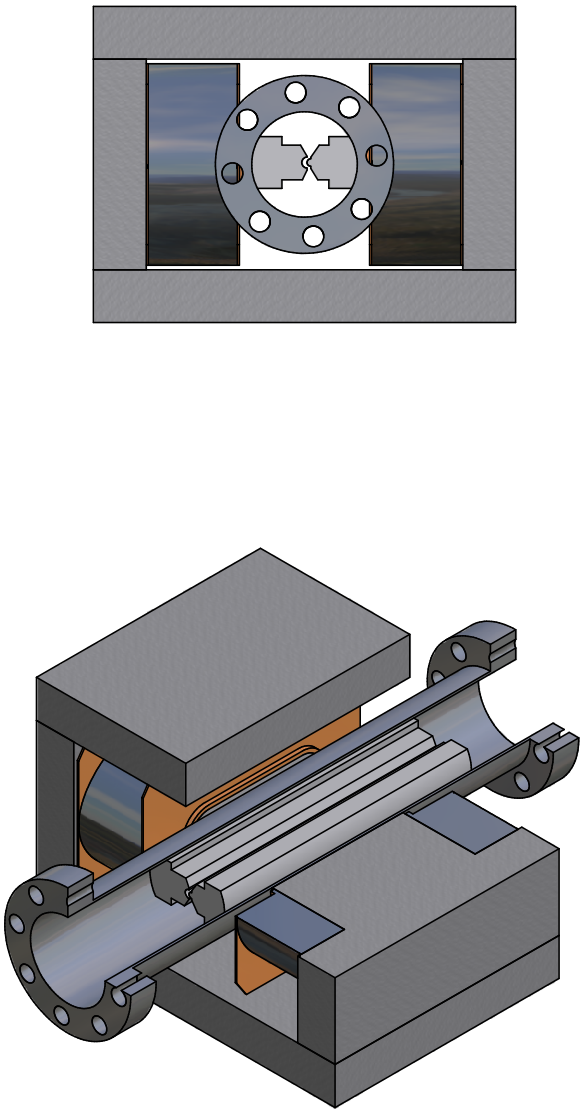

Figure 2.9: Coils and yoke of the stern Gerlach magnet

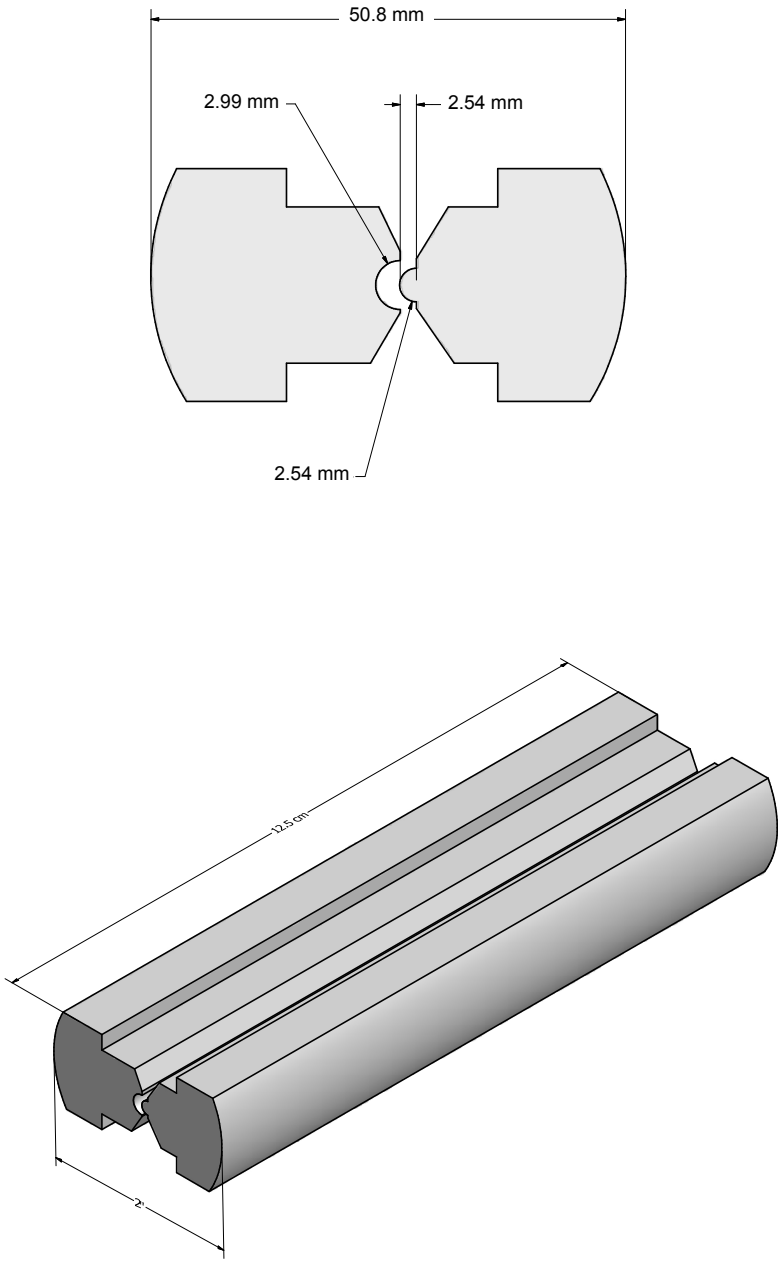

Figure 2.10: Geometry Stern-Gerlach magnet pole faces

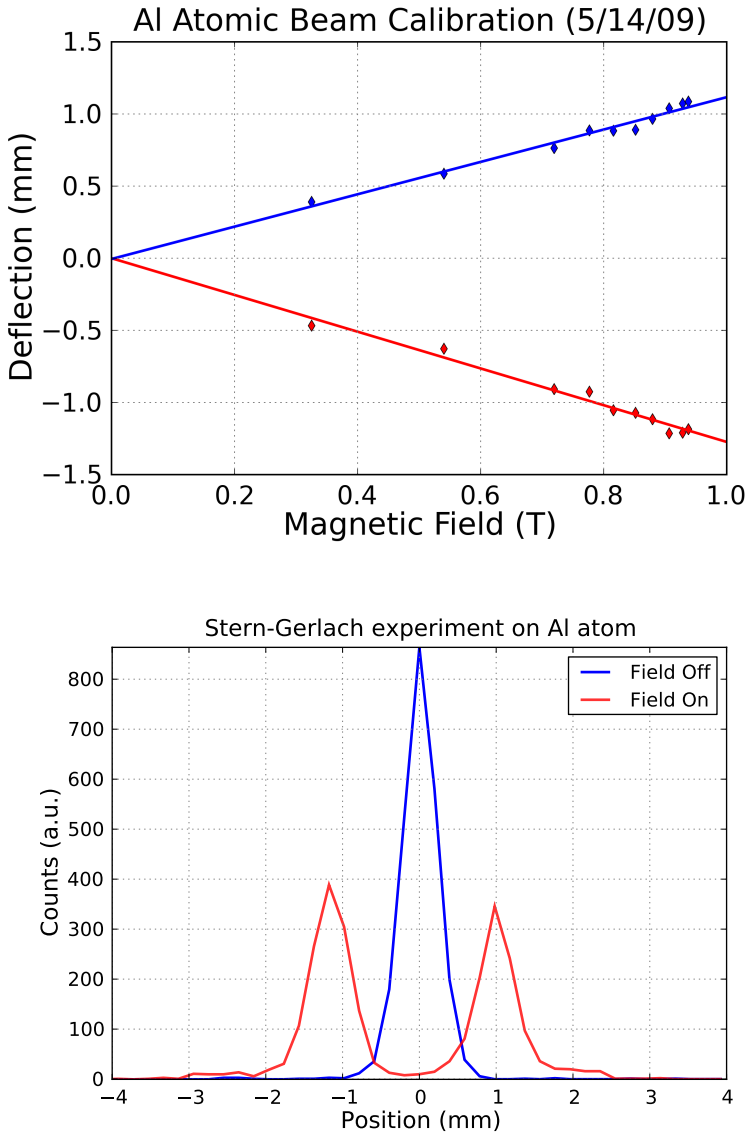

Figure 2.11: Calibration of the SG deflection magnet by deflection of the Al atom. At 20 K, the population is mostly the $J = 1/2$ ground state.

2.1.5 Time of Flight Mass Spectroscopy

When the clusters leave the source, the beam contains a broad distribution of cluster sizes. Time of flight mass spectroscopy allows the different masses in the beam to be separated. By choosing the voltages of the mass spectrometer so that the time of flight is sensitive to the position in the ionization volume, the deflections can be measured for all masses in the beam simultaneously.

The deflection of the beam is measured by a position sensitive time of flight mass spectrometer (PS-TOFMS). The clusters are ionized by an ArF excimer laser (193 nm / 6.45 eV, 10 ns pulses, 10 mJ per pulse) This photon energy is sufficient for the ionization of most metal clusters. The ions are extracted from the beam by an orthogonal repeller plate / extractor grid (R/E). The R/E voltages can be adjusted so that the TOF is sensitive to the position of the ions in the ionization volume. The shift in the time of flight is linear in the position over a volume of 1.5 cm^3. (see Figure 2.13) The position-sensitivity is calibrated by a movable slit which is placed in front of the entrance to the mass spectrometer.

2.1.5.1 Details of TOFMS

A more in-depth picture of the TOFMS is shown in Figure 2.14. Most modern time of flight mass spectrometers trace their design to an article by Wiley and McLaren [158] who introduced a method of using multiple acceleration grids to compensate for the initial velocity or width of the beam of charged particles.

The ions are detected by a microchannel plate at the end of a field free drift tube. The signal is amplified by a counter discriminator. The threshold of the pulse discriminator is carefully set so that a small noise count rate is detectable with no ions, this ensures that we do not reject any clusters which are deflected far in the tails of the beam. The intensity of the beam is adjusted so that there is no distortion of the deflection profile due to double counting.

An example mass spectrum is shown in the Figure 2.15 which shows the small shift in

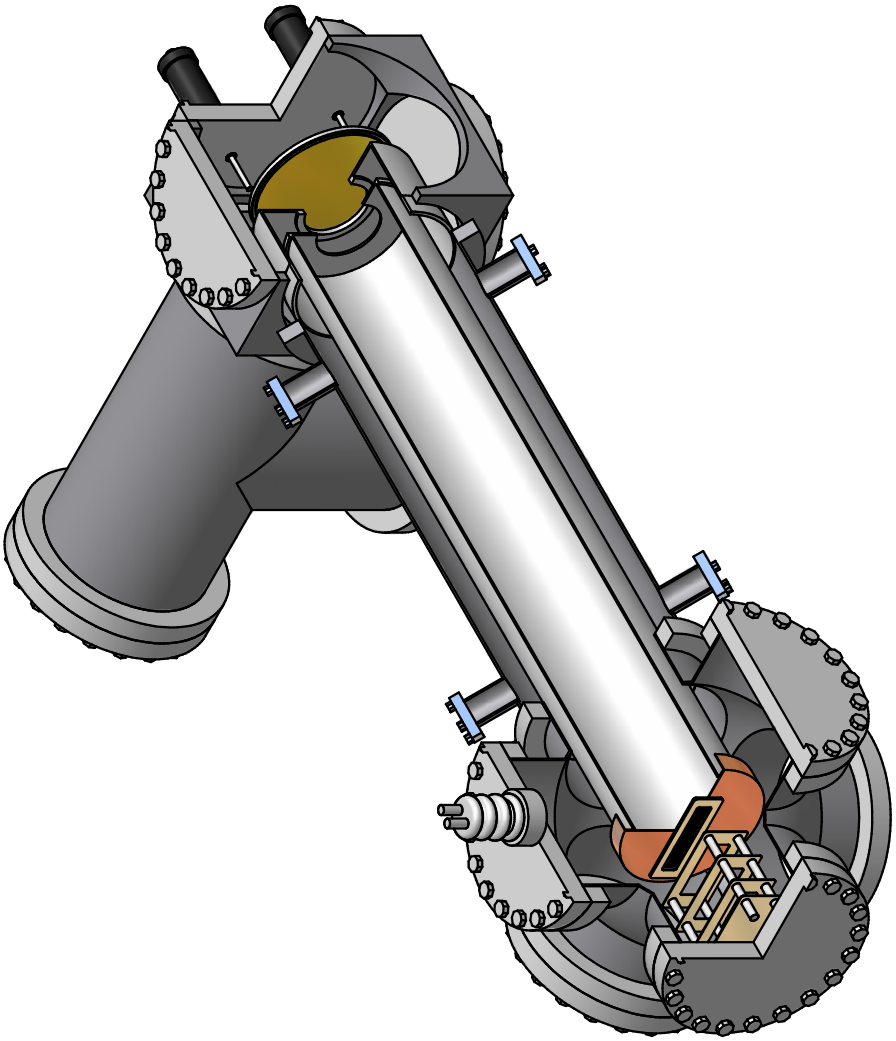

Figure 2.12: Time of flight mass spectrometer shown in it's vacuum chamber

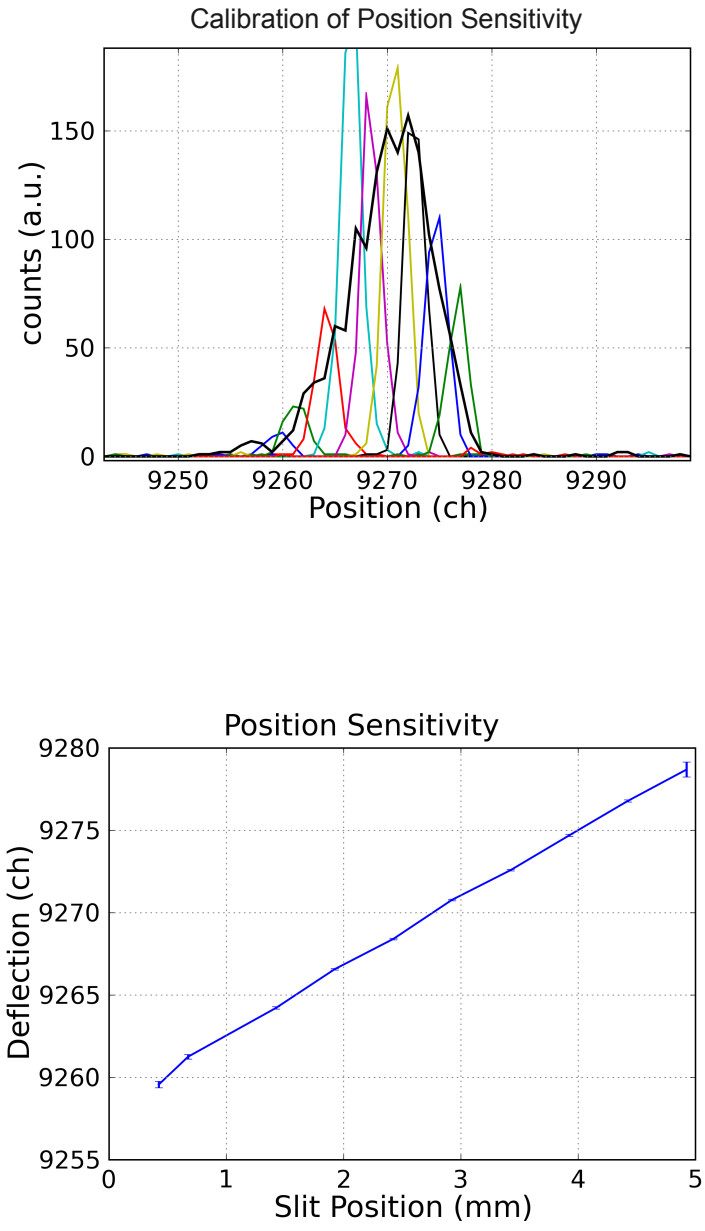

Figure 2.13: Calibration of the position sensitivity of the mass spectrometer with the use of a narrow slit at the entrance to the TOFMS

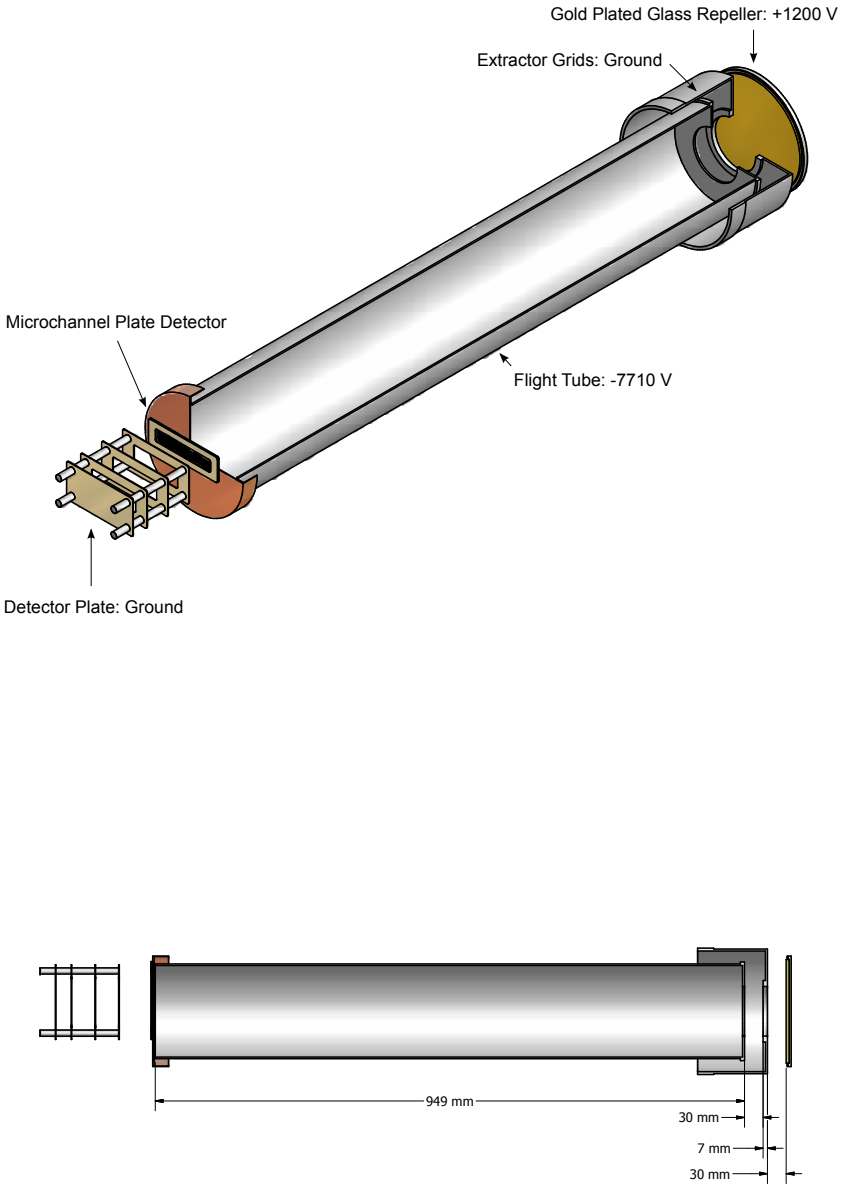

Figure 2.14: Geometry of the time of flight mass spectrometer

time of flight caused by a deflection field (red curve).

2.2 Analysis of Deflection Profiles

Electric and Magnetic deflection experiments both have the same general form. The cluster of mass m with velocity v, travels through a field which applies an inhomogenous electric or magnetic field to the cluster in the direction transverse to the beam. $E, \nabla E$ or $B, \nabla B$. The field induces a polarization or magnetization P or M in the cluster and the cluster then experiences a transverse force

$$F_{\text{electric}} = P \cdot \nabla E \tag{2.7}$$

$$F_{\text{magnetic}} = M \cdot \nabla B \tag{2.8}$$

The deflection of the cluster by the time it reaches the detector is given by the formula

$$\delta = K\frac{P\nabla E}{mv^2} \tag{2.9}$$

$$\delta = K\frac{M\nabla B}{mv^2} \tag{2.10}$$

where K is a calibration constant that depends on the geometry of the deflection plates, and the distance between the deflection plates and the detector.

For electric deflection experiments the polarization has two contributions: the electronic polarizability α, and the time averaged projection of any permanent dipole moment onto the direction of the field $P_{dip} = \langle \mu_E \cdot E \rangle_t$. For a rotating cluster this projection depends on population of the rotational states of the cluster, and therefore on the rotational temperature T_R.

$$P = \left(\alpha + \kappa\frac{\mu_E}{kT}\right) \tag{2.11}$$

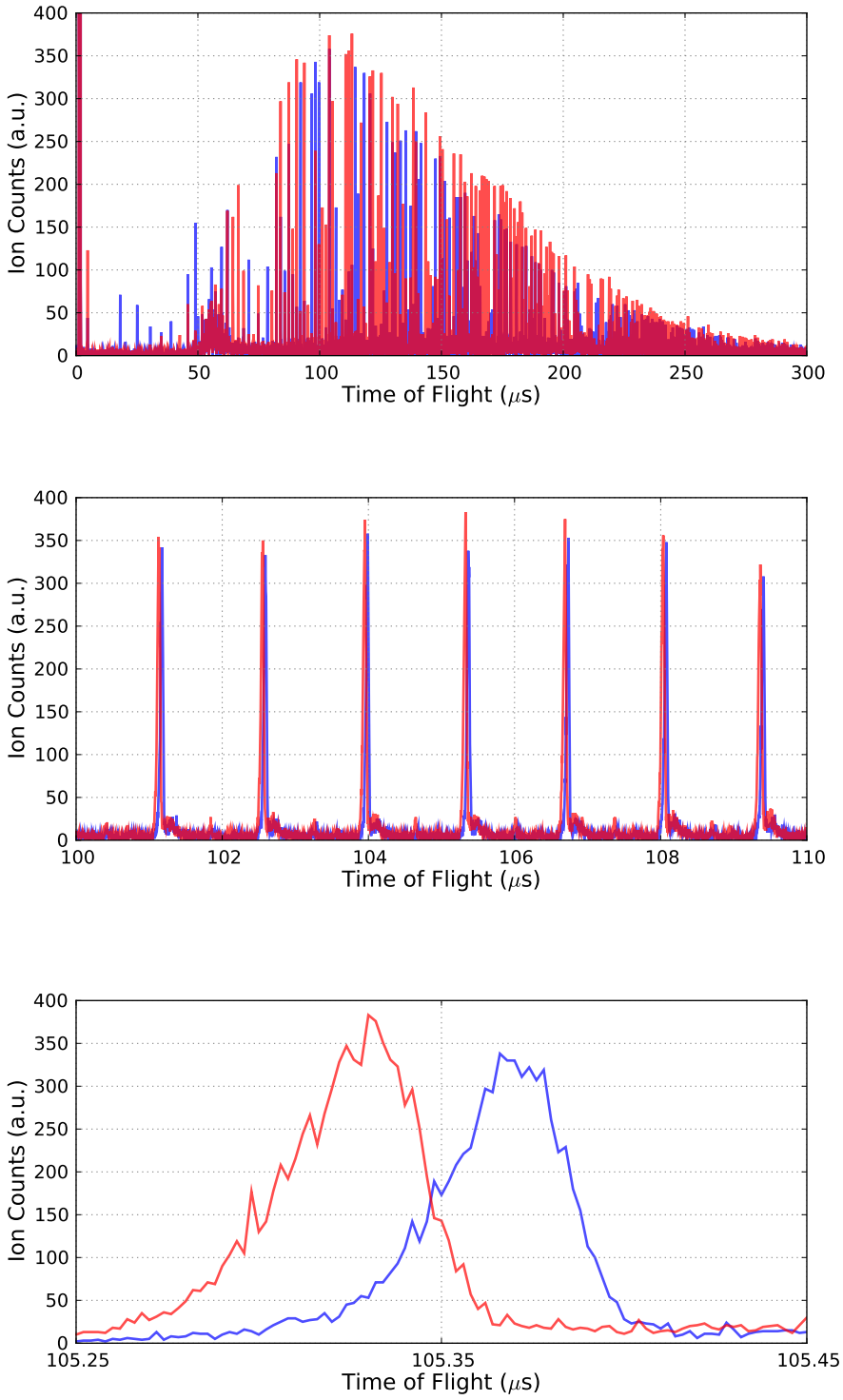

Figure 2.15: Time of flight spectra - the red curve is with the electric field on and the blue curve is with the electric field off, the small shift in time of flight allows the deflections of all clusters in the beam to be measured simultaneously

2.2.1 Static Response of a Cluster to an Electric Field

Figure 2.16 shows a calculation for the polarizability of a metal sphere. This leads to the intuitive conclusion that the polarizability of a metal sphere is a measure of its volume $\alpha = 4\pi\epsilon_0 R^3$.

For atoms, the polarizability is due to the quadratic stark effect. To prove this we make use of the definition of polarization as the slope of the stark diagram: $P = -\frac{dU}{dE}$. The induced polarization is determined by how much the energy of an atom or cluster changes in an applied electric field.

For an atom, we can compute these slopes using perturbation theory. Let $|0>$ be the ground state and $|n>$ be the excited states of an atom. The energy of the bound electron in an electric field is given by $H' = e\hat{r}E$ where $\hat{r}$ is the position operator. To first order the shift in energy is:

$$\Delta U^{(1)} =< 0|e\hat{r}E|0 > \tag{2.12}$$

Which is zero because of the familiar dipole selection rule.

Thus, to compute the polarizability we must evaluate the energy shift to second order in perturbation theory.

$$\Delta U^{(2)} = (eE)^2 \sum_n \frac{| < n|\hat{r}|0 > |^2}{E_n - E_0} \tag{2.13}$$

Equating this with the form $U = \frac{1}{2}\alpha E^2$ yields a formula for the polarizability.

$$\alpha = -2e^2 \sum_n \frac{| < n|\hat{r}|0 > |^2}{E_n - E_0} \tag{2.14}$$

Several observations are in order. First note that the polarizability of a quantum state is inversely proportional to the energy gap separating it from excited states. So atoms in highly excited Rydberg states have a large polarizabilities. A metal has an infinitesimal

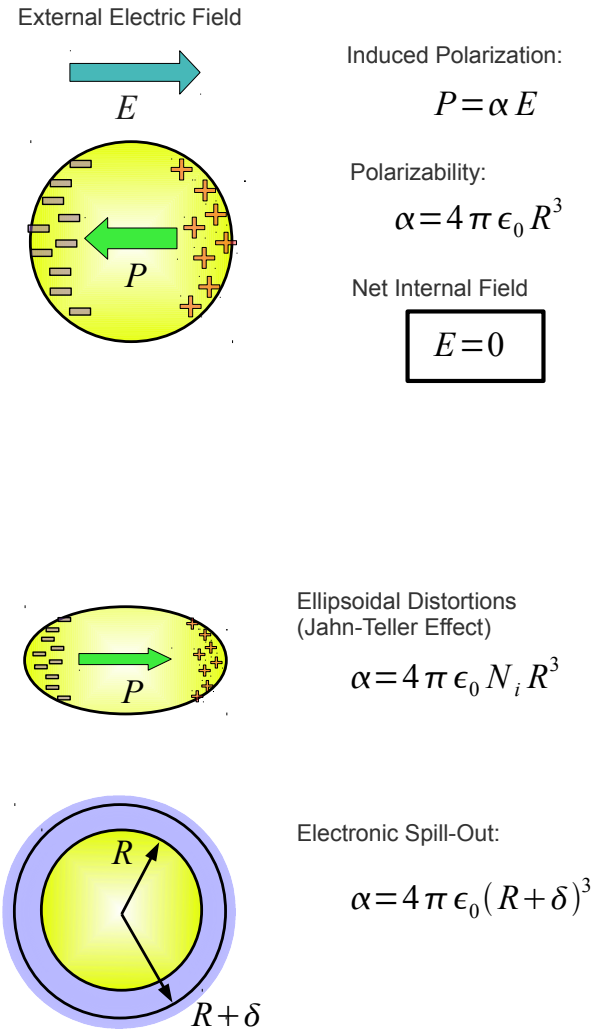

Figure 2.16: Illustration of the static dipole polarizability of a metal sphere. When an external electric field is applied surface charge accumulates on the metal to enforce the condition that $E = 0$ inside the bulk of the metal. The formula can be derived by enforcing this boundary condition. Important physical features to note are that (a) the polarizability α is proportional to the volume of the sphere, thus it can be used as a measure of the volume. (b) In the case of an ellipsoidal particle the polarizability along different axes differs by a depolarization factor N_i. For real metals it is necessary to account for the electronic spillout which is typically on the order of 0.5 Å.

energy gap to its excited states, so it can be considered a limiting case where the energy denominator goes to zero.

Also note that a linear stark shift $U = \mu_E E$ is the quantum definition of a "permanent dipole". This requires that $< 0|e\hat{r}E|0 >= \mu_E$. The dipole selection rule states that $\hat{r}$ has a non-zero expectation only between states of opposite parity. From this we can conclude that a quantum state $|\phi >$ can have a permanent dipole if

1. $|\psi >$ is a degenerate subspace

2. Two states in the subspace $|\psi >$ have opposite parity

2.2.2 Dynamics of a Polar Rigid Rotor in an Electric Field

In this section we discuss the electric deflection experiment used to measure the dipoles. The emphasis here is on the measure of the deflection and the systematic errors of the apparatus which require correction. The details of the models used to extract the polarizabilities and dipole moments from the deflection distributions will be discussed in the next chapter.

Molecular beam electric deflection measurements of dipole moments have been applied before [23, 40] to determine the structure of biomolecules, and clusters [111, 134, 133, 135, 11, 88, 4].

The principle of the experiment is simple. Consider the trajectory of a single cluster with a mass m and a velocity v traveling through a deflection plate which applies an electric field and gradient $E, \nabla E$ transverse to cluster beam. For any position in the deflection plates both E and ∇E are proportional to the voltage V applied across the deflection plates. The field polarizes and exerts a force on the cluster beam. The deflection of the cluster at the detector is:

$$\delta = K\frac{PV}{mv^2} \tag{2.15}$$

In the equation above, K is a calibration constant which depends only on the shape of the deflector, the length of the deflector, and the distance from the deflector to the mass

spectrometer. It is determined by a deflection experiment of a species with a known polarizability (e.g. the Li atom, or the Al atom).

The polarization P is defined to be the induced dipole moment projected onto the direction of the deflection field z. As previous mentioned, there are two main contributions to P: the electronic polarizability $P_\alpha = \alpha E$ and field projection of the permanent dipole moment time-averaged over its rotational motion $\langle \mu_z \rangle_t$. The value of $\langle \mu_z \rangle_t$ depends on the initial conditions (i.e. values of the conserved constants of motion) of the cluster when it adiabatically enters the electric deflector. The distribution of these conserved quantities are determined by the thermal conditions of the cluster source. The spacing between the rotational levels of our clusters is much smaller than kT_R, so we treat them as a continuum and use classical rigid body mechanics to analyze the deflection profiles.

For the ensemble of clusters in the beam we observe a distribution of deflections $\rho(\delta)$ and a entire distribution of polarizations $\rho(P)$. To analyze these distributions we make use of several simple models which relate the moments of the polarization distribution to the electronic polarizability and the dipole moment. (assuming that $\rho(P)$ has been normalized)

$$\bar{P} = \int P\rho(P)dP \tag{2.16}$$

$$\Delta P = \sqrt{\int (P-\bar{P})^2\rho(P)dP} \tag{2.17}$$

The simplest case to treat is a spherical rotor with polarizability α and dipole moment μ_E, in the limit where the dipole energy is much weaker than the rotational energy $\mu_E E/kT_R \ll 1$. In this case the polarization distribution has the analytic form [10] (*see chapter 3*):

$$\rho(P) = \frac{1}{\mu}\log\left(\left|\frac{P-\alpha E}{\mu}\right|\right) \tag{2.18}$$

Which allows the dipole moment and polarizability to be extracted by matching moments:

$$\bar{P} = \alpha E \tag{2.19}$$

$$\Delta P = \frac{|\mu|}{3} \tag{2.20}$$

For spherical and symmetric tops, there are known semi-analytic solutions [60, 10, 49] for the rotation and nutation of a polar rigid-body in an electric field. The formula in 2.20 applies to a spherical rotor – for a prolate or oblate symmetric top the value will be slightly different. (*see chapter 3*) For example, to get an error of 30% requires a symmetric top with a ratio of axes on the order of 1 to 10! For a more modest deviation from sphericity of $I_1/I_3 = 2$ gives an error in the dipole moment of 10%.

Thus, a precise quantitative estimate of the dipole moment requires knowledge of the inertia tensor and thus of the cluster structure.

For asymmetric tops, there is no analytic solution and the motion is unstable to chaotic tumbling [51, 5]. However, if the motion is unlikely to be perturbed, then the deflection distribution can still be computed by numerical integration of the rigid body equations of motion [48]. There is some evidence that asymmetric tops still show significant beam broadening, (see chapter 4)

2.3 Corrections to the Broadening

The previous section derived a relationship between the beam broadening and the dipole moment.

There are other causes of beam broadening that we must account for, a cluster with zero dipole moment, and only an electronic polarizability will still display some beam broadening due to the following effects.

1. The cluster beam has a finite width, thus different sections of the beam experience a different deflection field and will be deflected a different amount. This will cause the

clusters in the high field side of the beam to be deflected more than the clusters on the low field side, causing an increase in the width of the beam

2. If the clusters have a spread of velocities, then the slower clusters will be deflected more than the faster clusters, causing an increase in the beam width.

Both of the above effects are proportional to the average deflection of a cluster, and can be calculated using the formula

$$\delta = K\frac{\alpha E \nabla E}{mv^2} \tag{2.21}$$

2.3.1 Broadening due to Field Inhomogeneity

The electric field used in the electric deflection experiments has a coaxial geometry, thus the voltage, field and field gradient are given by

$$V(r) = \frac{V_0}{\log(R_1/R_2)}\log(r/R_2) \tag{2.22}$$

$$E(r) = \frac{V_0}{\log(R_1/R_2)}\frac{1}{r} \tag{2.23}$$

$$\nabla_r E(r) = \frac{V_0}{\log(R_1/R_2)}\frac{-1}{r^2} \tag{2.24}$$

The definitions of the symbols above are given in the section describing the coaxial deflection plates.

If the collimators for the cluster beam are positioned so that the center of the beam travels at radius r_c then the deflection of the cluster beam can be written as

$$\delta(r) = K\frac{\alpha V^2}{mv^2}\frac{1}{(r_c + r)^3} \tag{2.25}$$

For the values typical of our experiments $r_c \approx 3.5\text{mm} - -4.2\text{mm}$ and the width of the cluster beam in the deflection field is $w_c \approx 0.3\text{mm}$ so we can compute the broadening expected due to field inhomogeneity by expanding Eq. 2.25 about r_c as:

$$\delta(r) = \delta(0) + \left|\frac{\partial\delta(r)}{\partial r}\right|_0 r \tag{2.26}$$

$$= \delta(0) + K\frac{\alpha V^2}{mv^2}\left|\frac{-3}{(r_c+r)^4}\right|_0 r \tag{2.27}$$

$$= \delta(0) + \delta(0)\left(\frac{-3r}{r_c}\right) \tag{2.28}$$

Thus we see that the broadening due to the field inhomogeneity is proportional to the deflection, and the width of the beam. The larger that a cluster is deflected the wider the beam will be. Simulations of this effect are shown in the figure below

$$\Delta w_{\text{field}} = \delta(\frac{-3w_c}{r_c}) \tag{2.29}$$

2.3.2 Broadening due to Velocity Dispersion

The calculation of the broadening due to velocity dispersion is very similar to the above but for values of the velocity spread actually observed in our experiments this effect is negligible and contributes less than 1% to the broadening.

CHAPTER III

ANALYSIS OF DEFLECTION PROFILES

3.1 Overview

In this chapter we discuss the analysis of the deflection profiles, and the models that are used to relate the shapes of the profiles to the physical quantities of interest such as the electronic polarizability α, the electric dipole moment μ_E, and the magnetic moments μ_N of ferromagnetic clusters. The point of this analysis is to derive some simple formulas which relate the shape of the observed deflection profiles to the electric and magnetic dipole moments. As mentioned in the previous chapter, we characterize the shapes of the deflection profiles by computing the average and width.

There are close parallels between the electric and magnetic cases although the forces which bind an electric dipole and a magnetic dipole to a cluster body are very different. For the remainder of this chapter we use the term magnetization and polarization interchangeably. The meaning should be clear from context.

In both cases, we must consider the effects of the rotational motion of the cluster when it travels through the deflection field. The period of the rotational motion of a cluster is much shorter than the 10 - 100 μs travel time of a cluster through the deflection field, so the force experienced by each individual cluster is proportional to the projection of the electric or magnetic moment onto the deflection field, time averaged over several cycles of rotational motion.

$$F = \langle \mu \cdot \nabla B \rangle_t \tag{3.1}$$

The anisotropy forces which bind the electric or magnetic moment to the cluster's body also have a significant effect on the distribution of observed deflections. We explicitly

discuss the limit of strong anisotropy where the moment is fixed in the cluster body. The treatment here closely follows the prior work of [10, 49]. This "locked-moment" model is the case that is most relevant to electric dipole moments, because the most plausible physical mechanism is the charge inhomogeneity caused by localization of electrons in bonds. For transition metals we expect these bonds to be highly rigid like the bulk, so any unscreened charge inhomogeneities should be fixed in the clusters body fixed coordinate system.

In the low-field limit $\mu_E E/kT \ll 1$ the average polarization is linear in the field and has the form

$$\bar{P} = \frac{2}{9}\frac{\mu_E^2 E}{kT} \tag{3.2}$$

Note that this $2/9$ differs from the $1/3$ slope of the Langevin-Debye susceptibility. This adiabatic orientation process has been discussed in [57, **?**, 27, 139]

The theory for weak anisotropy, which applies to the magnetic moments of ferromagnetic clusters such as Fe and Co has been worked out by Xu et. al. [167, 168]. In this theory, the magnetization distribution can be computed from the slopes of the Zeeman curves. The avoided crossings in the Zeeman diagram cause all of the populated Zeeman levels to slope downward with increasing field, which explains the single sided deflections.

3.2 Magnetization Distribution

We are often interested in the field and temperature dependence of the moments, it is more convenient to work with the magnetization distribution instead of the deflection distribution, for the following reason: Consider again the deflection equation:

$$\delta = K\frac{M(B,T)\nabla B}{mv^2} \tag{3.3}$$

In the equation above $M(B,T)$ is the (generally) field and temperature dependent magnetization, which depends on the cluster's intrinsic moment and its interaction with the

deflection field. Because of the geometry of our deflection fields, the gradient is often simply proportional to the field $\nabla B \propto B$. The velocity of the beam is also roughly proportional to the square root of the temperature $v \propto \sqrt{T}$. (see Figure 2.6) Thus the deflection distribution should have the dependence overall dependence:

$$\delta \propto \frac{M(B,T)B}{mT} \tag{3.4}$$

These kinematic effects on the deflection are unrelated to the intrinsic magnetic properties of the cluster (captured in $M(B,T)$) so it is convenient to normalize away the dependence on field and velocity.

$$M = \frac{\delta m v^2}{K \nabla B} \tag{3.5}$$

So, instead of discussing a deflection distribution we will discuss a magnetization (or polarization) distribution.

To summarize our key points:

1. The average polarization of a cluster with polarizability α and dipole moment μ_E is

$$\langle P \rangle = \left(\alpha + \xi \frac{\mu_E^2}{k_B T_R} \right) E \tag{3.6}$$

   ξ is a constant which depends on the geometry of the cluster. $xi = 2/9$ for an adiabatic spherical rotor. $xi = 1/3$ (low field Langevin-Debye limit) for a fluctuating dipole, of one thermalized in the deflection field.

2. The dipole moment is related to the broadening of the beam. For spherical tops, in the low field / high temperature limit $x = \frac{\mu_E E}{k T_R} \ll 1$, the broadening is:

$$\Delta\delta = \frac{\mu_E}{3} \tag{3.7}$$

   For prolate or oblate symmetric tops, the beam is also broadened, but the exact numerical value depends on the deviation from sphericity which requires knowledge of

the cluster structure. In the next chapter we have reported dipole moments derived by relating the beam broadening to the spherical rotor model.

3. For asymmetric tops, we also expect to see some broadening (in fact, we have observed significant beam broadening on a polar cluster which known by independent means to be a highly asymmetric top see Sec. 4.6). It has been proposed that the rotational motion of a polar asymmetric top in a field is unstable to perturbations and will tumble chaotically [51, 5, 48]. For this case we see no evidence of chaotic tumbling.

4. If the magnetic or electric dipole moment of a cluster can move internally, and its motion is rapid on the time scale that the cluster spends in the deflection field, then a process analogous to thermal relaxation could hypothetically occur. These transformations are conceptually related to isomerization reactions of "floppy" molecules [154].

   There are some severe restrictions on this explanation in practice. First the internal motion is highly restricted because it must conserve energy and angular momentum, which is fixed for the whole isolated cluster. Second it requires some revision of the intuitive notion that metal clusters - (especially transition metal clusters) are rigid objects.

   Despite the vague justification of this mechanism, it has been invoked [11, 134, 133, 135] to explain electric deflection experiments where there is a large enhancement of the average polarization, far in excess of what can be explained by electronic polarizability. We have observed similar effects in Tm clusters (see Sec. 4.8.1)

5. For a large variety of plausible (but not optimized) cluster structures, we find that the majority are no more than 30% away from a spherical rotor, and of these most are close to the prolate or oblate limits. Thus the use of a spherical rotor is

6. Finally, we emphasize that a measurement of the beam broadening is a highly robust test for the presence of an electric dipole moment. The numerical values are only semiquantitative because the exact amount of broadening depends on the cluster structure. In cases where the broadening is reduced because of relaxation of the dipoles orientation in the field, the dipole will manifest itself as an enhancement of the average polarization.

3.3 Locked Moment Model

The "locked moment model" is a classical symmetric top with a permanent electric or magnetic dipole moment fixed along the symmetry axis. This model is very important in the analysis of electric and magnetic beam deflection experiments for polar and ferromagnetic clusters. We assume the magnetic case here and show calculations of deflection profiles for different values of $\mu B/kT$, and I_1/I_3. We give a detailed comparison between the predictions of this model and the Langevin-Debye model for the average deflection. We also discuss the broadening of the beam as a function of field, temperature, and deviation from sphericity.

3.3.1 Brief Description of Calculation

We give a brief summary of the calculation of the deflection profile. Calculating the time averaged projection of the axis of a precessing top is a part of physics folklore. I believe the first calculation was due to Lagrange.

We briefly describe this calculation to illustrate how the thermal population of an ensemble of rigid rotors gives a distribution of deflections.

There are three important elements:

1. The ensemble of rotors are initially at thermal equilibrium with the cluster source - the temperature of the source T, determines the population of rotational levels in the beam. (we neglect rotational cooling by nozzle expansion). The motion of each

rotor is determined by 3 conserved quantities (E, m_z, and m_3). We initialize our ensemble by choosing values for these quantities. Each value in the ensemble is given a statistical weight with the Boltzmann factor. $e^{-E/kT}$

2. The rotors adiabatically enter the electric field - When the field is turned on adiabatically, the conserved quantities will change and thus the motion of the rotor in the field changes. To compute the value of the conserved quantities in the field given their value in the source we use the "adiabatic invariants" of the symmetric top Hamiltonian[60]. It is important to account for this adiabatic entry - sampling from a ensemble thermalized in the deflection field will give incorrect results.

3. Once we have computed the constants of motion in the deflection field, we can compute the average projection onto the field axis $\langle M \rangle_t = \mu \cos\theta$. The periodic motion of θ is called nutation. There is a closed form formula for the time average of $\cos\theta$ over the nutation given in [60, 10, 49] We compute this time-average $\langle M \rangle_t$ for every element of our ensemble and group them into a histogram.

3.3.2 Deflection Profiles

The magnetization distribution is a function of two parameters: the ratio of the dipole energy to the thermal energy $x = \frac{\mu B}{kT}$, and the ratio of the principal moments of inertia I_1/I_3. In the $x \ll 1$ limit (called the low field limit) the deflection profile is symmetrically broadened about the field off peak. As $x \approx 1$ the profile becomes more asymmetric (the dipole orients itself with the field during the adiabatic entry process). Finally as $x \gg 1$ the deflection profile saturates at the value μ. This saturation behavior is similar to what happens in the Langevin-Debye model where the dipole thermally relaxes in the field, although this adiabatic rotor model is slower to saturate, and the low field limits of the two models have different values.

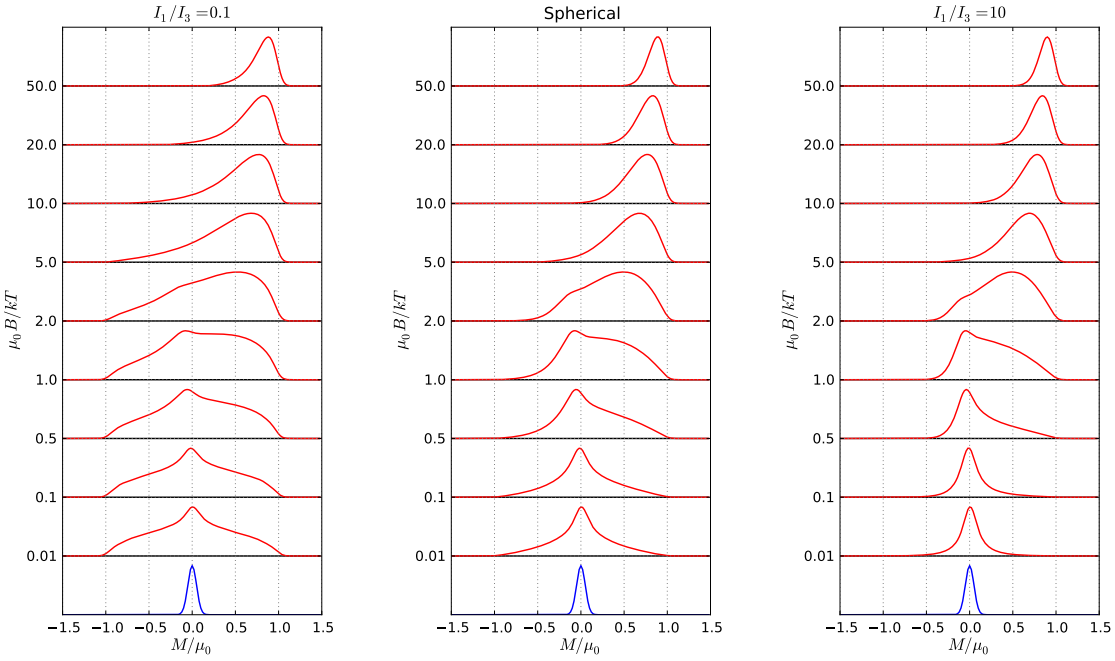

(a) Oblate **(b)** Spherical **(c)** Prolate

Figure 3.1: Magnetization distribution for different values of $x = \frac{\mu_0 B}{kT}$, and $\frac{I_1}{I_3}$. These have been normalized so that they have the same height rather than the same area, to emphasize the fine features of the shapes of the profiles.

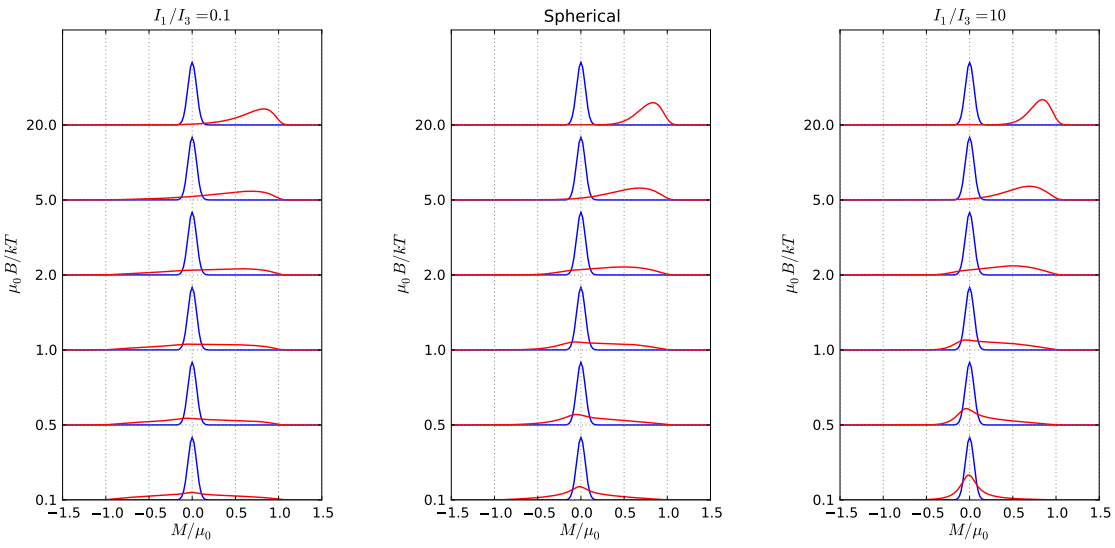

(a) Oblate **(b)** Spherical **(c)** Prolate

Figure 3.2: Magnetization distribution for different values of $x = \frac{\mu_0 B}{kT}$, and $\frac{I_1}{I_3}$. These are properly normalized by area, to compare the field on and field off profiles.

3.3.3 Average Deflection

Once we have calculated the deflection profiles we can give the average magnetization as a function of $\mu B/kT$. Note that the low field limit for the Langevin-Debye model is $\langle M \rangle / \mu = \frac{\mu B}{3kT}$. The low-field limit for the spherical adiabatic rotor is $\langle M \rangle / \mu = \frac{\mu B}{3kT}$

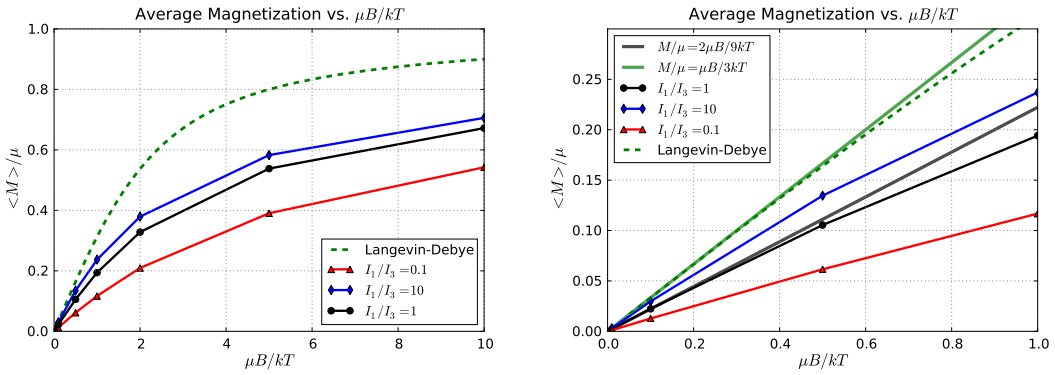

Figure 3.3: Average of the magnetization distribution $\langle M \rangle / \mu$ for prolate, oblate and spherical rotors as a function of $\mu B/kT$. Note that for the spherical rotor, $\langle M \rangle / \mu \approx \frac{2}{9}\frac{\mu B}{kT}$ in the $\mu B/kT \ll 1$ limit. The magnetization saturates much more slowly than the Langevin Debye model. Also, the low field limit is different.

3.3.4 Broadening

We can also compute the beam broadening as a function of x: In the $x \ll 1$ limit for a spherical rotor the distribution has the known analytic form

$$p(M/\mu) = \frac{1}{2} \log\left(\frac{\mu}{M}\right) \tag{3.8}$$

The standard deviation of this distribution is

$$\frac{\Delta M}{\mu} = \frac{1}{3} \tag{3.9}$$

Our calculations agree with this result, although it is important to note that in the low-field limit the the broadening does depend on I_1/I_3. So while getting a precise estimate of the dipole moment from this method requires knowledge of the structure, this is an extremely robust test for the presence of a dipole moment.

Even in the zero-field limit where $x \ll 1$ the amount of broadening depends on the ratio of axes of inertia.

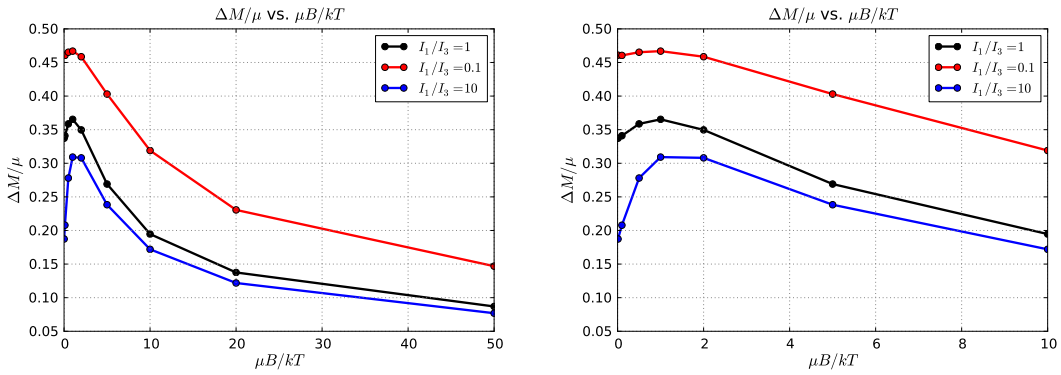

(a) Broadening over full range

(b) Broadening for $x \approx 1$

Figure 3.4: Width of the magnetization distribution $\Delta M = \sqrt{\langle (M - \langle M \rangle)^2 \rangle}$, for prolate, oblate and spherical rotors as a function of $\mu B/kT$. Note that for the spherical rotor, $\Delta M/\mu = 3$ in the $\mu B/kT \ll 1$ limit.

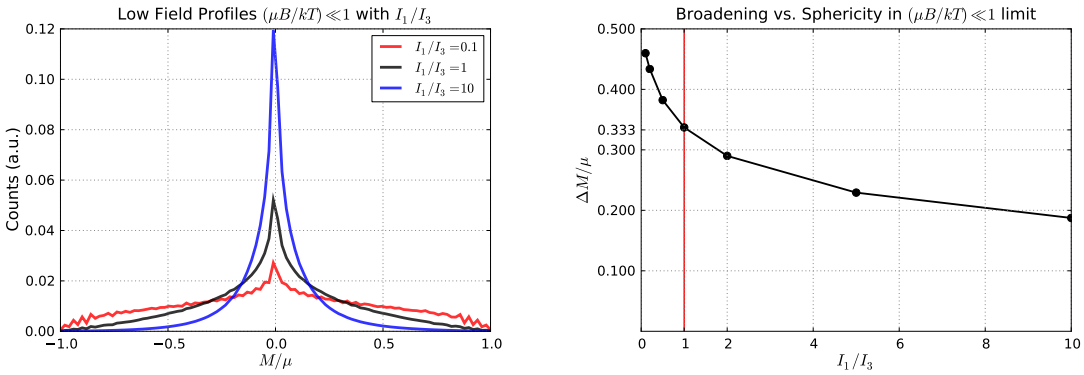

(a) Magnetization distribution for different values of I_1/I_3: an oblate spheroid, a spherical rotor, and a prolate spheroid. Note that these two limits correspond to extreme distortions away from sphericity - a ratio of 1 to 10. They are normalized by area.

(b) Second moment of the low-field $x \ll 1$ magnetization distribution as a function of I_1/I_3. Notice that when $I_1/I_3 = 1$, the $\Delta M/\mu = \frac{1}{3}$

Figure 3.5: Behavior of the beam broadening in the low-field limit.

3.3.5 Some Concrete Examples

It is also important to consider how close realistic experimental conditions are to the limits described above. We consider both electric and magnetic cases.

Electric dipole moments are measured in Debye (1 D = 3.33×10^{-30} C m). The largest electric fields used in our experiment are on the order of 22 kV / 5 mm = 7.3×10^6 V/m. The source temperatures used in our lab are typically 20 K. pE/kT is plotted for a variety of values of p below.

The magnetic case is entirely analogous - the largest magnetic fields possible with the resistive electromagnets used in our lab are 2 T. Consider a Ho clusters, and suppose that each Ho atom contributed its full atomic moment (10.6 μ_B) to the magnetic moment of a cluster. In this case a Ho_{20} cluster would have a magnetic moment of 212 μ_B. With a rotational temperature of 20 K, this gives a value of $\mu B/kT \approx 14$, which is deep into the saturation limit.

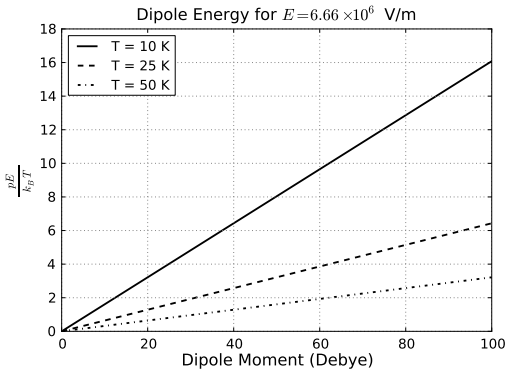

(a) $\frac{pE}{k_BT}$ at an electric field of E = 6×10^6 V/m. Note that it takes very large dipole moments to get anywhere close to the saturation limit. Metal clusters with few exceptions have zero dipole moments - so the low-field limit is almost always appropriate for the analysis of metal cluster deflection profiles.

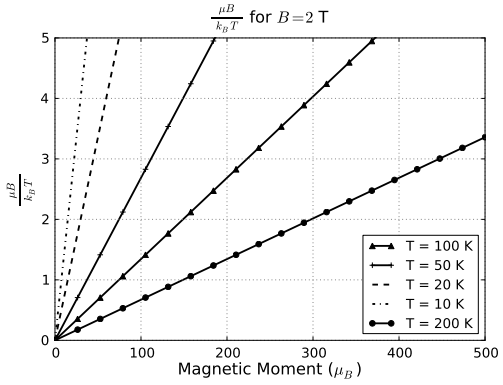

(b) $\frac{\mu B}{k_BT}$ at a magnetic field of B = 2 T.

Figure 3.6: Values of pE/k_BT and $\mu B/k_BT$ for realistic experimental conditions.

3.4 Asymmetric Rotors

The previous section has discussed the dynamics of a polar symmetric top in an electric or magnetic field. The assumption that a cluster is a symmetric top is quite restrictive. We expect that the majority of metal clusters are in fact asymmetric tops (albeit with a nearly spherical shape due to surface tension)

As discussed, the observed distribution of deflections is very sensitive to the rotational dynamics of a cluster, and thus to the population of rotational levels. How do the rotational dynamics of a polar asymmetric top differ from those of a polar symmetric top?

The first key difference between symmetric and asymmetric rotors is that the dipole moment is no longer restricted to lie along the symmetry axis. Thus to completely specify the problem we must give both the direction and magnitude of the electric or magnetic moment in the body-fixed coordinate system.

The Quantum Hamiltonian for this case is:

$$H = AJ_x^2 + BJ_y^2 + CJ_z^2 + \mu \cdot E \tag{3.10}$$

with $A \neq B \neq C$. We use the symbol μ to refer to either the electric or magnetic moment, and E to refer to the electric or magnetic field.

For almost all of the clusters considered in this thesis, the rotational constants are small enough that the rotational levels are effectively a continuum relative to the thermal energy kT at $T = 20K$. Therefore, we can treat the rotational motion using classical rigid body dynamics,

Unlike the symmetric top, the polar asymmetric top in an electric field has no known analytic solution. The only conserved quantity is the total angular momentum, and the projection of the angular momentum onto the space fixed axes (corresponding to the quantum numbers J and M). For symmetric tops, the projection of the total angular momentum onto the body-fixed axes is conserved, and each value K is doubly degenerate, the asymmetry breaks this degeneracy and mixes states with the same J but different K.

There is no known analytic solution to the asymmetric polar top in an electric field. We must note that the effect of chaotic tumbling is unlikely to depend on the value of κ alone. To illustrate this, consider two maximally asymmetric tops which both have $\kappa = 0$. The first one has $A = 1, B = 2, C = 3$, the other has $A = 99, B = 100, C = 101$. The second molecule is far closer to a sphere than the other, and so we would expect the effect of chaotic tumbling to be much less severe, despite both being highly asymmetric tops.

3.4.1 How asymmetric are clusters?

Chaotic dynamics and avoided crossings can have a dramatic effect on the deflection dynamics of a cluster in an electric or magnetic field. There are of course few experimental methods that allow for the determination of cluster structure, but global optimization methods can give us some highly plausible guesses for what structures are possible for N atoms interacting under different approximate pair potentials. Our purpose here is not to debate the merits of these different interaction potentials or how realistically these potentials account for the numerous and complex interactions which determine the ground state structure of real clusters.

A large collection of structures derived in this way have been calculated and are published at the Cambridge Cluster Database by Doye and others. Examples include the series of Lennard-Jones clusters which have been discussed extensively by Wales.

For three series of optimized structures, we have plotted three quantities

1. **Volume per Atom** In the structures the atoms are considered to be interacting point particles, so it is technically meaningless to speak of the volume of a discrete set of points. As a practical definition, we first compute the principal moments of inertia of the cluster (I_1, I_2, I_3). Then for the volume we use the volume of an ellipsoid which has the same moments of inertia

$$V_{\text{ellipsoid}} = \frac{4\pi}{3}abc \tag{3.11}$$

$$a = \sqrt{\frac{5}{2}\frac{I_2 + I_3 - I_1}{Nm_a}} \tag{3.12}$$

$$b = \sqrt{\frac{5}{2}\frac{I_1 + I_3 - I_2}{Nm_a}} \tag{3.13}$$

$$c = \sqrt{\frac{5}{2}\frac{I_1 + I_2 - I_3}{Nm_a}} \tag{3.14}$$

$$V_a = V_{\text{ellipsoid}}/N \tag{3.15}$$

In the equations above N is the number of atoms and m_a is the atomic mass.

We plot this volume as a function of the number of atoms. We notice that for all of the structures considered, V_a increases and converges to a fixed value. There are fluctuations about this slow trend which apparently reflect the ability of some sizes to assume especially compact geometries. Among these include the well-known MacKay Icosahedra - 13, 55, and 147.

2. **Deviation from Sphericity** Once we have computed the principal moments of inertia of each structure, we want a measure of how much spread there is between the principal moments. To quantify this, we express the difference between the largest I_{max} and smallest I_{min} of the principal moments as a percentage of I_{max}.

$$\text{(Deviation from Sphericity)} = \frac{I_{max} - I_{min}}{I_{max}} \tag{3.16}$$

This quantity is 0 for a spherical top, and 1 for a linear rotor.

For all of the structures we considered, very rarely is there more than a 30% variation among the principal moments.

3. **Ray's Asymmetry Parameter:** κ For an asymmetric top cluster with three unequal principal moments of inertia ($I_1 < I_2 < I_3$) We want a parameter that will smoothly

interpolate between the prolate $I_1 = I_2 < I_3$, or oblate $I_1 < I_2 = I_3$ symmetric top cases. If we define the rotational constants as

$$\begin{aligned} A &= \hbar/2I_1 \\ B &= \hbar/2I_2 \\ C &= \hbar/2I_3 \end{aligned}$$

Then Ray's Asymmetry parameter is

$$\kappa = \frac{2B - A - C}{A - C} \tag{3.17}$$

This quantity is -1 for a prolate top, 1 for an oblate top, and 0 for a maximally asymmetric top (one whose third principal moment is half way between the other two.

For this reason we have plotted the deviation from sphericity of the clusters: It expresses the difference between the largest and smallest principal axes of inertia as a percentage of the largest principal axis.

$$\Delta = \frac{I_{\text{max}} - I_{\text{min}}}{I_{\text{max}}} \tag{3.18}$$

The tables in Figures 3.7, 3.8 3.9, 3.10 show the deviation from sphericity is very rarely larger than 0.2!

What fraction of clusters are actually symmetric tops? One intuitive argument is that a solid or liquid clusters has a surface tension that is proportional to the surface area of the cluster. Minimization of this surface energy favors the formation of spherical clusters, because the sphere has the smallest surface area for a fixed volume. This intuition is correct for bulk liquids, but it is highly questionable for metal clusters which can show directional

bonding. The energy gained by forming directional bonds could more than make up for the cost of a large surface area. Covalently bonded structures can take on rigid geometries of almost limitless complexity, and the constraints of the sp^n bond angles can dominate the tendency for molecules to collapse under surface tension. There are also many examples of single element clusters (e.g Gold) which for small sizes favor the formation of planar, and tubular structures. While we lack experimental methods which can directly determine the structure of a cluster, there are many plausible theoretical guesses as to what the structures are and they have been compiled and published for a wide variety of interaction potentials. The methods used to calculate and optimize cluster structures vary a great deal in their realism. Finding the structure can be formulated as a global optimization problem of a high-dimensional potential energy surface where the number of local minima scales exponentially with the number of atoms.

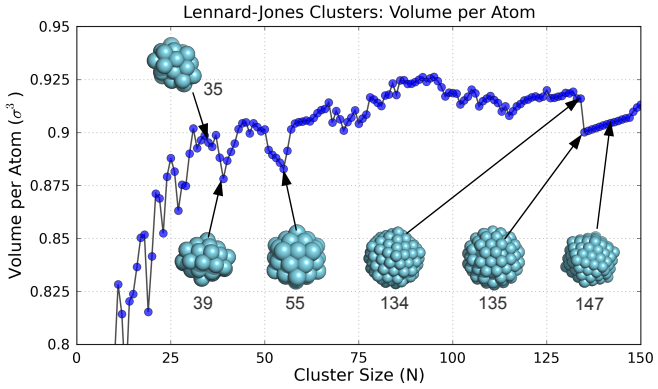

(a) volume per atom LJ_{3-150}

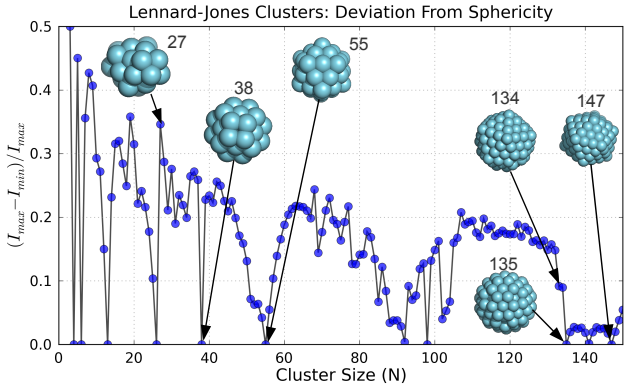

(b) deviation from sphericity for LJ_{3-150}

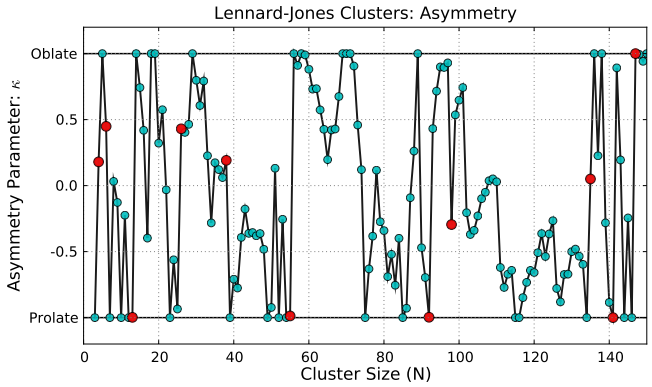

(c) Ray's asymmetry parameter for LJ_{3-150}

Figure 3.7: Descriptive statistics of Lennard-Jones clusters $N < 150$

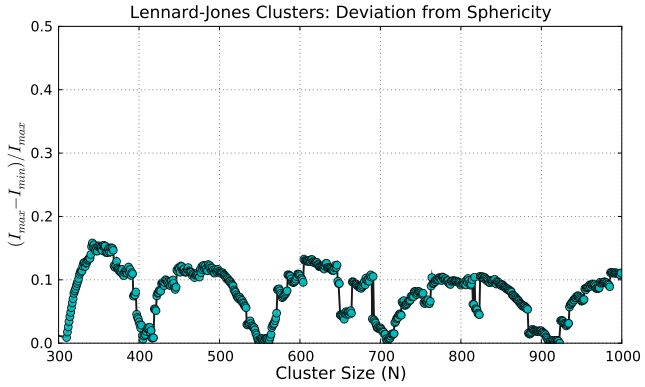

(a) deviation from sphericity for $\mathrm{LJ}_{300-1000}$

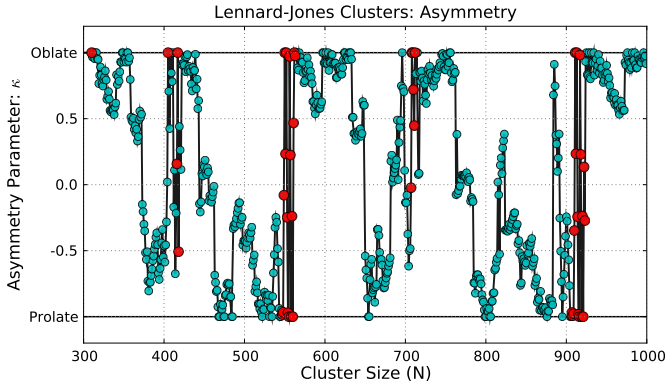

(b) Ray's asymmetry parameter for $\mathrm{LJ}_{300-1000}$

Figure 3.8: Descriptive statistics of larger Lennard-Jones clusters

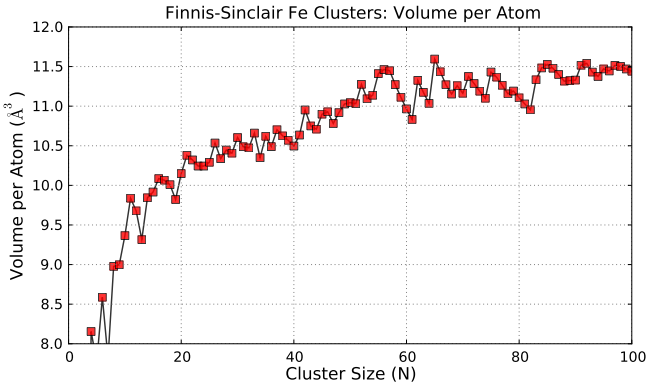

(a) volume per atom FS_{3--100}

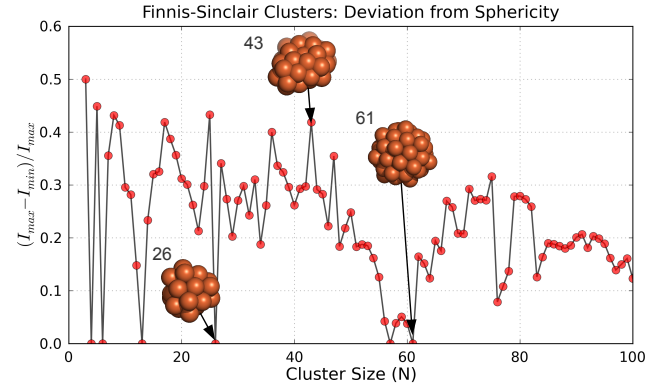

(b) deviation from sphericity for FS_{3--100}

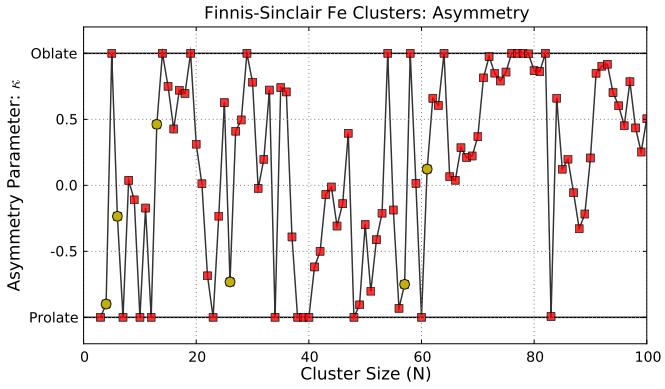

(c) Ray's asymmetry parameter for FS_{3--100}

Figure 3.9: Calculation of the sphericity for cluster structures obtained by applying global optimization techniques to atoms interacting under the Finnis-Sinclair potential [55]

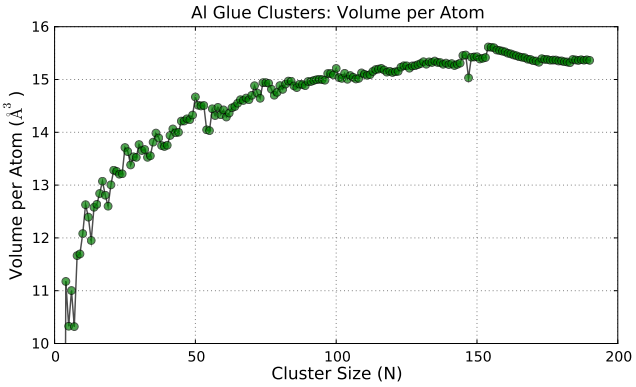

(a) volume per atom Al Glue_{3--100}

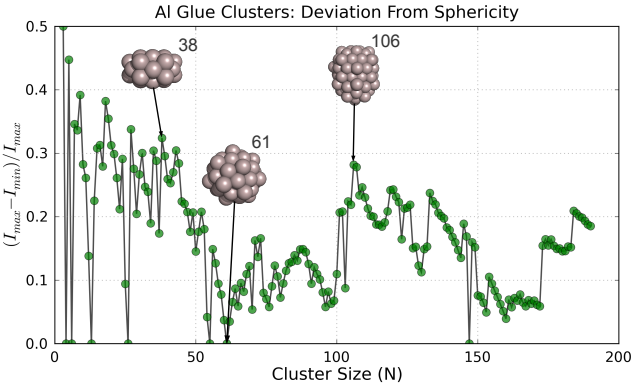

(b) deviation from sphericity for Al Glue_{3--100}

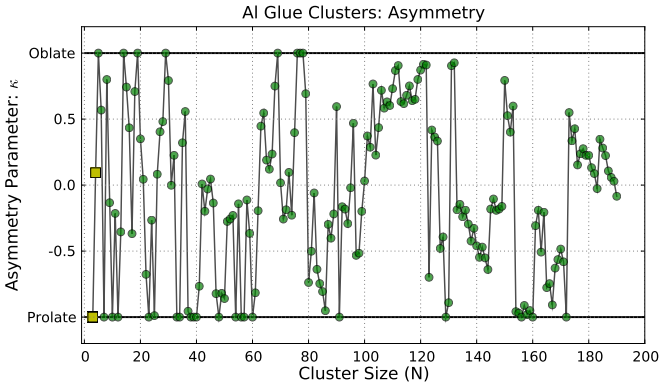

(c) Ray's asymmetry parameter for Al Glue_{3--100}

Figure 3.10: Same calculation as above for Al Glue clusters. This glue potential is described in refs. [47, 46], it is known to favor a polytetrahedra growth sequence where the atoms are arranged at the vertices of interpenetrating tetrahedra.

3.5 Adiabatic Magnetization by Avoided Crossing

For analysis of Stern-Gerlach magnetic deflection experiments the Langevin susceptibility Eq. 3.19 is used to relate the intrinsic moment of a ferromagnetic cluster to the average magnetization through the temperature and applied field. This formula is derived from statistical mechanics of a rotating dipole in a magnetic field.

$$\frac{\bar{M}}{\mu} = \left(\coth\left(\frac{\mu N B}{kT}\right) - \frac{kT}{\mu B}\right) \tag{3.19}$$

This is exactly the susceptibility that would obtain for a superparamagnetic particle relaxing in a magnetic field with temperature T. At the lowest temperatures in our experiments (20 K), superparamagnetic relaxation is impossible because there is no heat bath for the particle to interact with[168].

An alternative justification for the use of the Langevin susceptibility at low temperatures has been given by Xu [168]. In this theory the Zeeman curves of the cluster overlap with one another and avoided crossings with higher unpopulated levels cause the slopes of the populated states to trend downward. (see Figure3.11)

The average of the magnetization distribution in the low field limit amazingly has the same value as the Langevin low field limit!

$$M \approx \frac{\mu^2 B}{3kT} \tag{3.20}$$

The evidence from many years of work on cobalt, iron, and nickel clusters support the idea that the Langevin susceptibility applies at cryogenic temperatures where superparamagnetic relaxation is no possible. The agreement of the Langevin susceptibility with the observed magnetizations over a large range of fields and temperatures is shown in Figure 3.11. This includes temperatures where the vast majority of the clusters in the beam are in their electronic and vibrational ground states. Thus there is no heat bath for spin relaxation.

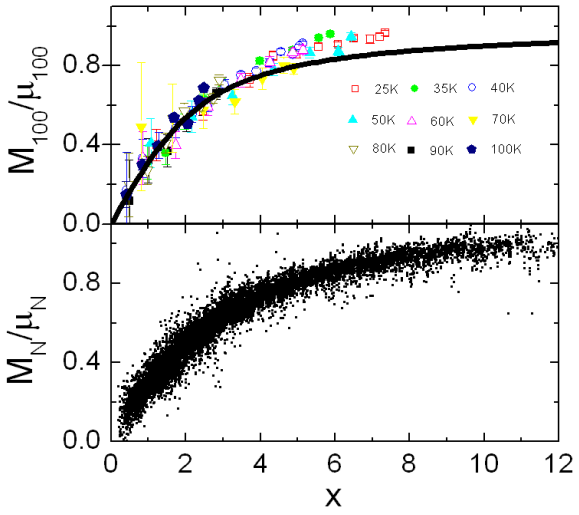

(a) Plot of magnetization of Co clusters with Langevin function

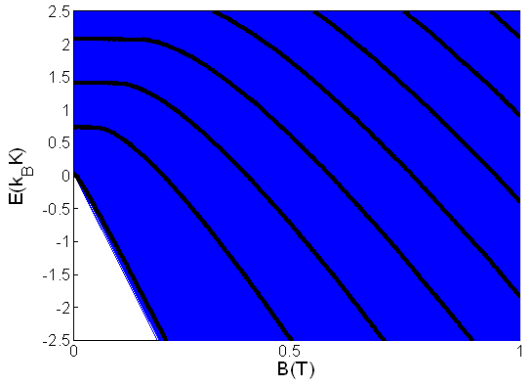

(b) Zeeman diagram for a ferromagnetic cluster

Figure 3.11: Demonstration of adiabatic magnetization for Co clusters. The observed magnetizations are plotted against the Langevin curve. The figure to the right shows how this magnetization process emerges from the adiabatic tracing of the Zeeman diagram, with no spin relaxation. Figures gratefully borrowed from Xu [168]

3.6 Cluster Temperature

The issue of cluster temperature critical to the correct interpretation of the deflection experiments, because the deflection profiles observed reflect the thermal conditions of the cluster source. A related issue is whether it is possible for any form of thermal relaxation to take place for a cluster isolated in a molecular beam.

What exactly is meant when one refers to the "temperature" of a cluster beam? Each cluster in the beam is uncoupled from the surrounding environment and has a fixed total energy. The total energy of each cluster was fixed when it left the cluster source. The probability that it had total energy E when it left the source is given by the Boltzmann distribution $p(E) \propto e^{-E/kT}$. Thus the ensemble of clusters in the beam has energies distributed according to the source temperature. When one refers the temperature of the cluster beam, one is referring to the distribution of individual cluster energies found in the beam. This is determined in the cluster source.

How do we know that the distribution of energies is close to the source temperature?

There have been several methods used to validate the cluster temperature. One simple example is to use the formation and dissociation of rare-gas complexes in the beam [108], as a measure of temperature.

Alternatively, it is possible to use the magnetization of a beam of ferromagnetic clusters as a thermometer for the cluster beam. The idea is to vary the dwell time until there is no change in the moments calculated from the Langevin susceptibility. For dwell times longer than this it is reasonable to believe that the clusters are in thermal equilibrium with the source. This condition is found to hold for dwell times on the order of 1 ms.

Obviously we have not verified the temperature of the cluster beam using these methods for every experimental run. In practice, we select valve and gas pulse settings so that the dwell time is in the 1 - 2 ms.

Theoretical calculations of the relaxation time for the different degrees of freedom in a cluster support the view that 2 ms of dwell time is sufficient for the clusters to come to

equilibrium with the source temperature.

CHAPTER IV

DIPOLE MOMENTS AND CLUSTER METALLICITY

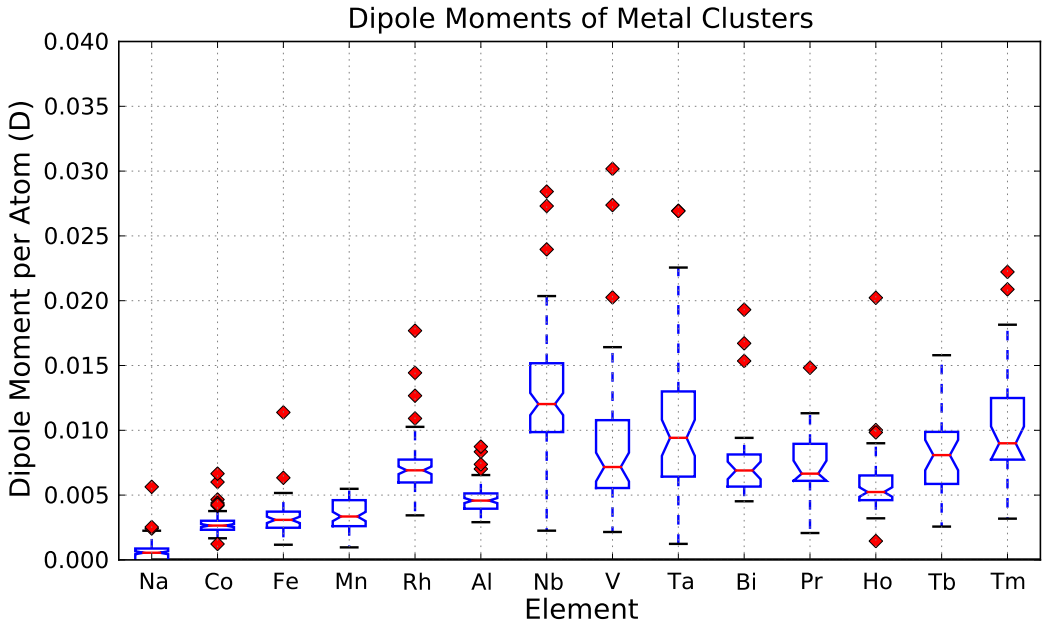

Figure 4.1: Dipole moments per atom for metal clusters of 15 elements. The box plot provides a summary of the distribution of per atom dipole moments. The line in the middle of the bar is the median value for the clusters measured, and the upper and lower bounds of the bars represent the range that contain the upper and lower quartiles. The red diamonds are the magnitude of the outlier points. An important caveat is the distribution for different elements is over different size ranges. For example the Na distribution is over $N = 1 - 250$ while Bi includes $N = 3 - 35$. Thus this comparison is possibly misleading. This plot is just to provide a quick summary of the results of this chapter.

In this chapter we present a series of electric deflection experiments on small metal clusters (mostly $N < 100$) of 14 different elements at beam temperatures from 20 - 50 K. These experiments allow us to determine their static polarizabilities and estimate the magnitude of their permanent dipole moments. The results of these measurements are summarized in Figure 4.1. Our measurements include the simple alkali metal Na, $3d$ transition metals

Mn,Co,Fe, a 4*d* transition metal Rh, the group V transition metals (V, Nb, and Ta), Al and Bi, as well as 4 lanthanides (Pr, Tb, Ho, and Tm).

As discussed in chapter 1, our motivation for these measurements is to test how effectively the delocalized valence electrons of a metal cluster can screen inhomogeneities in the cluster's charge distribution. A perfect metal sphere will have $E = 0$ everywhere in its interior and thus have a net dipole moment that is exactly zero. Of the materials we have tested, Na clusters come closest to this ideal. Fe, Co, and Mn clusters the data show very small dipole moments ($\approx 0.001 - 0.002$ D/atom).

Rh_N shows a qualitatively clear beam broadening for nearly all cluster sizes up to $N = 80$. These dipole moments computed from this broadening are repeatable and independent of field and temperature up to $T = 50K$. The constant per atom dipole moments implies that the total dipole moment increases with cluster size. We must therefore be far from the bulk limit as, all bulk metals have $E = 0$ in their interior. These dipole moments are further reflected in an increasing trend in the polarizability for Rh_N.

The rare earths Pr, Tb, Ho, and Tm show larger per atom dipole moments up to around $0.01D$ / atom. These dipole moments are in some isolated cases enhanced by the addition of an oxygen atom as in Tb_N, and Tm_N, Pr_N.

Bi_N shows a very strong odd-even alternation with even-N clusters having larger per atom dipole moments than their neighbors. The dipole moments for Bi_N are computed from a series of measurements taken over a range of measurements from 20 - 60 K. Unlike Nb,V,and Ta the dipole moments do not appear to vary significantly with temperature in this range.

Another key observation is the exceptionally of Nb, V, and Ta compared with the other transition metal systems that have been studied. Their per atom dipole moments are larger than the other materials, and there is a strong the odd-even alternation in the magnitude of the dipole moments with the even-N clusters showing consistently larger dipole moments than their odd-N neighbors. The temperature dependence of these dipole moments strongly

suggests that the mechanism of the polarization of these particles is very different than that of the other elements, which are insensitive to temperature in the ranges considered. Nb_N, Ta_N, and to some extent V_N all show a significant reduction of the dipole moment as the temperature is increased from 20 to 40 K. To explain the disappearance of these dipole moments at such low temperatures requires a physical mechanism which operates at an energy scale much lower than the lattice vibrations ($\frac{\hbar\omega_D}{N} \approx 100K$) or electronic transitions ($\frac{E_F}{N} \approx 5.3eV/N \approx 60,000K/N$).

There is also a slight correlation between the magnitude of the per atom dipole moments and the atomic mass, with heavier elements showing larger per atom dipole moments. However, it must be cautioned that this comparison is possibly misleading because different elements shown in Figure 4.1 cover different size ranges. (Na includes $N < 250$ while Pr covers only $N < 35$)

For many elements the polarizabilities and dipole moments as a function of cluster size show large variations and there are some special cluster sizes which show much larger dipole moments than their neighbors. (These outliers are shown as red dots in Figure 4.1) These large variations are most pronounced for smaller cluster sizes where the ionic and electronic structure of clusters is expected to vary significantly with the addition of a single atom.

Almost all of the clusters studied have polarizabilities that are significantly larger than their corresponding bulk materials, thus these clusters are still far from converging to the bulk limit. The polarizability is a rough measure of the volume per atom (the bulk values are derived from the bulk density), but even if the density for a cluster is the same as that of a bulk material, there are several other effects that can cause an enhancement in the polarizability. Examples include the electronic spillout [21, 97], ellipsoidal jahn-teller distortions [34, 91], and the dipole moment itself, which can become partially aligned with the deflection field as it rotates in the field.

The bulk and atomic polarizabilities are given in table 4.1. If there was no bonding or

Table 4.1: Bulk and Atomic Polarizabilities: M is the molar mass, ρ is the density of the elemental solid measured at a temperature of 25 C. The bulk polarizability is calculated by applying the formula $\alpha = 4\pi\epsilon_0 R^3$, where the radius R is the radius of a sphere containing one atom. The volume of this sphere is calculated from the molar mass and density. The atomic polarizabilities with a †, are derived from quantum chemical calculations and their precision is is estimated at 25%. The polarizabilities of Na and Al are derived from atomic interferometry [50], and beam deflection experiments [110] respectively.

Element	M (g/mol)	ρ (g/cm^3)	α_{bulk} (Å^3)	α_{atom} (Å^3)
Na	22.99	0.968	9.415	24.08
Al	26.98	2.700	3.961	6.80
V	50.94	6.110	3.305	12.4†
Cr	62.00	7.150	3.437	11.6†
Mn	54.94	7.300	2.983	9.4†
Fe	55.84	7.870	2.813	8.4†
Co	58.93	8.860	2.637	7.5†
Ni	58.60	8.900	2.610	6.8†
Y	88.91	4.470	7.885	22.7†
Nb	92.91	8.570	4.298	15.7†
Rh	102.91	12.40	3.290	8.6†
Ta	180.95	16.40	4.374	13.1†
Au	196.97	19.30	4.046	6.15†
Pb	207.21	11.30	7.269	6.8†
Bi	208.98	9.800	8.462	7.4†
Pr	140.91	6.770	8.251	28.2†
Tb	158.93	8.230	7.655	25.5†
Ho	164.93	8.800	7.430	23.6†
Tm	168.93	9.320	7.186	21.8†

charge transfer between the atoms in a cluster of N atoms then we would expect the cluster to have α/N equal to the atomic polarizability α_{atom}, just as for a rare gas solid.

There have been many earlier electric deflection experiments on pure metal clusters [134, 133, 135, 11, 88, 85, 87, 149, 91, 129]. However only [134, 133, 135] attempted to extract the dipole moments by an analysis of the beam broadening. Their findings for Pb_N and Sn_N clusters are similar to the results reported here and complement them nicely.

In our measurements, we subtract a correction from the broadening to account for the the inhomogeneity in the deflection field. We equate the residual broadening that remains

after subtracting this correction to a permanent dipole moment. For Na clusters this correction accounts or all of the broadening and the residual broadening fluctuates around zero. In many cases we independently calibrate this correction with the atomic beam that is present with the clusters for Al, Pr, Tb, Ho, and Tm. Atoms cannot have static dipole moments because their quantum states are eigenstates of the angular momentum operator, thus any beam broadening present in the atomic beam must be due to an experimental artifact. For cases where the atomic beam is present the field broadening correction accounts for nearly all of the broadening of the atom beams.

Whether the dipole moments are exactly zero is a critical question. In the elementary model of a metal the mobile delocalized charges will move until the internal electric field of the metal is exactly zero. A cluster in this condition should have zero dipole moment. Therefore a non-zero dipole moment implies the existence of unscreened electric fields, and non-metallicity.

The formation of a dipole moment in a finite cluster depends on a delicate balance of electrostatic forces. To sustain the charge separation and electric fields of a dipole moment, the electrostatic energy of the dipole $E = \frac{p^2}{3\epsilon_0 V}$ must be compensated for by some countervailing force which prevents the charges from moving to cancel the internal electric field. An obvious candidate is the binding of electrons in covalent bonds, but there are other possibilities related to charge density waves [64, 31, 151]. (although this is quite speculative)

For clusters derived from transition metals with partially filled d orbitals (such as Mn, Fe, Co, and Ni), the d electrons will show a tendency to be partially localized in bonds. This tendency toward localization is a key factor in the ferromagnetism of these clusters [80, 152, 119, 118, 65].

Electric dipole moments are ubiquitous in covalently bonded molecular systems [155], unless a dipole moment is forbidden by symmetry [150]. Many of these systems contain bonds between atoms with different electronegativities and so the bonds themselves have

an electric dipole moment. In a transition metal cluster, with partially covalent bonding, it would be quite a fortuitous accident if the charge density of the bonding electrons had exactly the same center of charge as the ion cores!

In the case of a simple alkali metal like Na, the electrons are all derived from *s* orbitals and they are almost completely delocalized throughout the body of a cluster. The delocalization is so great that alkali clusters can be described effectively with a shell model analogous to that for atoms and nuclei. In these systems, such as Na_N, the energetics and degeneracies of the electronic shell structure determines the structure of the ion cores rather than the other way around. We will find that as expected Na clusters have zero dipole moment. The other cluster systems considered are more complex and will be discussed in greater depth below.

4.1 Sodium clusters

To introduce our data, we begin with Na clusters. Na is an alkali metal with a single unpaired *s* electron bound to a Ne^+ core. Na is called a "simple" metal [6] because so many of its properties (conductivity, cohesive energy, optical response, paramagnetism) can be well explained by a free electron model, where the delocalized *s* electrons move independently of one another. Their motion is only weakly perturbed by the interaction with the lattice of ion cores. The success of this model is due to the strong delocalization of the *s* electrons. The free electrons further weaken the influence of the charged ionic cores by screening.

There is an abundance of experimental evidence (see [39], or [106] for a review) that this delocalization persists down to the smallest Na clusters. Thus the properties of Na clusters can be explained qualitatively using a simple shell model [92, 34] that is analogous to the nuclear shell model [**?**]. Nearly quantitative agreement with experiment can be achieved with more advanced models, such as deformed jellium [21], or calculations which include the optimized ionic structures with pseudopotentials (see [14] for an early example,

and refs. [146, 106] and the references therein for later examples)

The electronic shell structure has a dominating influence on the geometry of Na clusters, due to the Jahn-Teller effect [34]. A spherical Na cluster with a partially filled electronic shell can lower its electronic kinetic energy by elongating along one axis and filling the electrons into the orbitals which are spread out along this axis. These distortions are well known from molecular and nuclear physics. Just as for atoms, the electronic structure of Na clusters can be constructed by filling the electronic orbitals one at a time. The single particle states can even be accurately described as eigenstates of the quantum angular momentum operator as demonstrated by a recent angle resolved anion photodetachment experiment [7] which conclusively shows that electronic states in Na clusters have well defined angular momentum, similar to atoms.

At 20 K, we find that almost all Na clusters have zero dipole moments within our experimental error. This result is not surprising from the perspective of the jellium model [21, 106], but there have been quantum chemical calculations [146] which predicted that nearly all of the smaller Na clusters $N < 20$ would have dipole moments, some as large as of 1 D. These calculations are based on all-electron Hartree-Fock with perturbative corrections and DFT with generalized gradient functionals to attempt to account for the effects of electron correlations. The ionic structure was optimized as well to improve the realism. Our experiment establishes an upper bound on the dipole moments of Na clusters that is in many cases an order of magnitude smaller than the values predicted by these calculations. Na_N is by far the simplest and most thoroughly studied cluster system, so this result demonstrates the care and subtlety required to theoretically predict a quantity like the electric dipole moment.

4.1.1 Overview of Sodium

Sodium clusters were the first cluster system to be extensively investigated using molecular beam methods [142, 143, 42, 92]. The physical properties which have been studied include

- **Abundance Spectra** [92, 120, 105] which reveal differences in binding energy when the cluster beam is populated from an evaporative ensemble. This ensemble comes about by the following process. If the abundance distribution in a beam is initially log-normal, and the clusters have an average energy that is larger than the binding energy, then atoms will evaporate until the excess energy in each cluster is less than the binding energy. Thus cluster sizes with larger binding energies will see less depletion and larger abundance in the mass spectrum.

- **Static Dipole Polarizabilities** which are sensitive to the volume of a cluster and the electronic "spill-out". This quantity can be measured by an electric deflection experiment as in [91, 149].

- **Photoabsorption Cross Sections** [143, 142, 19, 136] The absorption of visible light as a function of wavelength has been measured by beam depletion. A cluster beam is illuminated with light of a specific wavelength. The absorption of a single photon significantly heats the cluster and will cause evaporation. The cross section for photoabsorption can thus be measured by plotting the beam depletion as a function of wavelength. These experiments revealed the existence of large collective dipole resonances in the visible spectrum that are closely related to the bulk surface plasmon. (evidence that the normally optically inaccessible "volume plasmon" has been recently presented in [165] The Mie theory of the surface plasmon is:

$$\omega_s = \sqrt{\frac{e^2}{m_e r_s^3}} \tag{4.1}$$

This formula can be derived by inserting the dielectric function for a plasma

$$\epsilon(\omega) = 1 - \frac{\omega_p^2}{\omega(\omega + i\Gamma)} \tag{4.2}$$

Into the formula for the polarizability of a dielectric sphere

$$\alpha = R^3 \frac{\epsilon - 1}{\epsilon + 2} \tag{4.3}$$

To yield

$$\alpha(\omega) = R^3 \frac{\omega_P^2/3}{\omega^2 + i\omega\gamma + \omega_P^2/3} \tag{4.4}$$

The above simple derivation is well-known and the form given above is due to Bertsch. We mention it because this relation between the moments of the optical resonances and the static-polarizability can be used to provide an alternative experimental method for measurement of the static dipole polarizability. This procedure has been used by Haberland [136], and the estimated polarizability agrees very well with the results of a deflection measurement.

The Mie theory gives the correct intuition for these giant resonances Brut more advanced theories [170] are required to correctly account for the asymmetric lineshapes and damping mechanisms.

- **Ionization Potentials** [76] can be measured by recording the ionization efficiency as a function of wavelength with a tunable laser. The threshold energy is interpreted as the baseline intercept of the post-threshold ionization efficiency curve [39]. The IP measurements of Na_N clusters clearly show jumps at electronic shell closings and a very interesting odd-even alternation as large as 0.1 eV. Odd-even alternations have been observed in nuclear physics, and have been explained by a pairing mechanism similar to the BCS theory of superconductivity[17]. However it is unlikely that this could be the explanation of the oscillations for Na clusters because the 0.1 eV energy gap is nearly 100 times larger than the energy for BCS type pairing. The odd-even gap has been explained by Häkkinen et. al. [67] as a shape deformation effect.

- **Caloric Curves and Melting Temperatures** [137, 96, 66, 66, 73, 138] The caloric curve for a system is a plot of the average energy as a function of temperature. In a free cluster, each individual cluster has a fixed total energy (a microcanonical ensemble), so the "temperature" refers to the temperature of the source where the clusters come to thermal equilibrium before being isolated in a beam. In these experiments

the clusters are size selected before being warmed with a laser. The heating laser causes a number of atoms to evaporate, and a histogram of the number of evaporated atoms is plotted as a function of the number of photons absorbed. Each photon deposits a known amount of energy to the cluster so the the distribution of evaporated atoms allows a measurement of the distribution of cluster energies before they were heated with the laser. Smooth thresholds in the caloric curves are the finite system counterpart to the melting curve. The melting temperatures of Na clusters show very interesting size dependencies.

- **Energy and Angle-Resolved Photoelectron Spectra** [161, 7] anion photoelectron spectroscopy provides a nearly direct measurement of the density of electronic states in a cluster. Na clusters show large near degenerate peaks in the density of states each of which corresponds to a single electronic shell. These methods thus provide a direct method for the observation of the electronic shell structure. The angular distribution of the emitted photoelectrons with respect to the polarization of the photodetachment laser depends on the angular momentum of initial state of the detached electron. Electron imaging experiments like [7], have concluded that the electronic states of Na clusters have the character of angular momentum eigenstates.

This list is by no means complete, and there are many other properties of Na clusters which have been investigated. The point is to give a sense for how strong the evidence is for the shell structure of Na clusters, and how essential the shells are for the understanding of their properties. Again we should emphasize that achieving quantitative agreement with experiment requires carefully accounting for the structure of the ion cores as in [93].

4.1.2 Experimental Considerations

The mass spectrum for the beam of Na clusters is shown in Figure 4.2. This mass spectrum was recorded using the KrF excimer wavelength of 248 nm (5.02 eV), the source temperature was 20 K, thus the Na clusters are close to their vibrational ground state. The

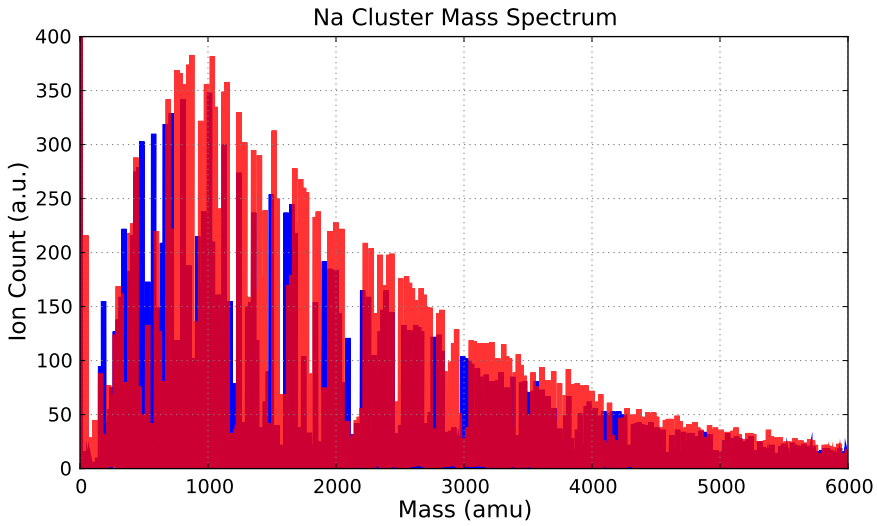

Figure 4.2: Mass spectrum for Na clusters produced at 20 K using laser vaporization (532 nm) and ionized with laser wavelength of 248 nm (5.02 eV). Note that the cluster size distribution shows a strong log-normal shape, unlike the evaporative ensemble observed in refs.[92]

distribution of cluster sizes follows a log-normal distribution which reflects the nucleation conditions and the kinetics of cluster growth in the source [145]. The log-normal size distribution is very different from the "evaporative ensemble" that emerges from gas aggregation source after laser heating [105]. A size distribution similar to this log-normal distribution has been observed before by Honea & Homer [76] using a liquid nitrogen cooled laser vaporization source.

At a photon energy of 6.45 eV (ArF excimer) no Na cluster intensity was observed. The single ionization potential for Na clusters (N > 20) is in the range of 3.2 - 3.6 eV [39]. Thus a 6.45 eV photon is well above the threshold, and contains enough residual energy to cause a significant heating of the cluster ion. This heating can lead to evaporation. If the cluster was double ionized it is also possible that fission processes could take place as well.

Regardless, when using 248 nm light, we observe clean mass spectrum of pure Na clusters with little oxide or hydroxide contamination and no double ionization. The lack of contamination is due primarily to the low temperature of the cluster source, which freezes

out reactive impurities in the carrier gas, and the preparation of the Na sample under an argon atmosphere.

Another noteworthy mystery is that the intensity of the Na atom beam is so weak while the intensity of the Al atom is so intense. As seen in table 4.1, the polarizability of the Na atom is nearly 4 times larger than the Al atom, so it's scattering cross section is correspondingly larger and thus the Na atomic beam would show much larger depletion. It is also possible that all of the atoms emitted from the laser vaporization source are charged, and since our beam is designed for neutrals there are many stray electric and magnetic fields which would certainly remove any charged species from the beam. Another possibility is that most of the Na atoms are consumed in cluster growth.

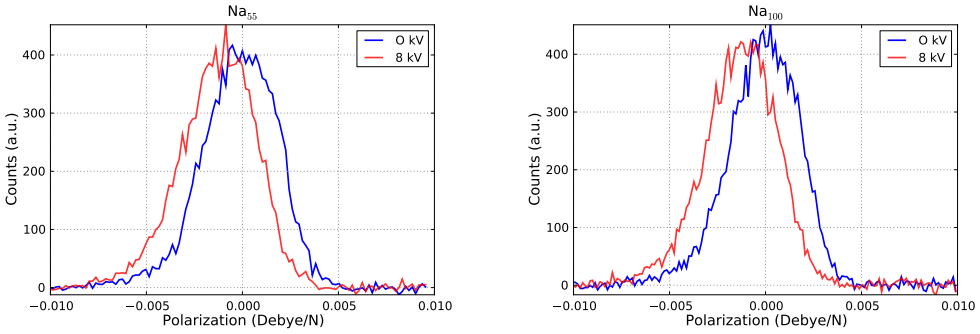

Figure 4.3: Electric Deflection Profiles for Pure Na_N Clusters, recorded at a temperature of 20 K. These two profiles are typical of all of the Na deflection profiles measured. There is a rigid shift of the deflection profile, with very little broadening of the beam. The scale of the deflection profile has been converted from mm to units of Debye/atom using the formula $\frac{P}{N} = \frac{\delta m_a v^2}{\nabla E K_\alpha}$. In the profiles shown, δ is the displacement away from the center of the beam, The polarizability is then found by $\frac{\alpha}{N} = \frac{P}{E}$.

Two typical deflection profiles for Na clusters are shown in Figure 4.3.

4.1.3 Polarizabilities and Dipole Moments

Our measurement of the polarizability of Na_N is shown in Figures 4.4 and 4.5. The decreasing trend has been noted in the previous measurements and is explained by the electronic spill-out.

The oscillations about the decreasing trend are also quite interesting. First, it should be noted that the locations of the maxima and minima closely track the maxima and minima observed by Borggreen in the Na cluster separation energies [20]. The local minima in Figure 4.5 correspond to the well-known spherical closed shell clusters. Part of the magnitude of the oscillations in the polarizability can be accounted for by ellipsoidal Jahn-Teller distortions [1], but rough estimates from the Clemenger-Nilsson model with a harmonic potential model due to Liang, indicate that these enhancements are too small to account for the full amplitude of the oscillations.

Similar oscillations have been observed even in the *spherical* Jellium model in a calculation due to Puska et. al. [124]. While the evidence for ellipsoidal distortions from photoabsorption [136] and photoelectron [93] experiments is not in doubt, this spherical jellium result suggests that the oscillations in the polarizability can be explained by electronic effects.

An explanation due to ref. [124] makes use of the fact that the polarizability increases with the volume of wavefunction of the highest filled electronic state. The local minima of the polarizability curve correspond to closed electronic shells. The increase in the polarizability after a shell-closing corresponds to the filling of a new subshell. Why would the size of an electronic wavefunction increase? Recall that the wavefunction with radial quantum number n and angular momentum quantum number l must be orthogonal to all other eigenfunctions. For the wavefunction n, l to be orthogonal to all other wavefunctions with $n = 0, ...n, l$ it must spread out radially. It is claimed that this increase in the radius of the wavefunction is responsible for the increase in polarizability as a new subshell is filled. The decrease after the local maxima correspond to the filling of a new subshell with a value of l that is unoccupied for every lower principal quantum number. Because these wavefunctions to not have to preserve orthogonality with lower shell wavefunctions with

[1] The polarizability in Figures 4.4 and 4.5 is an average of the polarizabilities along each of the principal axes. Thus an ellipsoidal distortion can give a slight enhancement.

the same value for l they can be packed in a lower radius.

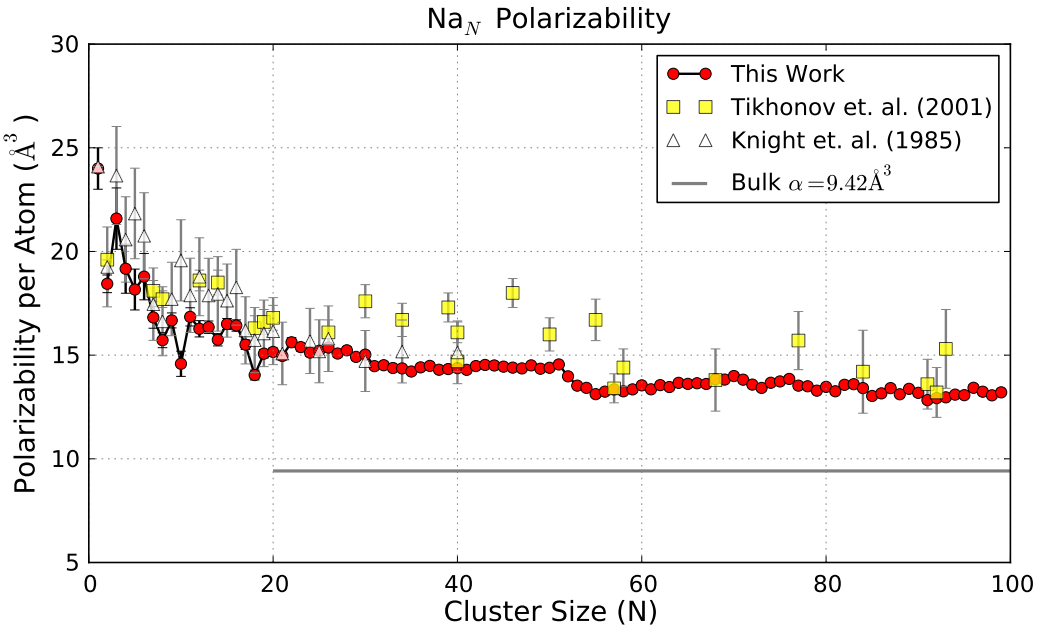

Figure 4.4: Polarizabilities of Na_N at a beam temperature of 20 K. These are derived from our electric deflection experiment, and represent the average of 6 experimental runs. The polarizability of Na clusters have been measured many times - The first measurement is due to Knight et. al. [91]. Also shown is a recent measurement due to Tikhonov et. al. [149]

There have been several experimental measurements of the polarizability of Na_N [91, 129, 149],, a comparison between these measurements and our data is plotted in Figure 4.4. Our measurements represent a large improvement over the previous measurements. The higher quality of this measurement is due to the low temperature, and the convenience of the position sensitive detection technique which allows the deflections of all cluster sizes to be measured simultaneously. While it has been predicted that the polarizability of Na clusters will change with temperature [15] due to a phenomenon related to thermal expansion, the key advantage of the low beam temperature is that the velocity of the beam is much slower ($\approx$ 300 m/s). For a constant deflection field a slower beam will show larger deflections and thus a smaller fractional error.

There are some important caveats to the measurements above. The trimer Na_3 is a

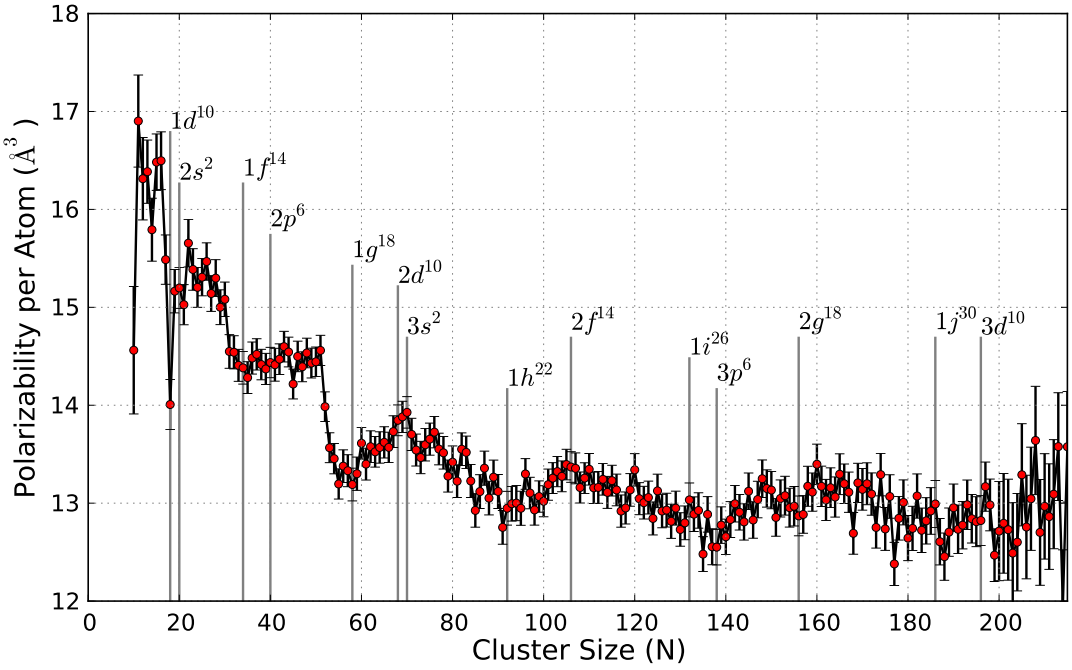

Figure 4.5: Polarizabilities of Na_N (N = 10-250) at a beam temperature of 20 K. The shell structure of the clusters is visible in the oscillations about the descending trend. At N = 250 the clusters are still far from the polarizability of bulk Na metal which is 9.6 Å$^3/N$.

classic example of a vibronic system, where the motion of the electrons and ions cannot be separated (the Born-Oppenheimer approximation). The normal modes of the ions can combine to form a type of motion where each ion moves in a circle about the vertices of an equilateral triangle. This motion has spectroscopic consequences due to the phase shift of the electronic wavefunction that accumulates as the ions complete each cycle of their motion [101, 71]. This system has been investigated for Na_3 and Li_3, with optical spectroscopy [25, 159, 24], and measurements of the hyperfine shifts in molecular beam ESR experiments [72].

Because of this internal motion, it is possible that the time averaged projection of an electric dipole moment would be different than what would be expected from a rigid rotor model. Thus the dipole moment derived from the beam broadening could be an underestimate. If this were the case the presence of an electric dipole moment would be seen as an enhancement of the polarizability, which is what we observe in Figure 4.4.

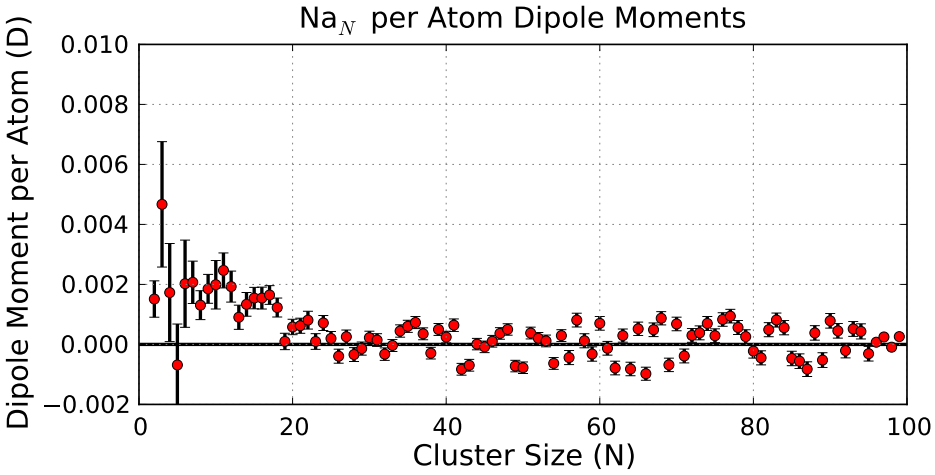

(a) Dipole moments per atom for Na_N recorded at a temperature of 20 K.

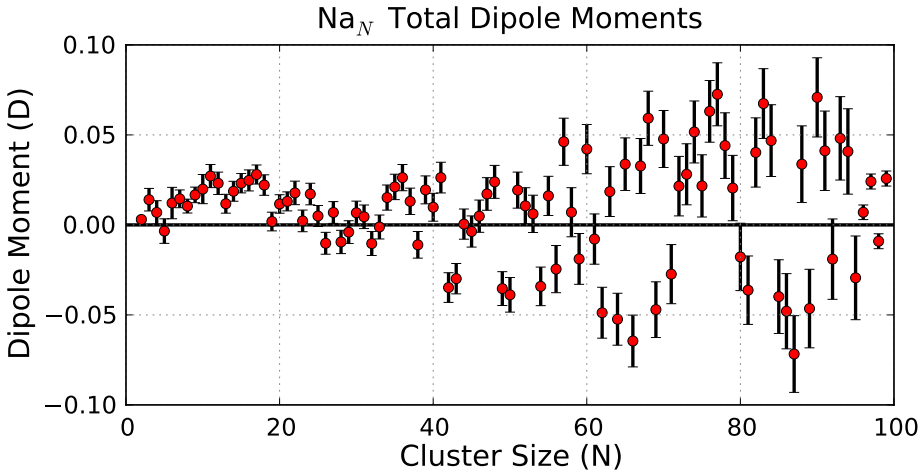

(b) Total Dipole Moments for Na_N

Figure 4.6: Per atom and total dipole moments for Na clusters. These dipole moments are estimated from the broadening of the molecular beam in an electric field. A small correction is applied to the

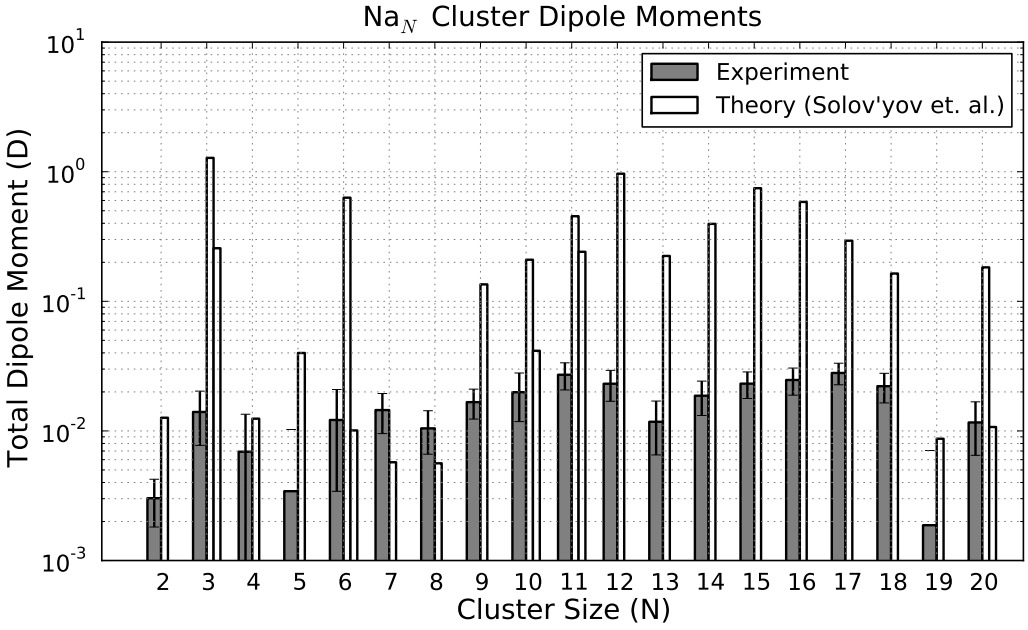

Figure 4.7: Comparison between the theoretical dipole moments calculated in ref. [146] and the dipole moments determined from the residual beam broadening. In order to clearly illustrate the magnitude of the difference between theory and experiment they are plotted on a log scale. Clearly, the methods used in ref. [146] give a false overestimate of the dipole moment. This is quite puzzling because the calculations in ref. [146] show excellent agreement with experiment for the polarizability and ionization potentials. Many of the structures for $N = 14-20$ are predicted to be symmetric tops, so if we assume the structures are optimized then our measurements have quantitative significance.

It is also notable that there are two isomers predicted for Na_6 in ref. [146] one is a planar triangle with zero dipole moment, and the other is a pentagonal pyramid with a dipole moment of around 0.5-0.6 D. The calculated energy difference between these two isomers is large enough that we should only see the lower energy isomer at a source temperature of 20 K. However we do observe an anomalous loss of beam intensity when the electric field is turned on for Na_6. This intensity loss has been observed in multiple experiments, and in some cases half of the beam intensity is depleted. This can be explained if there are two isomers for Na_6 in the beam, one with a dipole moment and one without.

4.2 Niobium, Vanadium and Tantalum: Metal cluster Ferroelectricity

Vanadium, Niobium, and Tantalum clusters all lie in the same column (Group V) of the transition metals. It was found by Moro et. al. [111] that at low temperatures nearly all of the clusters $N < 200$ have electric dipole moments.

The early deflection experiments reported in ref. [111], estimated the dipole moments from the depletion observed in the beam with the detector. Later measurements, reported in [172, 169], were careful to observe the complete tails of the deflection profiles estimated the dipole moments to be on the order of 0.1-0.2 D/atom.

Example deflection profiles for several Nb clusters from different size ranges are shown in Figure 4.8. The profiles are very different from the Na cluster deflection profiles shown in Figure 4.3.

This is a very interesting effect, and it is important to view it in the context of the other elements. We briefly summarize the experimental facts about the Nb cluster dipole moments, for more details see refs [172, 169, 112, 111]

- As seen in Figure 4.8, the deflection profiles show a long asymmetric tail, and a central peak. The maximum extent of the tail is linear in the electric field. (which corresponds to a dipole completely aligned or anti-aligned with the field)

- The beam broadening is sharply reduced as the temperature is increased (Figure 4.2, and Figure 4.2.1). This was interpreted to mean that above a certain temperature, the clusters become non-polar. For this reason, we refer to the clusters as *ferroelectric* . The dipole moments show significant reductions starting at very low temperatures (50-100 K) which suggests that the energy difference between the ferroelectric and non-polar state is minuscule $\approx$ 10 meV.

- Stern-Gerlach magnetic deflection experiments on Nb_N at low temperatures have shown that the odd-N Nb clusters have a magnetic moment of $1\mu_B$, just as would

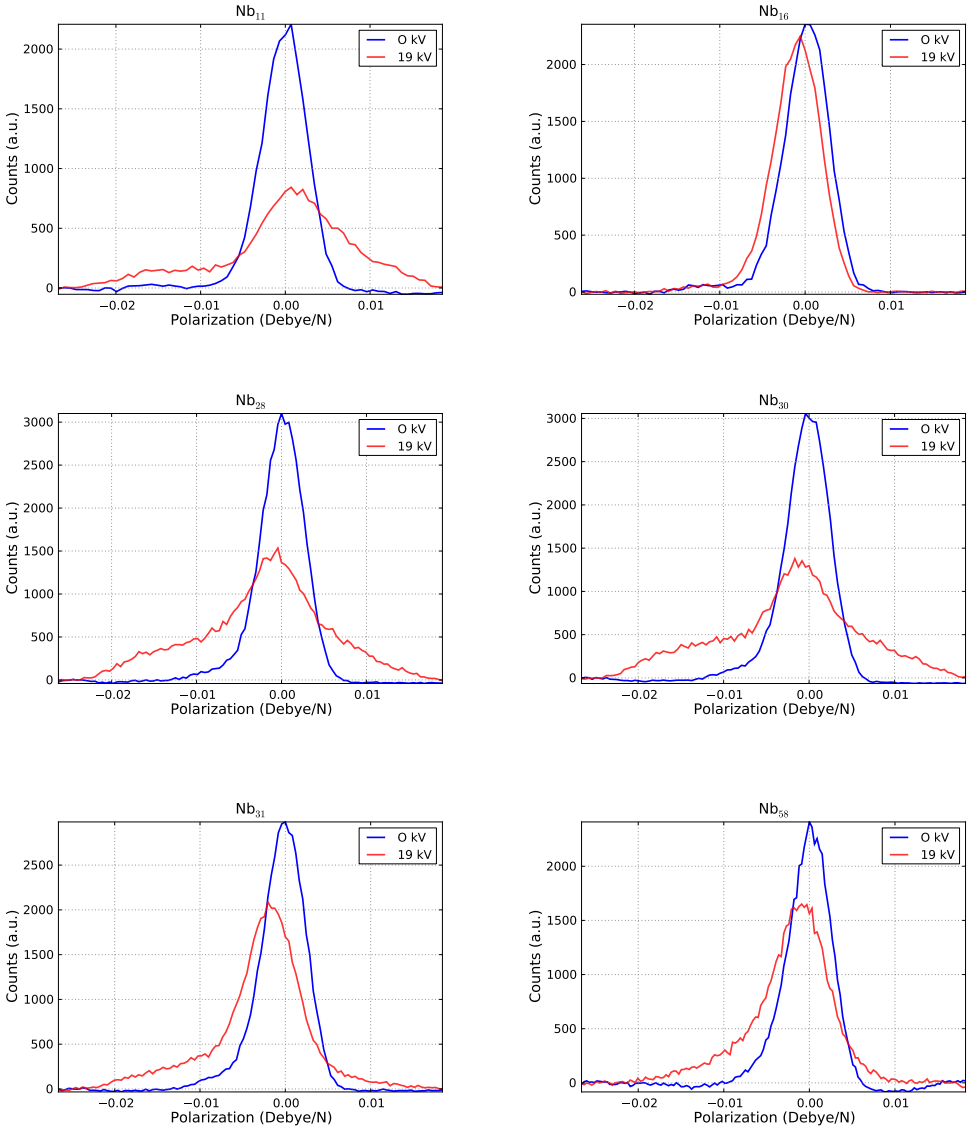

Figure 4.8: Electric Deflection Profiles for Pure Nb_N Clusters, recorded at a temperature of 20 K. These are measurements of the complete deflection profiles, and there is no area loss. Many of the clusters show two sided deflections. We have tried to show representative examples for N = 11, 16, 28, 30, 31, and 58. See the graph of dipole moments for a better summary. Especially interesting is N = 11, which shows an average deflection toward the low field direction, which implies that it is polarized anti-parallel to the applied electric field.

be expected as electrons are paired by spin-up and spin-down in orbitals. The quantitative change in the second moment of the deflection profile indicates that this spin is uncoupled from both the cluster lattice [112] and the total angular momentum.

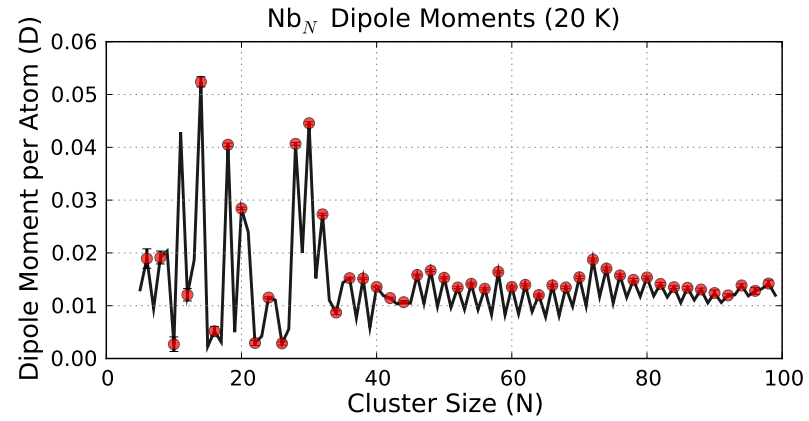

(a) Dipole moments per atom for Nb_N recorded at a temperature of 20 K.

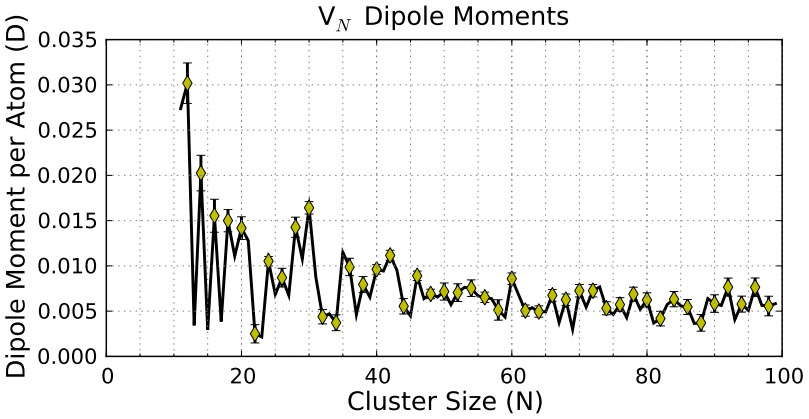

(b) Dipole moments per atom for pure V_N.

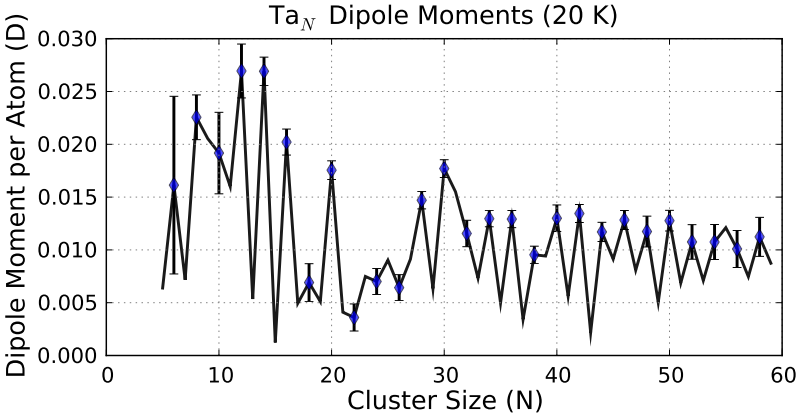

(c) Dipole moments per atom for pure Ta_N.

Figure 4.9: Measurement of the dipole moment per atom for ferroelectric Nb, V, and Ta clusters, at 20 K. The dipole moments are estimated from the maximum deflection. For example profiles observe the case of the pure Nb clusters.

Both spin-lattice and spin-rotation coupling are mediated through the spin orbit interaction [22]. Spin uncoupling therefore suggests that the spin-orbit interaction is weakened. The uncoupling of the spin appears to be closely related to the large electric dipole moments because the temperature dependence of the two phenomena is similar. More convincing is that if the electric deflection field is placed in front of the Stern-Gerlach magnet so that the cluster beam is depleted of the tail with the large electric dipole moment, then the magnetic spin uncoupling also vanishes.

- The observed beam broadening shows a very strong odd-even alternation which is most consistent in the size range N=30-100. The even-N clusters show a stronger response to the electric field than their neighboring odd-N clusters. This odd-even alternation depends on the number of valence electrons. As will be explained later, this is most convincingly demonstrated by a series of deflection experiments on $Nb_N X_M$ clusters where X is any of (O, Au, Al, Co, Fe, Mn)

There was little precedent for the observation of large electric dipole moments in a homonuclear metal particle and several theoretical works attempted to address the dipole moments within the framework of density functional theory [2, 3], their calculations Nb_N ($N < 15$) were able to reproduce the experimental dipole moments for these small sizes, and they explained the apparent disappearance of the dipole moment as an artifact of the rotational motion of the cluster. There is some precedent in the literature [51, 5] for the idea that the chaotic rotational motion of a highly asymmetric top clusters can lead to a reduction of the beam broadening, but this effect appears to require a significant perturbation of the rotational motion such as a slight collision with a carrier gas molecule, so its relevance to our experimental conditions is questionable. Furthermore our electric deflection experiments on Au_9 demonstrate that even a highly asymmetric rotor will still show significant beam broadening.

Laser heating experiments described in [169, 172] performed on Nb clusters further

support the hypothesis that the disappearance of the dipole moment with increasing temperature is not due to the rotational motion. Absorption of a visible photon gives a large increase in the internal energy but only changes the angular momentum of a cluster by $\hbar$. The deflection profile of the laser warmed clusters is very similar to the deflection profiles taken at near room temperature. Or course, a stronger test of this hypothesis would need to increase the angular momentum of the cluster without raising its internal energy.

An additional problem with the calculations in refs. [2, 3] is that they do not address the most striking experimental facts about the Nb clusters, which is the consistent odd-even alternation of the dipole moments from N=30 to N=150. This odd even alternation is most likely an electronic effect, as will be demonstrated by the doping experiments.

4.2.1 Other Studies of Nb Clusters

Niobium is monoisotopic and Nb clusters are easy to produce in a laser vaporization source. As a result, there have been many experiments on Nb clusters investigating a wide variety of physical properties. It is worth reviewing some of these experimental results to see if there is any correlation with the large dipole moments. It should not be surprising that we see little sign of the large dipole moments, because there have been no experiments on Nb clusters at temperatures as low as 20 K.

Nb clusters have been studied by anion photoelectron spectroscopy in refs. [162, 82, 83]. The clusters in these studies were produced with a magnetron source, and the clusters were cooled to 77 K, in a flow tube. The two studies cover different size ranges (up to N=200 in ref. [162]) and are largely in agreement with one another. Large size dependencies were observed for cluster sizes (N < 30), larger sizes showed a smooth behavior. While there is no obvious correlation between the fine features of the photoelectron spectra and the dipole moments observed in our experiments, the dipole moments are highly size dependent for sizes N < 30, while for sizes above N = 30, the dipole moment per atom is relatively flat with a consistent odd-even alternation. There is no odd-even alternation

in the PES data, and the relevance of this is questionable since the electrostatic energy of the dipole moments are smaller than the 50 meV resolution of the photoelectron spectra, and there are additional questions as to whether the final state of the neutralized cluster produced by photodetachment is the same as the ferroelectric state observed in the neutral beam.

At the same time Knickelbein [87] reported an electric deflection experiment on Nb clusters (N < 27) at a temperature of T=68 K. Large enhancements in the polarizability above the bulk value were observed for N = 11-14. Smaller, but still significant enhancements were observed for N=5-7,9,18, and 20. The deflections observed were quadratic and not linear in the deflection field which indicates that the induced polarization is linear in the field, but the enhancements are too large to be explained by the electronic polarizability. It is notable that we observe similarly large dipole moments for these sizes.

The optical absorption spectrum in the visible and near UV was also measured by Knickelbein [90] by tracking the dissociation of rare-gas complexes in a TOF mass spectrum. The optical absorption was found to be smooth and unstructured with a threshold. The ionization potentials of neutral Nb clusters were measured

A similar rare-gas complex dissociation technique was recently applied to measure the far-infrared vibrational spectrum of Nb clusters [53], V[52, 128], and Ta [61]. These clusters are produced at a source temperature of 77 - 100 K. Comparison of the measured FIR spectra with the theoretical spectra calculated from DFT calculations allows for the deduction of the cluster structures. Unfortunately there hasn't been a thorough comparison between the structures identified in [53] and the structures calculated in refs. [3].

4.2.2 Nb Alloy Clusters: Effect of Doping on Ferroelectricity

The dipole moment and the odd-even alternation is an electronic effect. The clusters which show enhanced dipole moments are those that have an even number of electrons, not those that have an even number niobium atoms. This line of evidence points away from theorists

that seek to explain the origin of the dipole moments in the cluster structure. A series of experiment adding single impurity atoms to Nb clusters conclusively demonstrates the electron nature of the dipoles. This work is due to Yin [172]. The VAu and TaAu alloys have not been shown anywhere before.

To illustrate the trend: V,Nb, and Ta doped with Au which has an odd number of valence electrons. Thus Nb_N with 1 Au atom added should have its odd even alternations inverted so that they Nb clusters with an odd number of Nb atoms have larger dipole moments than those with an even number of Nb atoms. Adding another gold restores the original odd-even alternation pattern. The effect holds for (O, F, Al, Co, Fe). Another interesting dopant in Mn which appears strongly reduces the dipole moments. These results are particularly interesting because the follow the behavior of superconducting Nb alloys so closely. NbAu alloy has a much larger T_C than pure Nb and Mn is a magnetic impurity which breaks the time-reversal symmetry required for the formation of cooper pairs. These results are certainly suggestive that the dipole moment is related to superconductivity[172].

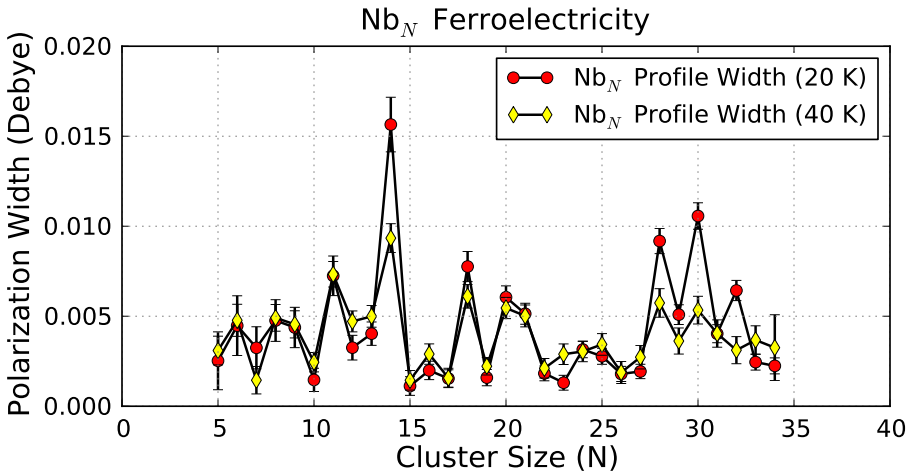

Figure 4.10: Figure showing the strong reduction of the Nb beam broadening as the source temperature is raised from 20 to 40 K. The reduction is even stronger as the temperature is raised further to 100 K. Because the profiles for Nb clusters are strongly asymmetric we use the overall width of the polarization distribution as a measure of the transition.

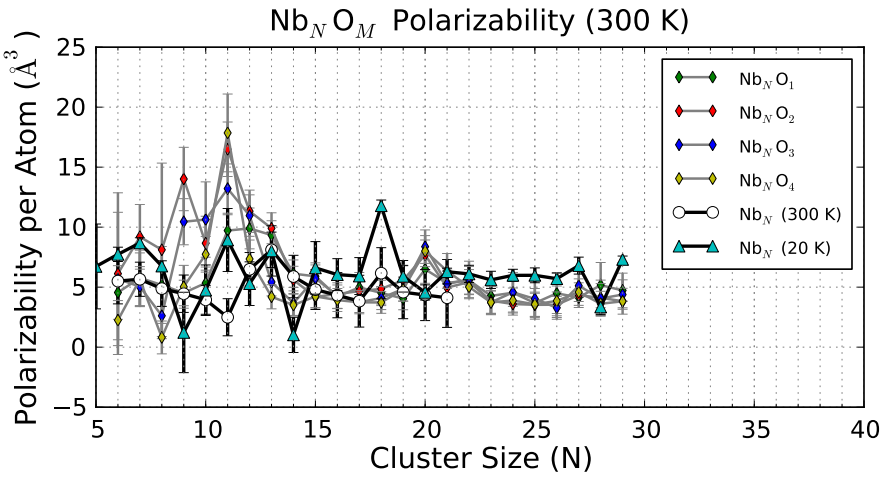

(a) Polarizability per Atom for Nb_NO_M clusters at room temperature

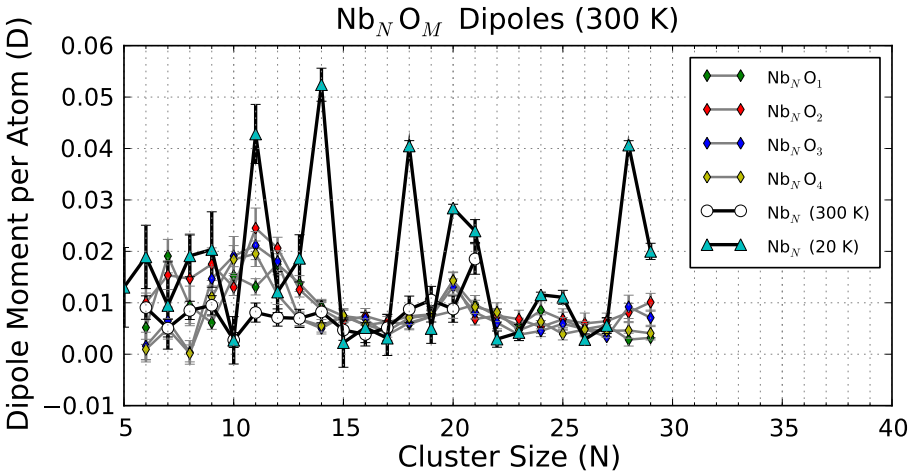

(b) Dipole Moment per Atom for Nb_NO_M clusters at room temperature

Figure 4.11: Results of electric deflection experiment on Nb_N clusters at room temperature. To compensate for the larger velocity the beam was carried in argon instead of helium. This reduced the velocity from 1100 m/s to 420 m/s. The beam also contained significant numbers of oxide clusters. And many of these clusters also have significant dipole moments at 300 K.

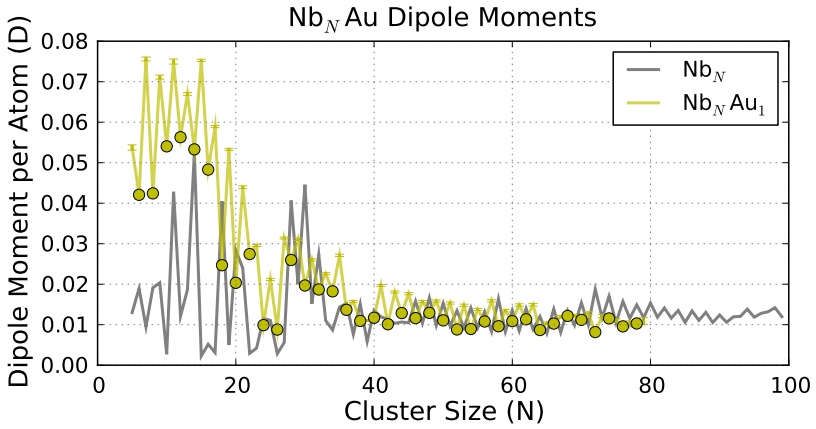

(a) Dipole moments per atom for $Nb_NAu_{0,1}$. Note that the addition of a single Au atom inverts the odd-even alternation of the dipole moment.

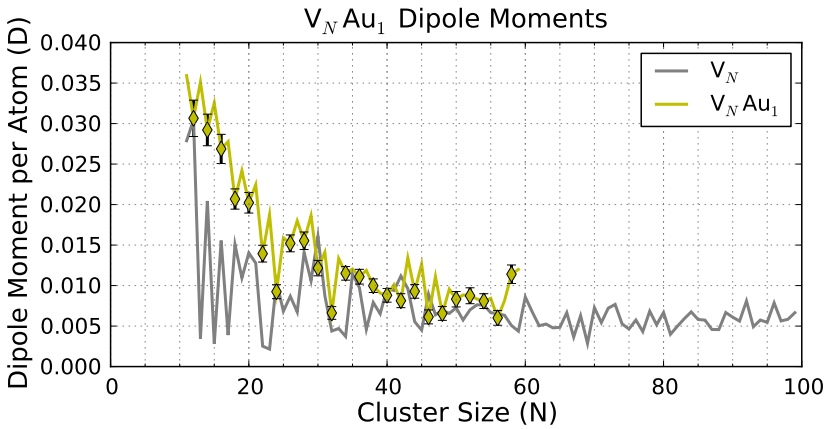

(b) Dipole moments per atom for V_NAu_1.

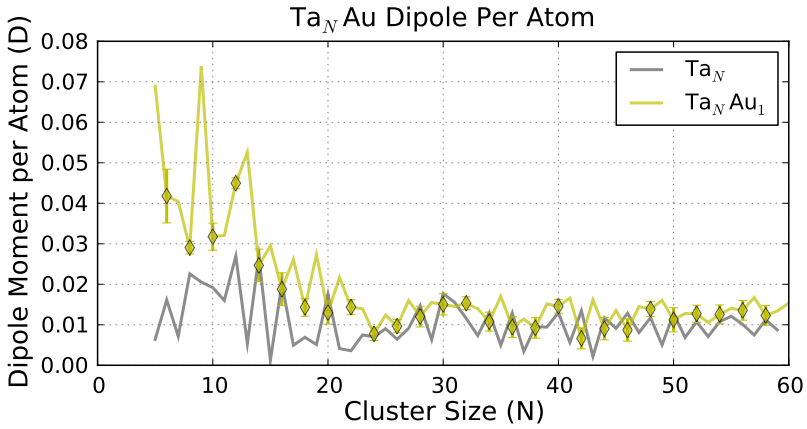

(c) Dipole moments per atom for Ta_NAu_1.

Figure 4.12: The effect of doping Nb, V, and Ta clusters with a single Au atom. For all clusters addition of a single gold atom enhances the magnitude of the dipole moments and it inverts the odd-even effect. The same pattern has been demonstrated for many other impurity elements (O, F, Al, Co, Fe, and Ho) in ref. [172]

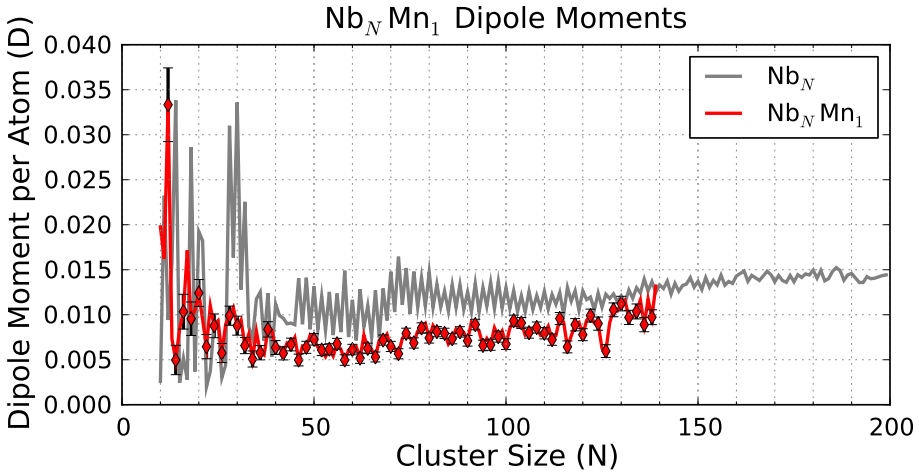

Figure 4.13: Dipole moments per atom for $Nb_N Mn_{0,1}$. Unlike the other impurities,the addition of a single manganese atom causes a large reduction in the dipole moment

4.3 Aluminum

Aluminum is a trivalent metal with 2 s valence electrons and 1 p valence electron. This makes it an intermediate case between the alkali metals where the valence electrons are derived from s orbitals, and transition metals where the valence electrons are derived from partially localized d orbitals. In the bulk, its Fermi surface is far from the nearly spherical shape of the Alkali and Noble metals (k_F lies in the 3rd Brillouin zone) [6].

There have also also been many studies on Al clusters since they are easy to produce with laser vaporization source. Many of these studies found evidence of shell structure, although it is nowhere near as clear as in alkali clusters. The polarizabilities of Al clusters were measured in an early experiment by de Heer [41], which found major discrepancies with the jellium predictions for cluster sizes less than $N = 60$, the ionization potentials were reported in refs. [140, 121].

Al clusters have also been studied in a series of anion photoelectron spectroscopy experiments [58, 38, 33, 104]. Which were also focused on the observation of electronic shell structure. The most current measurement suggests that electron shell closings occur for the sizes

There were several theoretical works which addressed these experimental findings. [1, 79, 107, 171, 127]

Our measurement of the polarizability of Al clusters is shown in Figure 4.3 (a). A comparison with the earlier measurement of Milani and de Heer [41] is also shown. Our measurement covers a much larger size range, and reveals significant structure in the polarizability trend for cluster sizes larger than $N = 60$. In ref. [41] it was noted that the polarizabilities converged to the jellium prediction at $N = 60$. Our experiment covers a much larger size range and our measurements show that the convergence to the bulk (or the jellium prediction) is far from complete at $N = 60$. It appears that $N = 60$ is only a local maximum in a series of oscillations. In fact, the oscillations are highly reminiscent of those observed in the Na cluster polarizabilities, although it is doubtful whether the explanation

given for them in section 4.1.3 applies to Al.

The Al_N polarizability shows local minima at $N = 34, 40, 44, 52, 66, 82$ and local maxima at $N = 31, 37, 42, 46, 56, 75$. The photoelectron study notes that shell closings occur for neutral Al clusters with sizes $N = 46, 52, 56, 66, 78, 80, 100$, and 106. Several of these coincide with the local extrema of the polarizability curve.

It is also notable that the fine structure in the polarizability trend differs considerably from that reported in refs. [107, 41]. (see Figure 4.3). The amplitude of the variations in our measurement are much smaller and the local maxima and minima do not agree. A major difference between these two measurements is that the experiment in ref. [41] was performed on clusters produced in a source at 300 K, while our experiment was done at 20 K. It is unclear exactly why a change in temperature from 300 K to 20 K would cause the polarizability curve to change in this way. The fine structure in the polarizability and dipole curves have been repeatedly observed in several different experiments at different fields and temperatures from 20 - 40 K. The features are consistent from run to run, and the data points plotted in Figure 4.3 is an average over these runs.

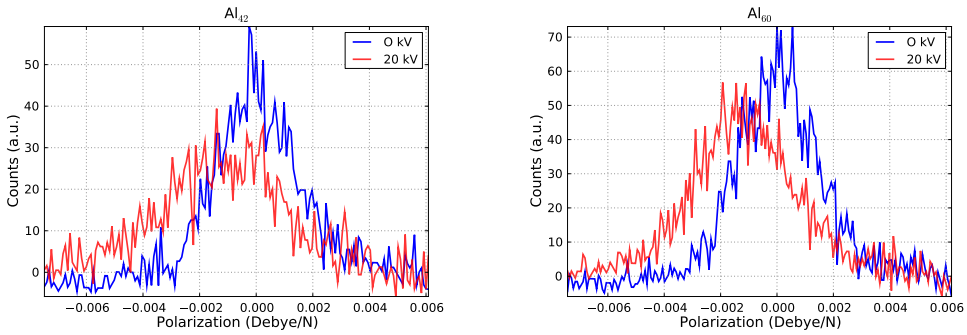

Figure 4.14: Electric Deflection Profiles for Pure Al_N Clusters, recorded at a temperature of 20 K. These are to illustrate the visible shape of the deflection profile associated with the dipole moments plotted in the next figure.

An analysis of the beam broadening reveals that all Al_N clusters have small electric dipole moments on the order of 0.002 - 0.004 D / atom. There are again, significant variations with cluster size that appear to be only loosely correlated with the trends observed in

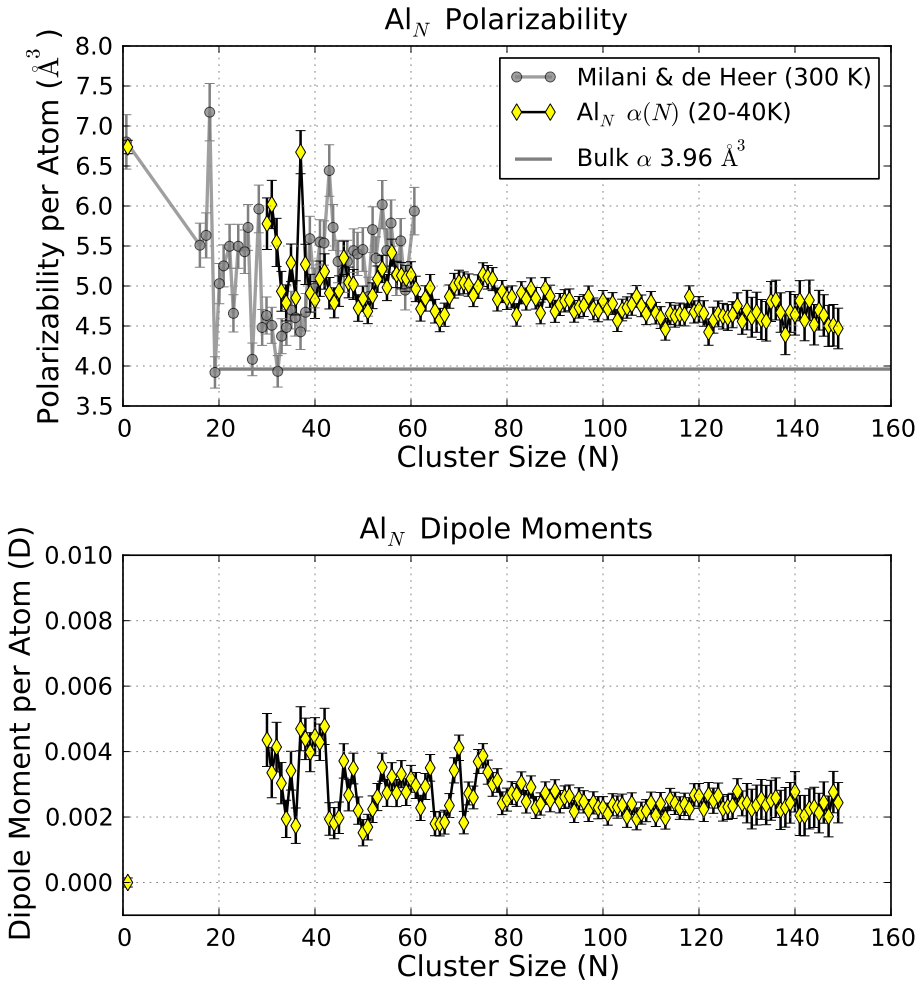

Figure 4.15: Polarizability and Dipole moments for Al_N. The polarizability is plotted with the previous best measurement of available [41, 110]. There are large discrepancies with these measurements.

the polarizability. For example, N = 37 shows a large maximum in the polarizability, and it is also at the center of a local maximum in the beam broadening, however N=36, and N=38 show broadening of similar magnitude, but their measured polarizabilities are much lower than N=37.

Just as for the polarizability the per atom dipole moments have been observed to have the same value for several different deflection fields and temperatures between 20 - 40 K.

4.4 Transition Metals: Iron, Cobalt, Manganese

Iron and cobalt clusters have been extensively studied as itinerant ferromagnets, and bulk manganese becomes anti-ferromagnetic at 90 K. Like the bulk materials, Fe and Co clusters are ferromagnetic down to the dimer [13, 12, 81]. For Co_N and Fe_N, the magnetic moments per atom are enhanced compared to the bulk values of 1.7 μ_B for Co and 2.2 μ_B for Fe. Mn_N shows a

Itinerant ferromagnetism, or the spontaneous spin polarization of delocalized electronic bands, can be understood as a trade off between the exchange energy gained by spin polarization and the extra kinetic energy needed to overfill one spin band. The cost in kinetic energy to overfill one spin band is proportional to the density of states at the Fermi level $g(E_F)$, and the exchange energy gained is typically described by an exchange constant I which is the strength of the exchange interaction between the spin up and spin down bands. When $g(E_F)I > 1$ it is predicted that the system will become ferromagnetic. While this model (due to Stoner) is a vast oversimplification and many of its predictions are incorrect, we can intuitively reason that any change to a system that localizes the electronic wavefunctions and thus increases $g(E_F)$ will strengthen the tendency toward ferromagnetism.

It is widely agreed [152, 119, 118, 65, 80] that the magnetic moments of small cobalt clusters are enhanced because the *d* electrons are more tightly bound or localized than they are in the bulk metal. The increased localization is a consequence of the reduced nearest neighbor coordination in a cluster. An anion photoelectron study [100] remarkably found large well-resolved peaks in the density of states for cluster sizes up to N = 50.

The polarizabilities of both Co_N, and Fe_N are unremarkable with the exception of the large polarizability enhancement for Co_{42-46}. A similar block of clusters with enhanced polarizability occurs weakly for Fe clusters at Fe_{38-39}. A similar block was also observed by Knickelbein [84] observed in a measurement of the polarizability of Ni clusters for Ni_{48-52}.

An analysis of the beam broadening gives an estimate for the dipole moments of around

0.002 D / atom for most of the clusters $N < 100$. For dipole moments this small the beam broadening is not qualitatively visible in the deflection profile as it is for Nb, Al, Rh, Bi and the rare-earths. There are exceptions such as Co_{15}, Fe_{12} and Fe_{26} which show a qualitatively visible broadening, and we feel confident in the conclusion that these cluster sizes have permanent dipoles.

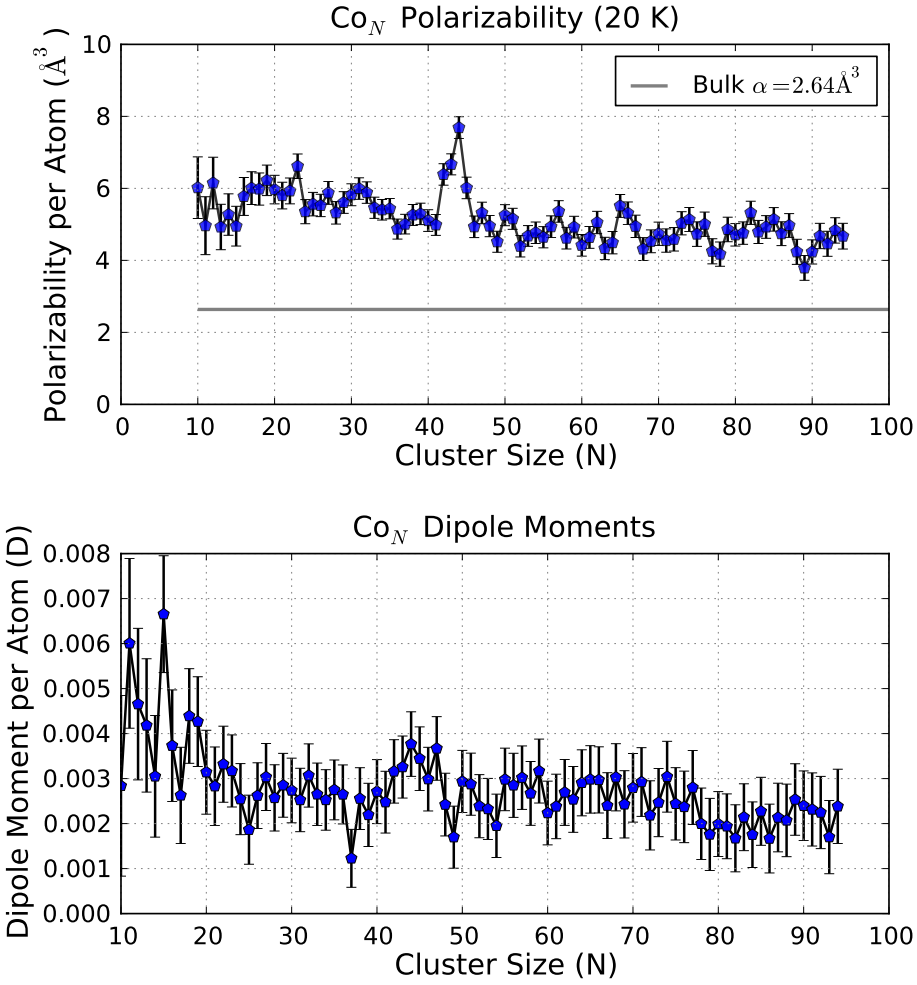

Figure 4.16: Polarizability and Dipole moments for Co_N. The polarizability shows a jump around $N = 40$, a feature that has also been observed in Ni_N clusters by [85]

For the case of manganese, we see a large 50% increase in the polarizability starting at N=60. From N=20-60 the polarizability per atom is around around 8 Å^3 and from N=65-100 the polarizability per atom clusters around 13 Å^3.

Measurements of the magnetic moments [86, 89, 16] show no obvious correlated change

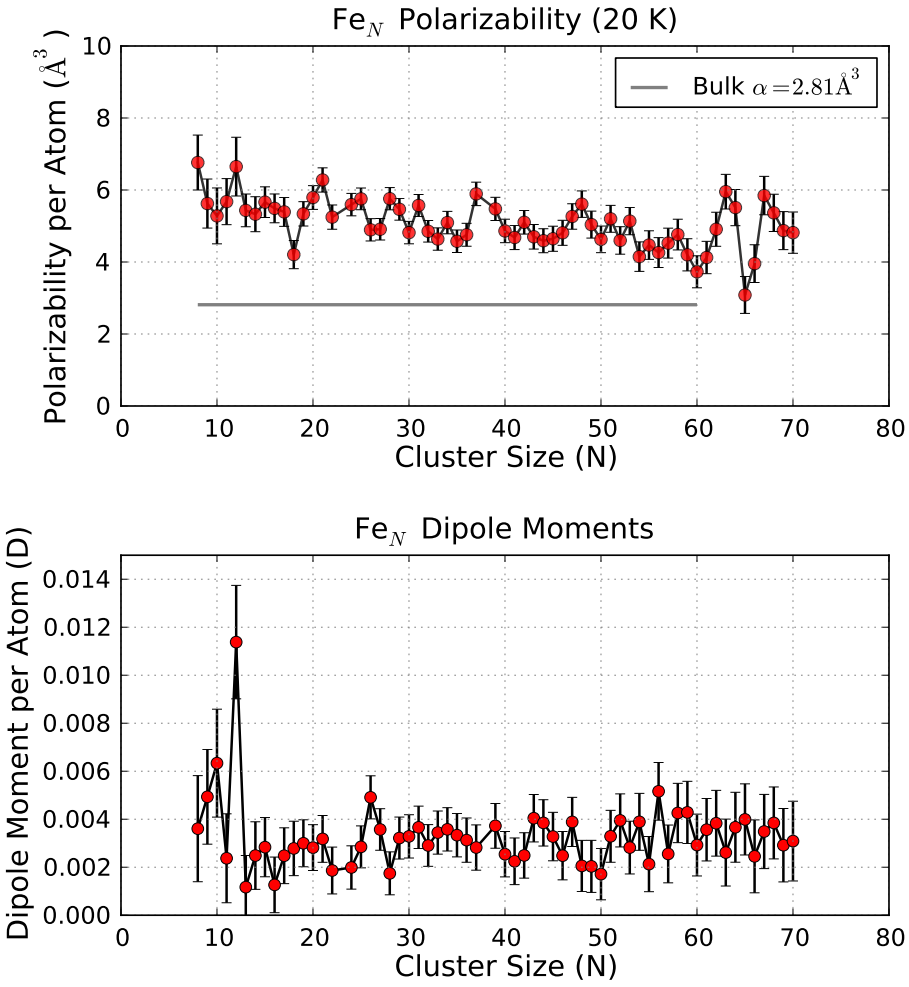

Figure 4.17: Polarizability and Dipole moments for Fe_N. The polarizability shows a jump around there is a faint remnant of the jump in polarizability around $N = 40$ which was also observed for Co and Ni clusters. Also notable is the very obvious dipolar broadening for Fe_{12}.

in the magnetic properties at N = 60. The polarizability per atom for a metal sphere is proportional to its volume, thus it is possible that this increase in polarizability reflects a structural transition. In this interpretation, the clusters with $N < 60$ prefer a structural arrangement that is more compact than those with $N > 60$. Could a transition between a close packed and non-close packed geometry such has fcc to bcc transition account for this change of volume? To account for the full magnitude of this change would require a change in volume of around 50%!

The beam broadening gives a dipole moment per atom for about 0.005 D. This is too

small to account for the magnitude of the observed polarizability enhancement. Because there is a large amount of oxygen contamination present in the beam, and the Mn_NO mass peaks are well resolved and isolated from the pure Mn_N peaks, we can examine the effect of oxygen doping on the transition (Figure 4.4) We see that for the smallest cluster sizes, adding a single oxygen atom gives a slight increase in both the dipole moment and the effective polarizability. The differences between pure Mn_N and Mn_NO_1 rapidly disappear with increasing cluster size. The sudden increase in the polarizability at N = 60, occurs for both Mn_{60} as well $Mn_{60}O_1$.

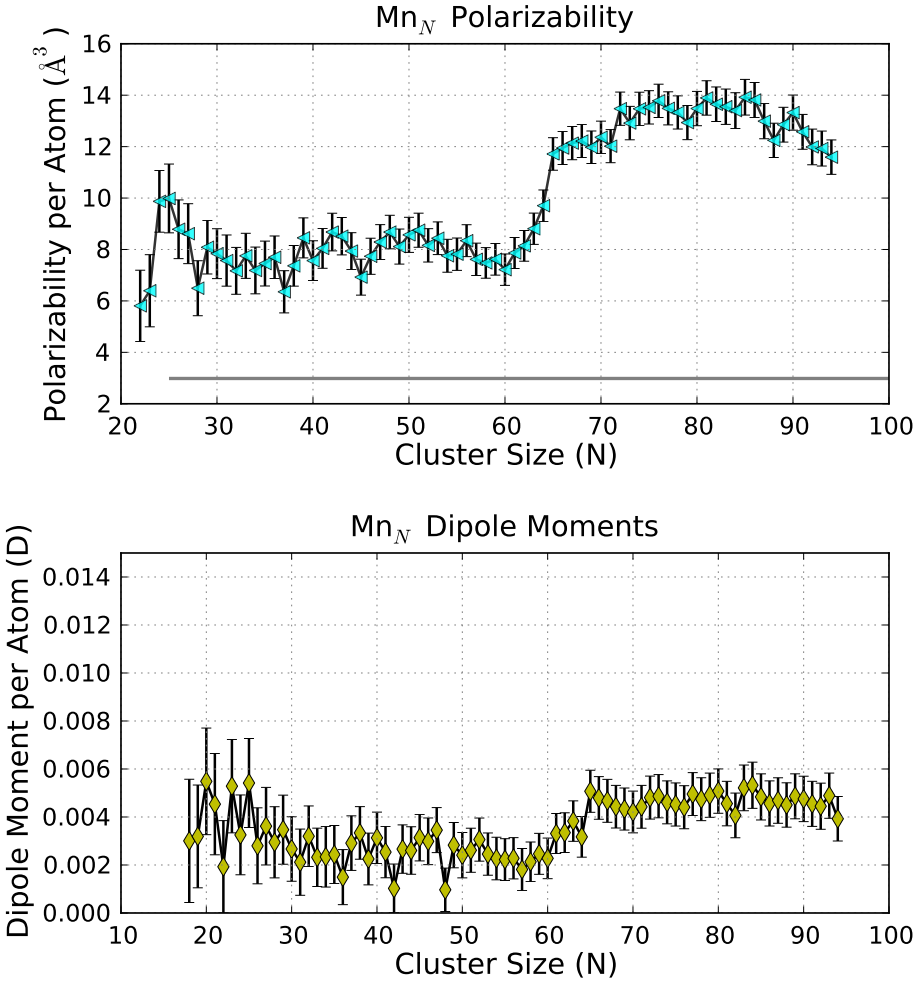

Figure 4.18: Polarizability and Dipole moments for Mn_N.

To conclude this section we present a comparison of the polarizabilities of iron, cobalt,

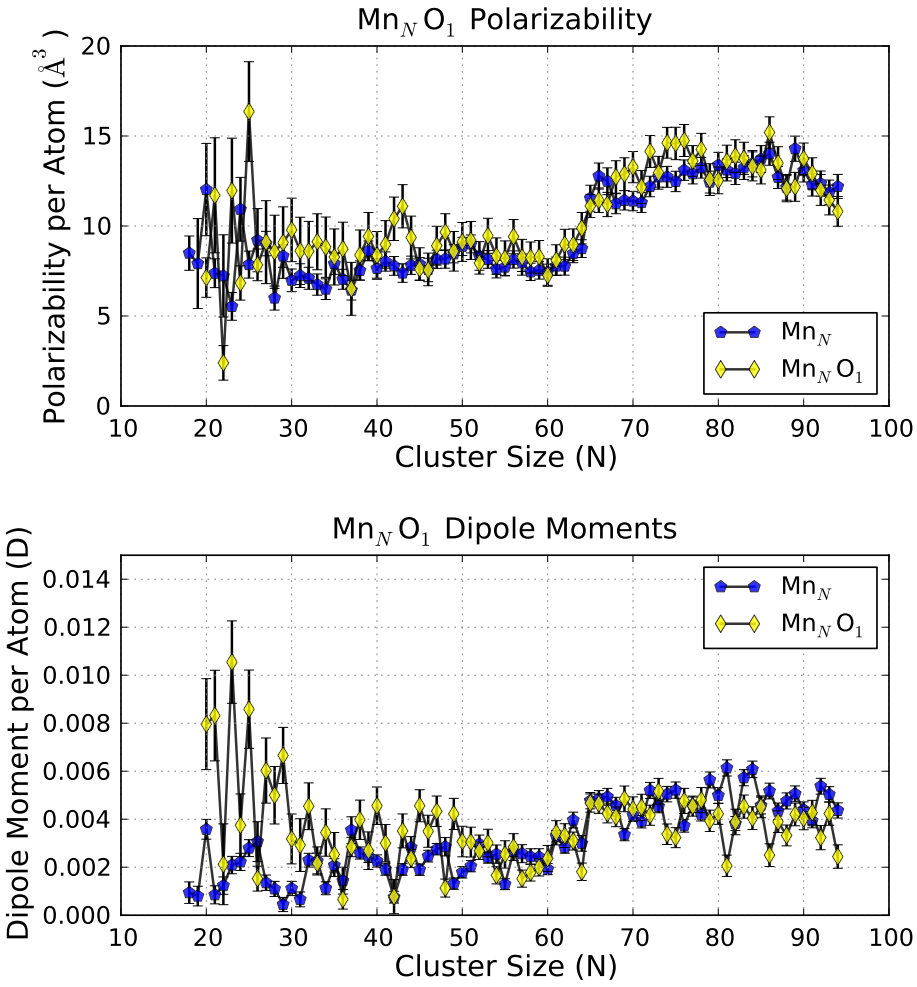

Figure 4.19: Polarizability and Dipole moments per atom for Mn_NO clusters, compared with pure Mn_N clusters. The addition of a single oxygen atom gives an enhancement of the dipole moment for small sizes. However the jump in the polarizability at $N = 60$ is preserved.

and nickel clusters using data from an electric deflection experiment of Knickelbein [85].

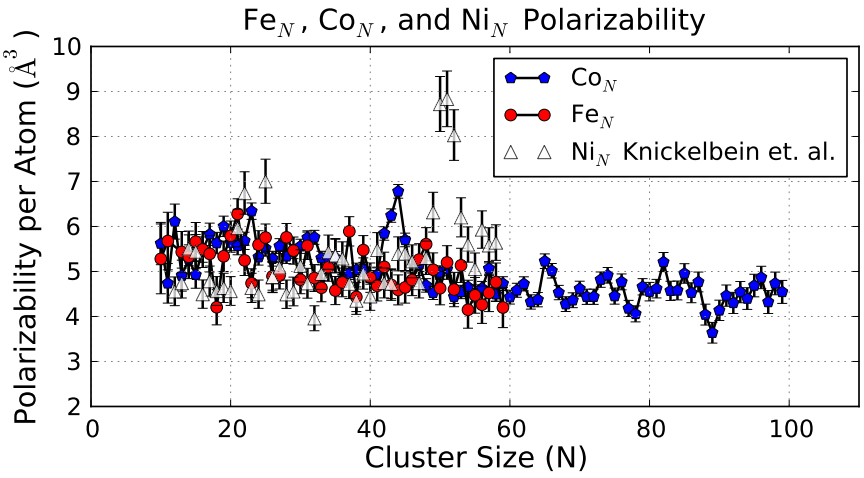

Figure 4.20: Polarizabilities of Fe_N, Co_N, and Ni_N plotted on the same graph. The most notable feature is their similarity. The jump in the polarizability from Co_{40} to Co_{46} has a very similar appearance to the peak observed in Ni_{47} to Ni_{53}.

4.5 Rhodium: Simultaneous Electric and Magnetic Moments

Rh_N clusters attracted widespread interest because they are ferromagnetic while the bulk metal is non-magnetic. Our experiments show that nearly all Rh_N clusters have permanent electric dipole moments. This is also in contrast with the bulk material which is a metal and has an internal electric field of zero, and thus supports no permanent dipole moment. This system is highly unusual as many of the Rh_N clusters show both electric and magnetic polarizations. For sizes up to N=100 we still observe small electric and magnetic dipole moments. The correlation between the two properties does not appear to be strong, and they could in fact be entirely independent of one another. There is no obvious correlation between the two properties so the cluster sizes which show exceptionally large electric dipole moments are not necessarily those which have large magnetic moments.

We will take a brief diversion away from electric deflection experiments to explain our magnetic deflection experiments on Rh_N as this is an important aspect of this cluster system.

4.5.1 Magnetism of Rh clusters

The magnetism of Rh clusters was first studied experimentally by Cox et. al. [36, 37] who performed a Stern-Gerlach deflection experiment on a beam of Rh clusters produced in a laser vaporization source at 60 - 100K. Like Fe, Co, and Ni, Rh clusters were found to be ferromagnetic, confirming earlier theoretical predictions due to Reddy et. al. [130]. This study was inspired by the observation of magnetic moments at the Rh surfaces, which suggested that the increased density of states due to the reduced coordination at the metal surface would be sufficient to favor a spontaneous spin polarization. The non-magnetism of bulk Rh metal can be intuitively understood as a consequence of its low density of states at the Fermi level which does not fulfill the Stoner criteria for spontaneous magnetization.

We have performed Stern-Gerlach deflection measurements on a beam of Rh clusters very similar to those described in refs. [36, 37]. Our beam temperature is 20 - 40 K, which

is about 2-3 times lower than the sources used in previous studies. Our measurements of the magnetic moments are in nearly perfect agreement with the revised values quoted in ref. [36]. (see Figure 4.5.1)

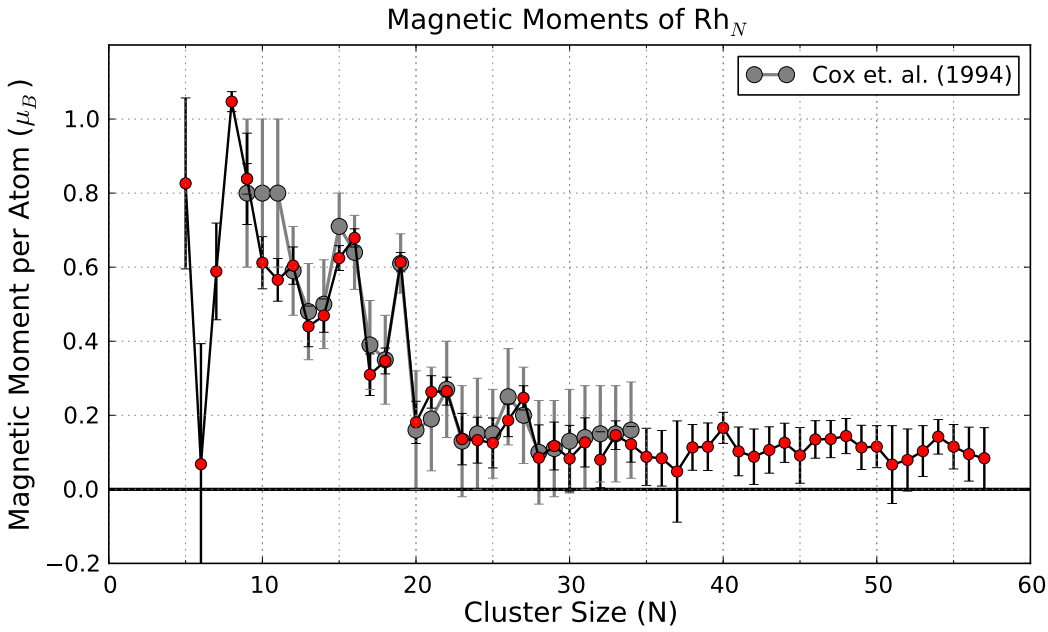

Figure 4.21: Magnetic moments per atom for Rh_N clusters at a temperature of 34 K. The intrinsic moments are calculated by applying the Langevin susceptibility to the average deflection of the profiles. The agreement with the earlier measurements reported in [36] is almost perfect. Nearly all of the points lie in the error bars of ref. [36] and many data points lie in the center of the error bars from the previous measurement.

There are some critical differences between our interpretation of the Stern-Gerlach deflection experiment and the interpretation given in refs.[37, 36]. Cox. et. al. claim that the single sided deflection profiles and the field and temperature dependence of the cluster magnetization is a consequence of superparamagnetic relaxation. The superparamagnetic model assumes that the giant spin in a magnetic field is rapidly exchanging energy and angular momentum with a heat bath at temperature T. This model will indeed give the correct Langevin-Debye susceptibility for the average magnetization, but the assumptions that this model depends on do not apply to a free cluster in a molecular beam. The essence of the problem is that there is no heat bath for thermal relaxation to take place once a cluster has

left the source. It was proposed that the excited vibrations of the cluster could function as a heat bath, but the Debye temperature for rhodium is 480 K so at 20 K the vast majority of clusters in the beam are in the vibrational ground state[167, 168].

Another difficulty with the superparamagnetic model is that it cannot account for the shapes of the observed deflection profiles. If the superparamagnetic model were correct, then every cluster in the beam would quickly lose memory of its initial conditions when it enters the deflection field, and the deflection in the magnet would reflect thermal equilibrium with the heat bath it is assumed to be interacting with. Thus, every cluster should experience the same deflection, and there should be no broadening of the beam. This is very different from what is actually observed in the experiment. Refer again to Figure 4.5.1. The profile shown there which is consistent with the predictions of the superparamagnetic model is Rh_{18}, which shows a single sided deflection and little or no broadening. Rh_7,Rh_{17}, and Rh_{21} actually clearly show double sided deflections, Rh_{15} Rh_{16} and Rh_{19} show a single sided weakly broadened peak on top of a long asymmetric tail. When we computed the magnetic moments in Figure 4.5.1 we were careful to included both sides of the deflection profile the full tail in the computation of the average magnetization used in the Langevin susceptibility below.

$$\bar{M} = \mu\left(\coth\left(\frac{\mu B}{kT}\right) - \frac{kT}{\mu B}\right) \tag{4.5}$$

The most likely explanation for varying shapes of the deflection profiles observed in Figure4.5.1 is differences in the magnetic anisotropy forces which bind the cluster's magnetic moment to a particular direction in the cluster's body-fixed coordinate system. For anisotropy which is much stronger than the applied deflection field, or the rotational energy, the magnetic moment will be rigidly fixed in the cluster body and a "locked-moment" model similar to that discussed for electric dipoles will apply. This type of model can nicely account for the profiles where two sided deflections are observed, but cannot correctly reproduce the deflection profiles which are single sided, except for much stronger fields or

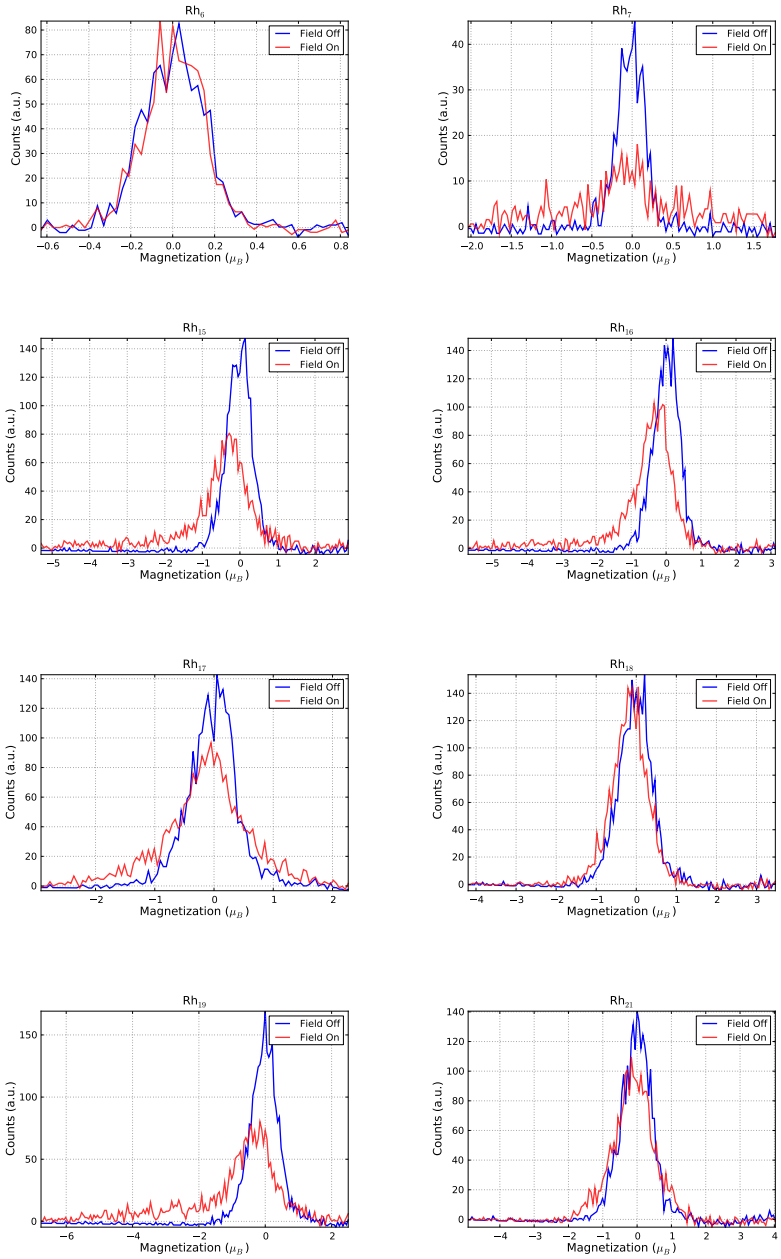

Figure 4.22: Magnetic deflection profiles of Rh_N clusters at a temperature of 34 K, and B = 0.95 T. Several selected sizes are shown to illustrate the variation in the deflection profiles which appear. N=6 shows no deflection, N=7,17, and 21 show strong two-sided deflections, N=15,16,19 show single sided, but highly asymmetric profiles with a long tail. N=18 shows a single sided deflection with little broadening

lower temperatures that could possibly apply.

The adiabatic magnetization model discussed in ref. [168], gives deflection profiles

with single sided deflections and significant broadening, but we haven't actually tested it to see if it can correctly reproduce the observed deflection profiles. This model assumes that the moment is due to a macro spin and that S_z is a good quantum number, and all other interactions, such as spin-orbit, spin-rotation, and anisotropy are treated as weak perturbations which cause level crossings to be avoided. The physical parameters of cluster only enter the model through the density of states. The avoided crossing model takes a delightfully agnostic point of view on whether the quantum states at zero field line of the Zeeman diagram are rotational, vibrational, or electronic states.

The only remaining mystery is Rh_{18} - it shows a single sided deflection with little broadening - which is exactly what would be predicted if superparamagnetic relaxation were taking place. Since the assumptions required for superparamagnetic relaxation are so implausible, there should be an adiabatic explanation for this narrow distribution. One possibility is that Rh_{18} is a highly asymmetric rotor with a rigidly locked magnetic moment that is tumbling chaotically in the deflection field. There have been a few early theoretical and experimental [48, 5, 5, 51] works which suggest that fully developed chaotic motion can have effects which are very similar to thermal relaxation.

4.5.2 Electric Properties, permanent dipole Moments

Now we return to the discussion of electric deflections of Rh clusters.

Rh_N clusters have been studied by electric deflection methods before, by Bayer and Knickelbein. The only reported quantitative values for the polarizabilities, although they did note that the temperature dependence of the polarizability suggested the presence of dipole moments. Our measurements for the Rh_N polarizability are in excellent agreement with their 42 K measurements, measurements cover a much larger range of cluster sizes. We also observe a significant amount of beam broadening, which allows us to derive estimates for the dipole moments. The dipole moments per atom are shown in Figure 4.5.2,

the deflection profiles for select sizes are shown as insets to illustrate the qualitative difference between in deflection profile that the oscillations correspond to. The fine structure in the measurements are reproducible from run to run, and unlike Nb,V, and Ta we find no evidence that the dipole moments of Rh_N are sensitive to temperatures up to 50 K.

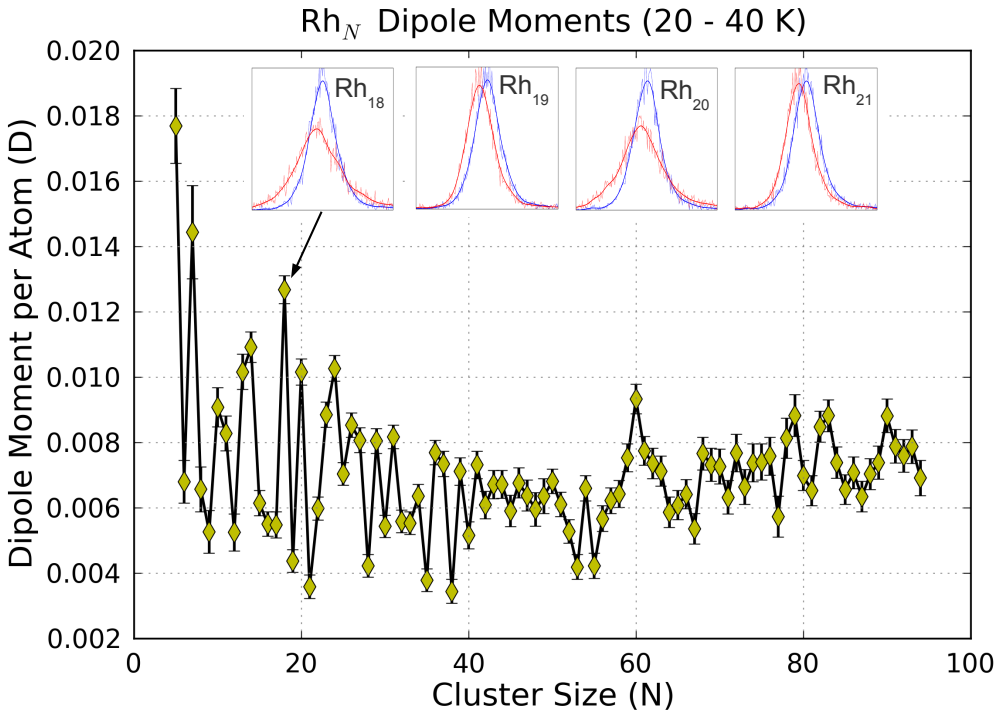

Figure 4.23: Electric dipole moments per atom for Rh_N clusters averaged at several temperatures. The dipole moments are insensitive to temperature in the range T = 10 - 50 K. Insets show deflection profiles of selected clusters to illustrate the qualitative shapes of the deflection profiles.

4.5.3 Connections between the dipole moment and the chemical reactivity?

Much recent work on Rh_N has been motivated by potential applications in catalysis. There have been many attempts to relate the physical properties of clusters measured in beam experiments such as the polarizabilities, ionization potentials, electron affinities, binding energies, etc. with their chemical reactivity in different reactions. The most successful

of these has been the relationship between the electron affinity (EA) and the reactivity as discussed by Knickelbein [84]. Without going into too great of depth on the topic we give one example of where the per atom dipole moments of neutral Rh clusters seem to correlate reasonably well with the rate constants for a reaction between charged Rh clusters and N_2O.

The rate constants for this reaction have been measured by in a gas-phase experiment due to MacKenzie et. al. [70]. The principle of an FT-ICR (Fourier Transform Ion-Cyclotron Resonance) experiment is easy to explain. Charged clusters are produced in a laser-vaporization source, and directed into the bore of large superconducting magnet. The large magnetic field causes the charged clusters to orbit in cyclotron orbits. The frequency of the cyclotron orbit depends on the charge to mass ratio as $\omega_c = \frac{Bq}{m}$, and the orbiting charged particles will induce a periodic voltage in metal electrodes which are arranged concentrically around the chamber where the clusters orbit. Thus the abundance of any charged species in an FT-ICR is directly related to the amplitude of the frequency component of a cyclotron orbit with that mass.

To measure the reaction rates between cluster ions and a gaseous molecule a small pressure of the reactant is admitted to the chamber and the depletion of the cluster-reactant compound is monitored in time. The experiment found that the rate constant for the reaction with N_2O varies over several orders of magnitude as a function of cluster size. The log rate constants are plotted against the measured dipole moments in Figure 4.5.3

The theoretical estimates for the rate constants used in ref.[70] are calculated with the surface charge capture (SCC) model due to Kummerlöwe and Beyer [95]. It is interesting to note that this model is essentially a metal sphere model which assumes that all of the excess charge of a charged cluster is distributed on the surface, just as for a classical metal sphere [77]. Because of the measured electric dipole moments of the neutral, it is very likely that this model gives an inaccurate description of the charge density on the surface of a Rh cluster cation/anion.

It is noteworthy that this model gives much more accurate agreement for many other

reactions with Rh clusters, such as CO, NO, benzene, etc. For these reactions there is apparently little or no correlation between the measured dipole moments and the chemical reactivity.

Even for N_2O the correlation is far from perfect. There doesn't appear to be any clear quantitative relationship between the measured per atom dipole moments and the N_2O rate constants. The agreement is best in that the dipoles and rate constants share many local maxima and minima. This suggests that the N_2O reaction is probing some aspect of the Rh clusters electronic structure that is being missed by reactions with CO, NO, etc.

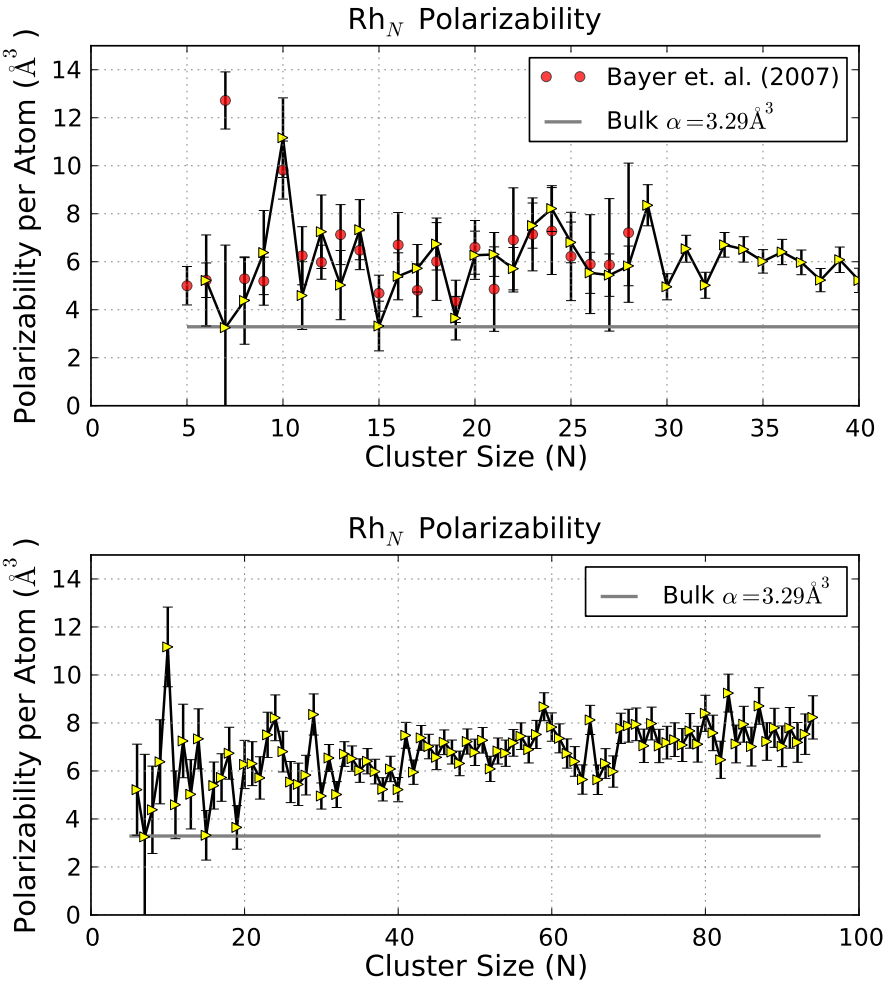

Figure 4.24: Polarizability of Rh_N Clusters. Our measurements agree well with the work of Bayer and Knickelbein [11]. Their work was taken at a temperature of 49 K, and our data is taken at 20 K. From N = 20-95 there is a slight increasing trend in polarizability with cluster size. This increase in *effective* polarizability with cluster size is consistent with a constant dipole moment per atom, which is what is observed from the beam broadening.

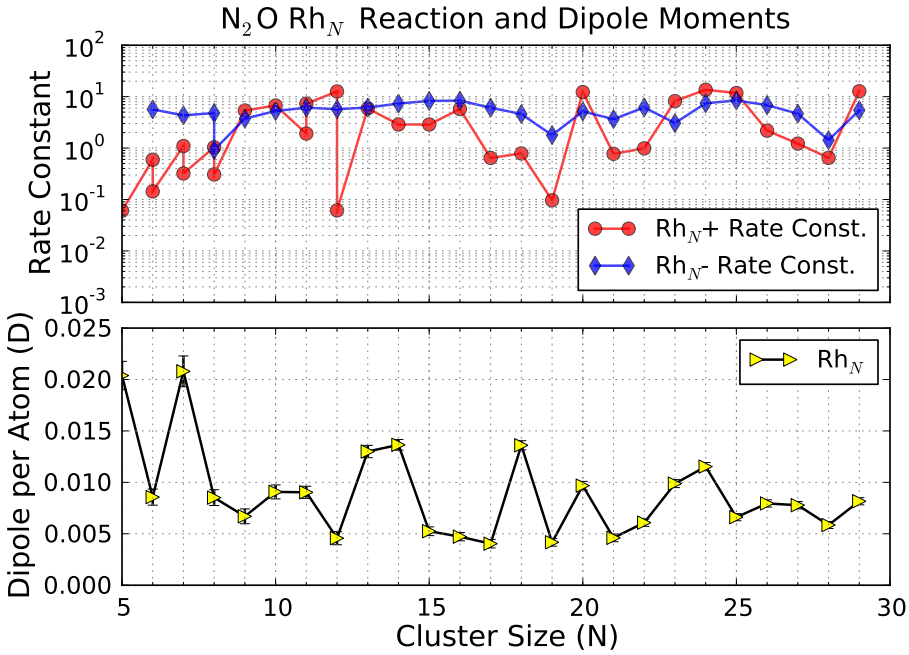

Figure 4.25: Correlation of the N_2O reactivity and the per atom dipole moments. Rate constants for gas phase reactivity between Rh_N cations and anions and N_2O. These data are from an experiment by Harding et. al. [70]. The correlation is far from perfect but it is notable that the two curves have minima at corresponding sizes.

4.6 Gold

The ionization potentials of neutral Au clusters are larger than the 6.45 eV photon energy of the ArF excimer laser. Thus we only have conclusive measurements for Au_9 and Au_{11}. The mass spectrum for the Au clusters that we record with a photon energy of 6.45 eV is shown in Figure 4.26. This prevents us from making any conclusions about the size dependence of the polarizabilities and dipole moments, but these two clusters are still worth discussing. There is a large literature on the chemistry Au clusters [125] and there have been many experimental and theoretical efforts to determine their structures. These studies suggest that Au_9 is a highly asymmetric rotor. Thus a deflection experiment on Au_9 provides a useful test case to investigate the deflection dynamics of an cluster that is known to have an asymmetric structure.

Our molecular beam electric deflection experiments reveal that the neutral Au_9 cluster shows a symmetric two-sided deflection profile,(Figure **??**) which is the signature of a permanent electric dipole moment. If we apply the same spherical top model to relate the observed beam broadening to the dipole moment we estimate that it Au_9 has an electric dipole moment of around 0.285 ± 0.048 D. The neutral Au_{11} cluster shows no visible beam broadening so we conclude that it's dipole moment is zero within experimental error.

The far-infrared vibrational spectra of these clusters, in the range 50 - 250 cm^{-1}, allows the cluster structures to be assigned. As previously predicted, Au_9 is a planar double-capped hexagon with $C2v$ symmetry. The FIR spectrum and the dipole measurement strongly support a $D3h$ structure for Au_{11} which has a three-fold axis normal to a mirror plane.

Calculation of the electric dipole moments using methods of quantum chemistry in a system with delocalized electrons such as a metal cluster is a delicate matter. The electrostatic energy of a 1 Debye dipole moment is on the order of a few meV, and other sources of error such as the choice of grid size for integration of the charge density can lead to erroneous results. While there are many covalently bonded systems with dipole moments

known to great precision, there are few examples of homonuclear cluster systems which can be used to test these methods. Two different calculations using density function theory (one using the LDA, and the other using a gradient dependent functional, both estimate dipole moments on the order of 0.28 D - 0.32 D. These dipole moments are very close the the experimentally measured value, which suggests that in this case at least DFT is accurately reproducing the dipole moments.

Small gold clusters [63] are of technical interest for their application as catalysts [174] (e.g. oxidation of CO), and low-toxicity fluorophores [176] for biological imaging. For catalysis, Recent work has emphasized the critical role of the support for catalysis on MgO surfaces [175, 174, 173]. and IR spectroscopy has identified the effect of activation by measuring shifts in the stretching frequency of molecules adsorbed on transition metal clusters. [103].

Among small Au clusters Au_9 and Au_{11} have the lowest ionization potentials (which is why we are able to observe them). Following [84] suggests that they should be active chemically [84].

The geometry of Na clusters with a lone *s* valence electron, is determined by the degeneracy of the electronic shells. For Au the *d* band overlaps in energy with the *s* band, causing the interatomic bonds to become highly directional. Thus the geometric structure is expected to be much more significant. This directional bonding causes the small Au clusters to prefer geometries quite different from the from spheroids or close-packed icosahedral structures. Many small Au clusters have a planar structures [166] and some larger ones have been shown to arrange in hollow cages [28]. From a theoretical perspective, these structures emphasize the importance of properly accounting for the relativistic corrections to the electronic energy. [68, 69]

The deflection profiles are shown in Figure 4.27 The qualitative difference between Au_9 and Au_{11} is very clear. Au_9 is broadened symmetrically about the center of the beam, where Au_{11} is not broadened at all, only slightly shifted. Two scales are plotted: (1) where the

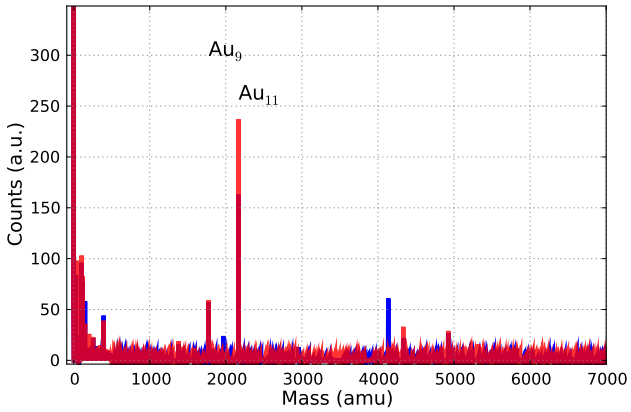

Figure 4.26: Mass spectrum for Au cluster beam recorded with an ionization wavelength of 193 nm (6.45 eV). At this wavelength only Au_9 and Au_{11} have ionization potentials low enough to have enough signal for a deflection experiment.

time of flight has been converted to deflection by the position sensitivity calibration and (2) where the deflection has been converted to polarization in Debye. This scale corresponds to how far a perfectly aligned dipole moment would be deflected in the field.

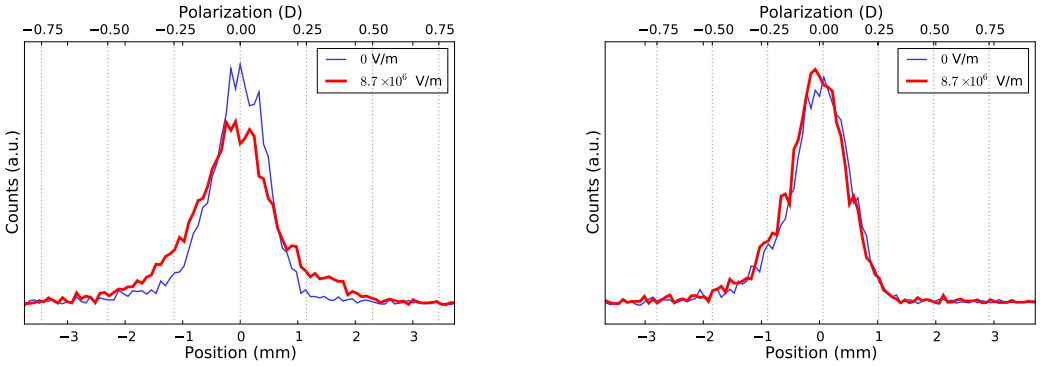

(a) Au_9 **(b)** Au_{11}

Figure 4.27: Deflection profiles for Au_9 and Au_{11}.

Two qualitative features of the profiles are worth comment: First, Au_9 shows deflection toward both the high field and low field directions. The deflections toward the high field side imply that the dipole moment spends the majority of its time oriented anti-parallel to the field.

If the dipole moment is 0.285 D, and the beam temperature is $T_R = 30$K, then $\frac{pE}{k_B T_R} = 0.02 \ll 1$ so the energy of the dipole moment in the deflection field is very small compared to the rotational energy. Thus we expect the field to exert a weak perturbation on the rotational motion of the cluster.

Although the qualitative features of the deflection profile, specifically the large width, and the symmetric deflection toward both sides unambiguously implies a dipole moment, there is still some systematic error possible with the use of a spherical rotor model to relate its numerical value to the broadening observed.

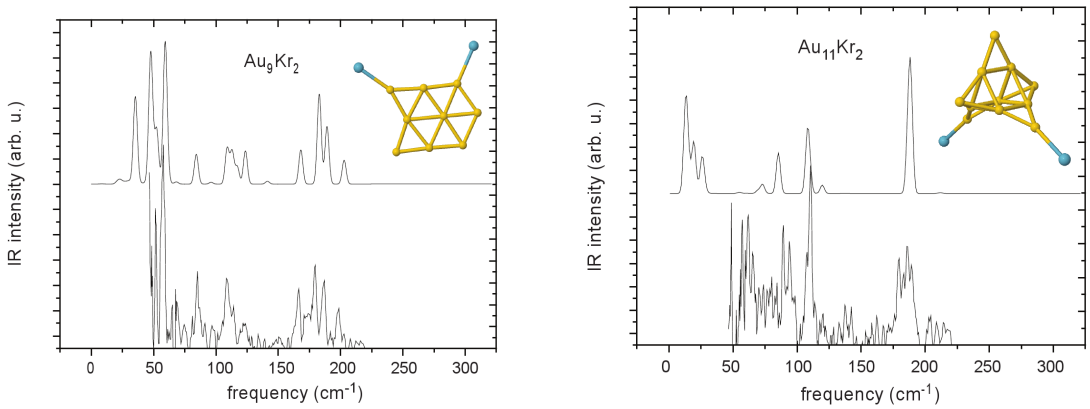

(a) Au_9 **(b)** Au_{11}

Figure 4.28: Far infrared spectrum measured with a free electron laser (FELIX) the experimental spectrum is compared with the theoretically calculated spectrum from DFT calculation. This result is due to for Au_9 and Au_{11}. The experimental setup was described in [63]

The structure of a cluster can be determined by using an optimization procedure to find an arrangement of atoms and bonds which matches an experimentally measured spectrum.

The because the attached rare-gas atoms break the symmetry of the cluster, the breathing modes (which would ordinarily not be IR active) can be included in the FIR spectra.

The measured FIR spectra shows vibrations at low energies - around 50 cm^{-1} for Au_9 and the theory predicts a band of vibrations at around 25 cm^{-1} for Au_{11}. Note that: 30 K $\approx$ 3 meV $\approx$ 25 $cm^{-}1$ so this is evidence that even in a beam temperature of 30 should be a substantial number of weakly vibrationally excited clusters in the beam. It is still doubtful

that having a few vibrations excited would make any difference in the thermal relaxation of electric or magnetic dipole moments, but it indeed interesting that the vibrations are accessible at this energies.

This is worth considering in light of the simple estimate of the lowest vibrational mode based on the "quantization" of acoustic waves. The Debye temperature of fcc gold is 150 K so a very crude estimate of the lowest vibration energy is $\frac{T_{\text{Debye}}}{N^{(1/3)}} \approx 72K \approx 59\text{cm}^{-1}$, which is reasonably close to what is seen in the measured spectrum.

4.7 Bismuth

In the bulk, bismuth is classified as a semi-metal. The technical meaning of this is that at zero temperature the carrier density will still be non zero. It has a very low conductivity (7.7×10^4 S/m), and a very low melting temperature (544 K). It is in the nitrogen group of the periodic table, it is most famous for the largest diamagnetic susceptibility [29] ($\chi = 1.5 \times 10^{-}4$) of any metal.

Unlike Lead, Bismuth does not become superconducting down to the lowest temperatures. This is again a consequence of the low density of states at the Fermi level.

Both of these above properties are highly dependent on the geometry of the crystal. If the Bi is deformed slightly then the band structure and thus the area of the Fermi surface changes. In fact there have been extensive ARPES studies of the surfaces of Bi (see ref. [75] for a review). At a crystalline surface the crystal will distort to reduce the surface energy. These distortions change the density of states, and this can have a dramatic effect, with some crystallographic faces becoming metallic, and others becoming semiconducting.

It is very easy to produce an intense pulsed beam of bismuth clusters in a laser vaporization source [115, 141, 164]. Of all of the materials we have worked with Bi produces the most intense cluster beam, for the smallest power of the ablation laser. The polarizability curve shows a rapid convergence to the bulk polarizability with a slight enhancement over it. Part of this enhancement reflects the partial orientation of the permanent dipole moments.

The most remarkable finding is the dipole moments. Bi clusters at low temperatures show dipole moments that are slightly smaller than Nb clusters, but they show the most consistent odd-even alternation observed in any element. The even-N Bi clusters have larger dipole moments than the odd-N clusters. It is unclear what if any the relationship is to the dipole moments of Nb,V,and Ta clusters which also show an odd-even alternation.

The dipole moments for Bi_N are independent of temperature in the range from 20 - 60 K. This suggests that there is a different mechanism from the dipole moments of Nb

clusters.

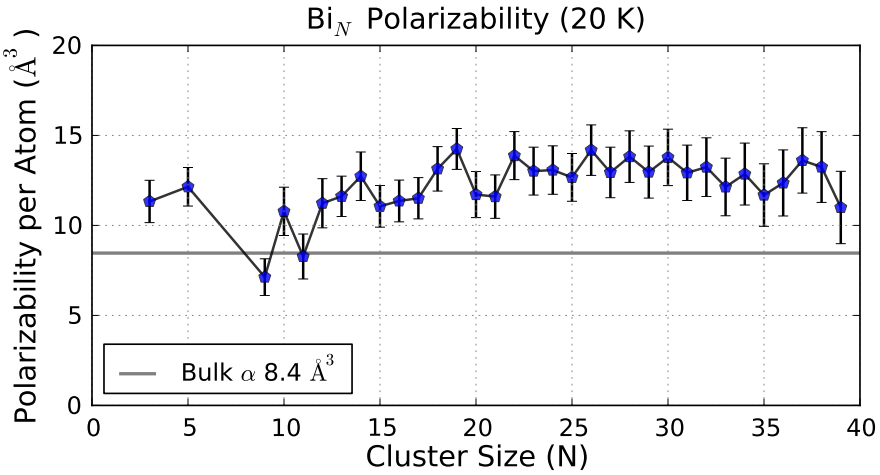

(a) Polarizabilities for pure bismuth clusters

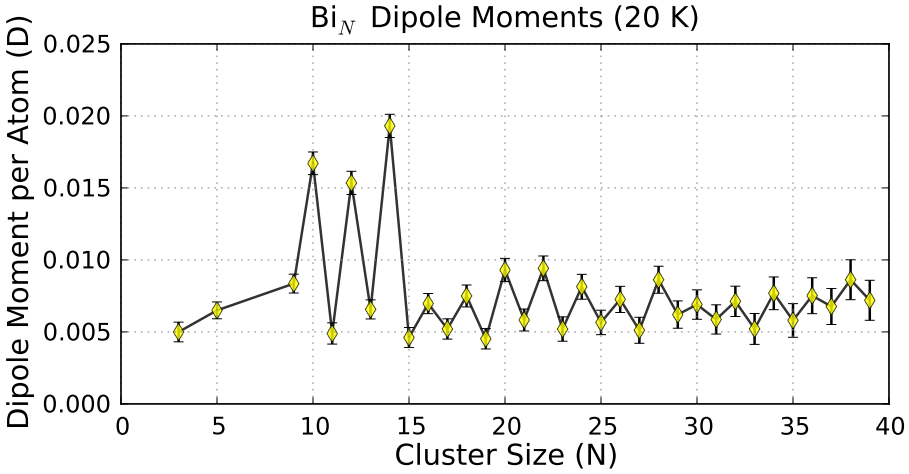

(b) Dipole moments per atom for pure bismuth clusters.

Figure 4.29: Polarizabilities and dipole moments for pure bismuth clusters. The polarizability is relatively close to the bulk value which suggests little spillout, and that the density of the clusters is very close to the bulk value. The dipole moments show a large odd-even alternation.

4.8 Rare Earths: Praseodymium, Terbium, Holmium and Thulium

The rare earth metals are trivalent and all are metallic in the bulk. They are all reactive with water and air and form a layer of oxide, Because of this oxide layer, the cluster beam produced by laser vaporization contains many single oxide, double oxide, and hydroxide clusters.

The main focus of our work on the RE's was their magnetic properties, but we will include the results of our electric deflection experiments on these elements in this chapter. They show a rich diversity of behavior. The results with oxygen doping for Tb_N are especially interesting. For some cluster sizes the addition of an oxygen atom gives a large enhancement of the dipole moment, while for other sizes doping with oxygen has no effect - almost as if the charge inhomogeneity had been eliminated by metallic screening.

The trends in polarizability are similar for Pr_N, Tb_N, and Ho_N. Tm_N shows radically different behavior.

4.8.1 Thulium Clusters: Fluctuating Dipole Moments

Figure 4.35 shows the effective polarizability of Tm_N clusters. It is very different from the other RE materials. Note the large peaks in the size trend polarizability of Tm_N compared to the other lanthanides. It is difficult to believe these enhancements as large as 60Å^3 per atom, can be accounted for by an unusual geometric structure or electronic spillout, thus the most likely explanation is a permanent dipole moment. The dipole moments derived from the beam broadening are too small to account for the observed polarizability enhancement. Further evidence against a rigidly fixed dipole moment is the small broadening (Figure 4.35 (b)) and the temperature dependence of the polarizability enhancement. (Figure 4.35 (a)) However, the deflection profiles are single sided and show little broadening - this implies that the dipole moment must be fluctuating inside of the deflection field.

This property is a great mystery at present and requires more study.

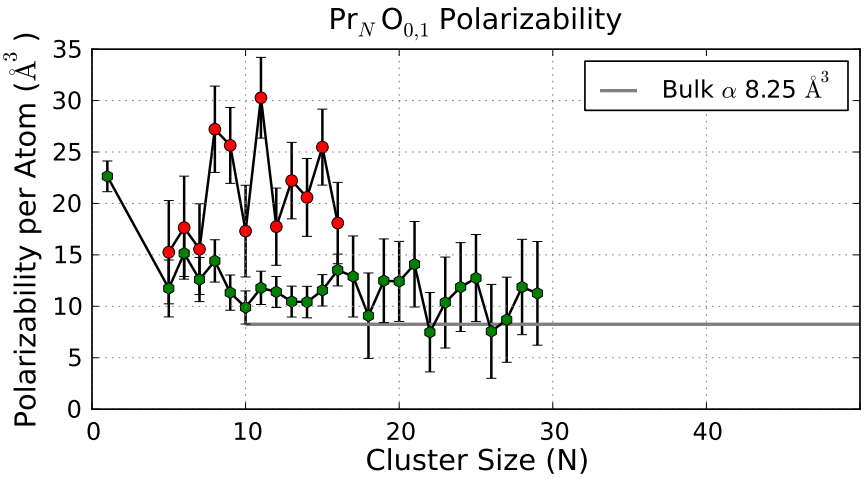

(a) Polarizabilities for praseodymium clusters

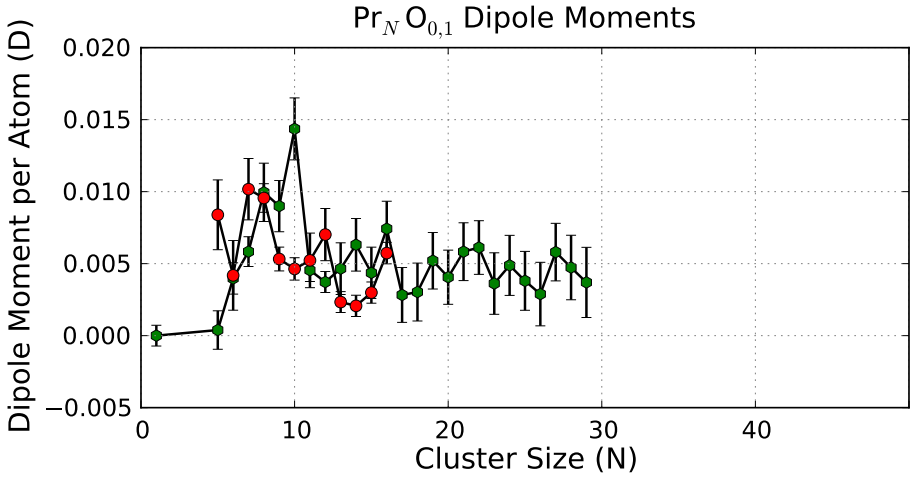

(b) Dipole moments per atom for praseodymium clusters.

Figure 4.30: Polarizabilities and dipole moments for pure and oxide praseodymium clusters. The error-bars are larger because there is an overlap of the pure cluster mass peak with the hydride. The Pr$_N$H clusters account for 5-10% of the total intensity. For the oxide the overlap with the Hydroxide becomes much larger and we have excluded this peaks from the measurement.

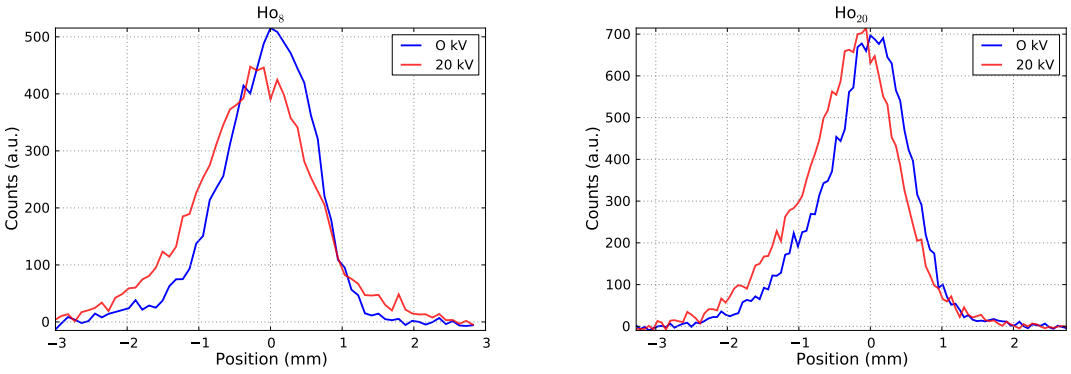

(a) Ho_8: 0.17 Debye

(b) Ho_{20}: 0.21 Debye

Figure 4.31: Deflection profiles for Ho_8 and Ho_{20}. Note the broadening of the deflection profile which is the signature of a permanent electric dipole moment. If we use a spherical rotor model in the $\frac{pE}{k_B T_R} \ll 1$, we get values of 0.17 D and 0.21 D for Ho_8 and Ho_{20} respectively. This estimate is only **semiquantitative** because we don't know the structure of the cluster and we have assumed that the rotational temperature is close to the source temperature. Symmetric tops have slightly different constants which relate the broadening to the dipole moment depending on whether the cluster is prolate or oblate. The beam broadening is far too large to be explained by an velocity dispersion or field inhomogeneities. For Ho_8 there is a clearly visible amount of deflection toward the low field direction which implies that the cluster has a net polarization parallel to the applied electric field. This is clear proof of a dipole moment.

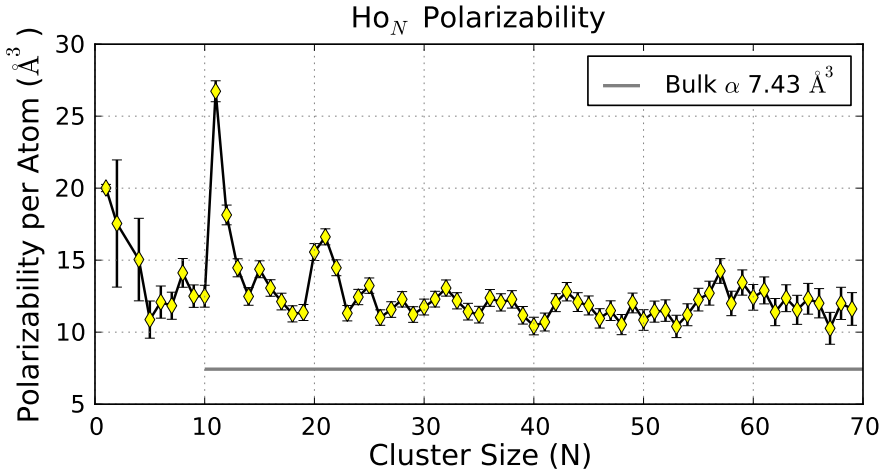

(a) Polarizabilities for pure holmium clusters

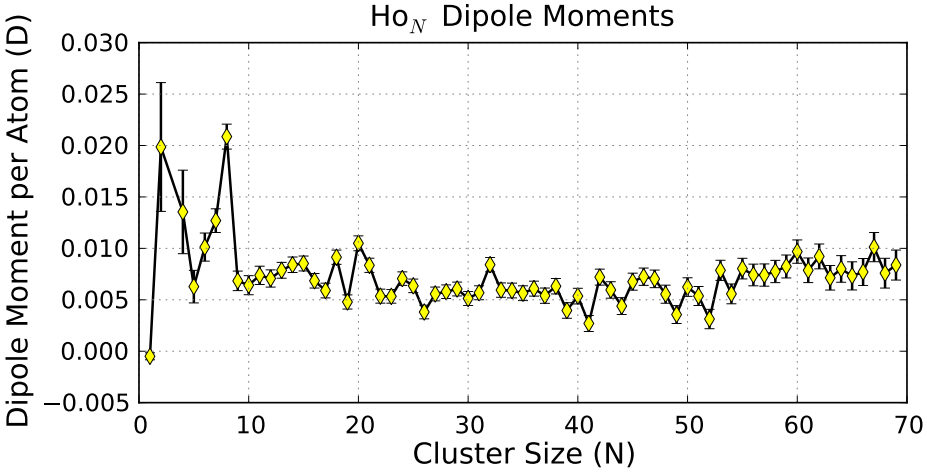

(b) Dipole moments per atom for pure holmium clusters.

Figure 4.32: Polarizabilities and dipole moments for pure holmium clusters. The polarizability is enhanced above the bulk value, and nearly all clusters show a small residual broadening consistent with dipole moments of around 0.005 D / atom. There are several sizes which stand out from the baseline with larger dipole moments.

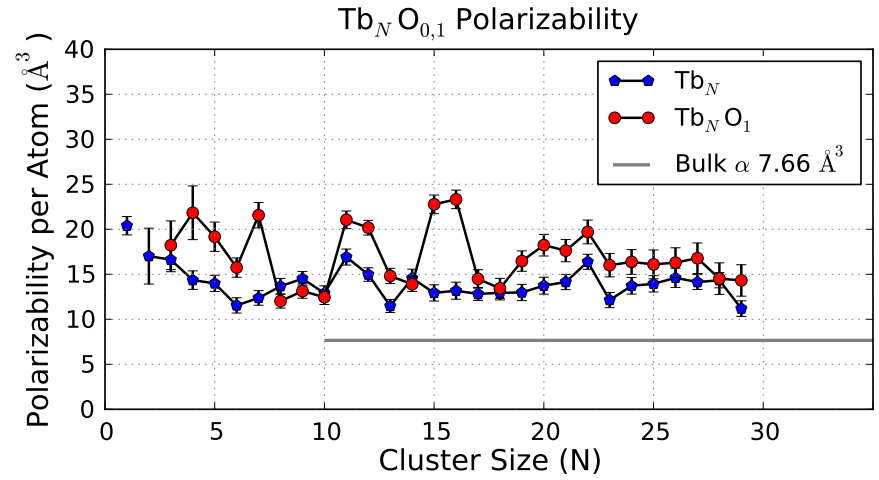

(a) Polarizabilities for terbium clusters.

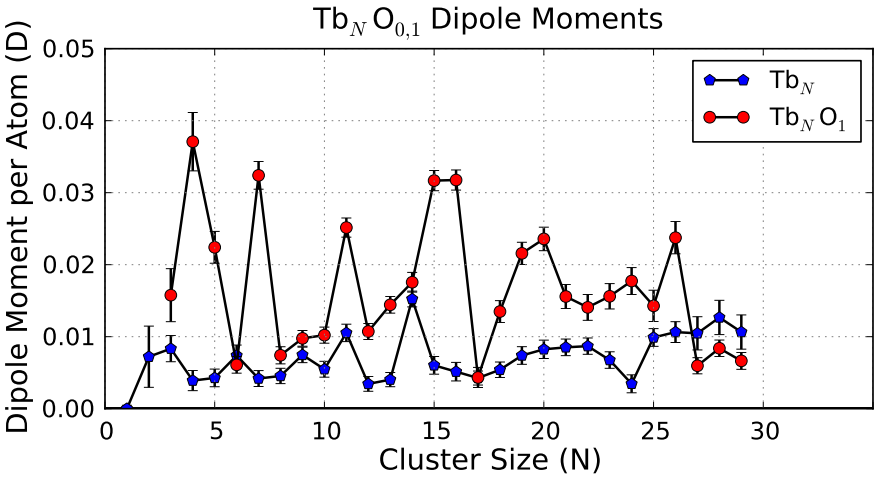

(b) Dipole moments per atom for terbium clusters.

Figure 4.33: Polarizabilities and dipole moments for pure terbium and terbium oxide clusters. For most sizes the addition of a single oxygen atom gives a dramatic increase, implying that the oxygen atom distorts the charge distribution in the cluster in a way which cannot be screened by the valence electrons.

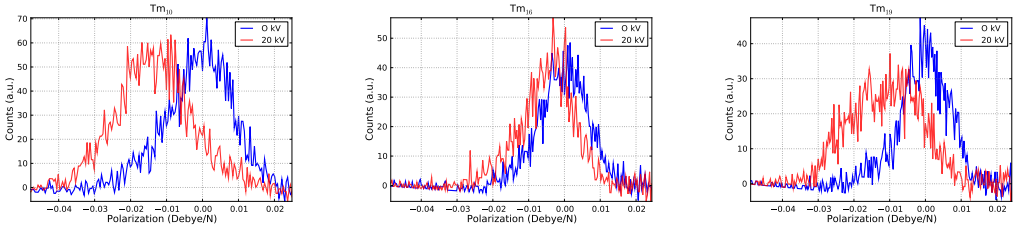

Figure 4.34: Electric Deflection Profiles for Tm Clusters

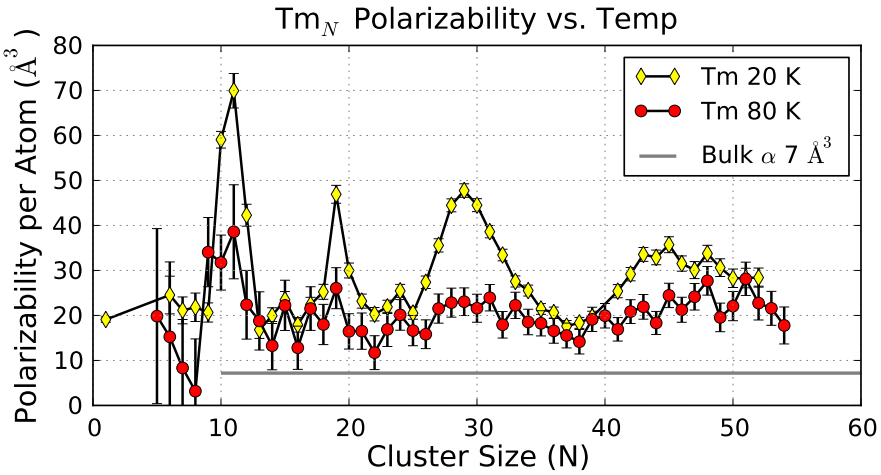

(a) Effective Polarizability for Tm$_N$ (

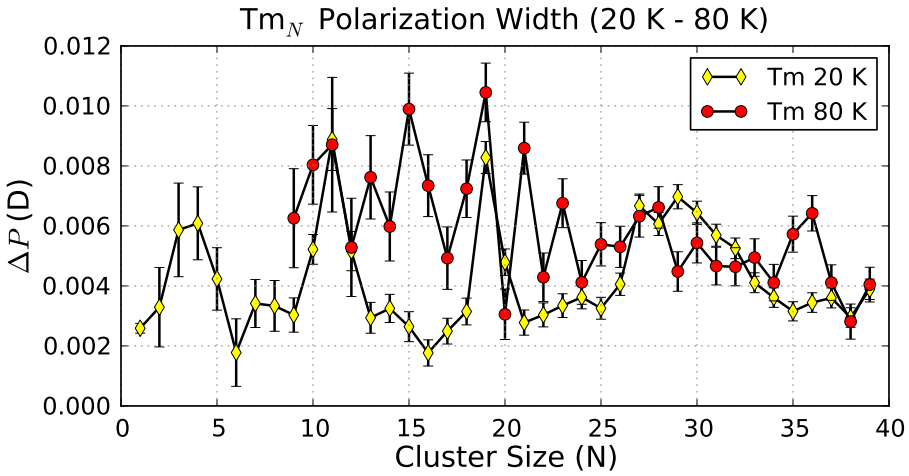

(b) Width of Polarization Distribution of Tm$_N$

Figure 4.35: Polarizabilities and dipole moments for Tm clusters at 20 K and 80 K. Note the very large reduction in the effective polarizability with increased temperature. The width of the polarization distribution shown in (b) shows little or no reduction with increase of temperature this suggests that there is a relaxation process taking place. Possible explanations include (1) chaotic tumbling, (2) large amplitude shape fluctuations or rapid isomerizations reactions.

CHAPTER V

MAGNETISM OF RARE EARTH CLUSTERS

5.1 Background

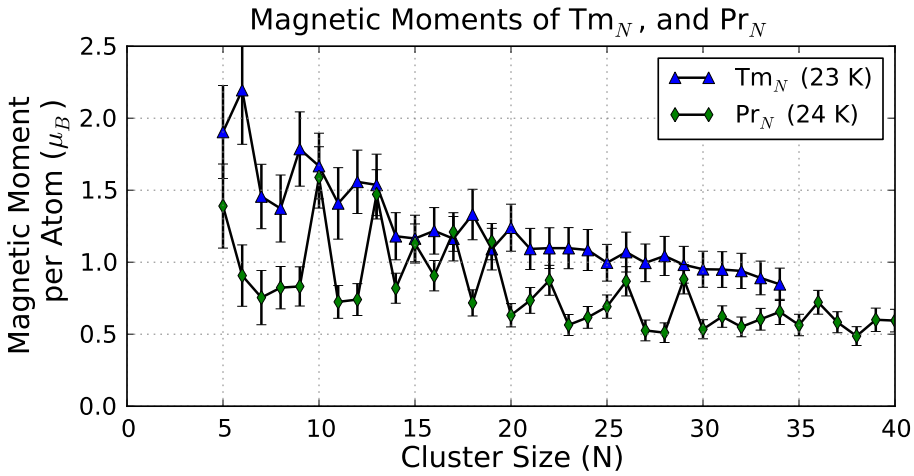

Figure 5.1: Magnetic moments per atom for Pr and Tm clusters at a temperature of 15 K.

This chapter presents a series of Stern-Gerlach deflection experiments on free cluster beams made from the lanthanide series of elements. (Pr_N, Ho_N, Tb_N, and Tm_N) The lanthanide series of the periodic table is constructed from the filling of the atomic $4f$ shell. The atomic moments of these elements are due to the combined spin and orbital moments of the partially filled $4f$ shells. Because these $4f$ shells remain close to the nucleus, in many cases the atomic moments are preserved in the solid state.

The direct exchange between neighboring $4f$ shells is negligible so the exchange which couples together the atomic moments is indirect and mediated through an oscillating spin polarization of the conduction electrons, called the RKKY (Ruderman, Kittel, Kasuya, Yosida) interaction.

Depending the exact distance between two atomic sites the coupling can be ferro or anti ferromagnetic. These competing magnetic interactions responsible for the rich varieties of

magnetic order which are found in the bulk rare earth metals. Examples include the helical anti-ferromagnetic phase found in Ho and Tm.[78]

There have been many studies of rare earth clusters of Gd, Dy, and Tb before, but to our knowledge, this is the first experimental study on the magnetic properties of free Pr, Ho, or Tm clusters. We performed magnetic deflection experiments on all four pure elements over a wide range of fields and temperatures. In order to facilitate a comparison across the elements we analyze the profiles by calculating the Langevin magnetic moments from the average magnetization $\bar{M}$.

$$\mu = L^{-1}(\bar{M}) \tag{5.1}$$

$$\mu = \approx \sqrt{\frac{3\bar{M}kT}{B}} \tag{5.2}$$

Where the approximation is valid in the low-field / high temperature region. Pr and Tm clusters appear to follow the Langevin law rather well, Tb and Ho are very different and as the temperature is raised from 20 K to 200 K they show large apparent changes of their net magnetic moments accompanied by large changes in the width of the deflection profiles.

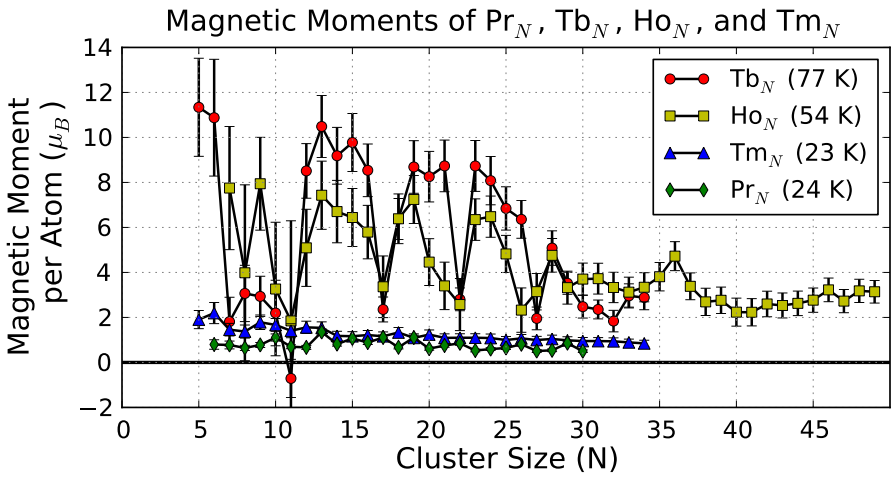

Figure 5.2: Magnetic moments per atom for the 4 lanthanide cluster systems studied. The magnetic moments are calculated by applying the Langevin formula to the average magnetization. For all of the elements, the field dependence of the magnetization is consistent with the Langevin theory, meaning that the moments calculated from experiments with different deflection fields give the same magnetic moments. The magnetic moments of Tb_N and Ho_N appear to decrease as the temperature is increased. The point we wish to emphasize here is how similar the trends with cluster size are for Tb_N and Ho_N.

5.2 Summary

5.2.1 Praseodymium Clusters

Unlike the bulk material which is non-magnetic down to 50 mK [78], Pr clusters are magnetic up to at least room temperature. The crystal field splitting is very large in Pr (13 meV), and as a result the ground state for the Pr ion in the crystal is a singlet state with no magnetic moment. The paramagnetism of Pr follows the law of van Vleck where the magnetic moment is restored by a perturbative mixing of with excited states with larger magnetic moments. In a cluster the geometric structure is very different with lower symmetry so it is more likely that the Pr ions retain some of their atomic moments.

Praseodymium clusters have small magnetic moments of $\approx 1 - 2\mu_B$/atom. (see Figure 5.1) This is confirmed by many experiments over a range of fields and temperatures. The magnetization of Pr_N is well-described by the Langevin susceptibility. The magnetic moments of most Pr clusters are independent of temperature, but certain sizes (e.g. $N = 13$) show a significant change in the moment with temperature. There is also a consistent odd-even alternation in the moments from N=10 - N=20, with odd-N clusters showing slightly larger per-atom magnetic moments.

The low moments and temperature response can be explained by a Heisenberg model (see ref. [32, 114]) with competing ferro and anti-ferromagnetic interactions between the atomic moments in the cluster. This frustration of the local moments can result in the formation of a canted ground state where the local moments are oriented non-collinearly, which reduces the net magnetic moment.

This ground state calculated in Ref. [32] has many spin excited states separated from the ground state by small gaps, so the magnetization should be highly sensitive to temperature. The calculated temperature dependence of the magnetization is shown that in Figure **??**

Our experiment can not distinguish between the case where the net magnetic moment is reduced due to antiferromagnetism or canting, and a case where (like the bulk material) the local moments of lattice sites is reduced through a crystal field splitting of the atomic

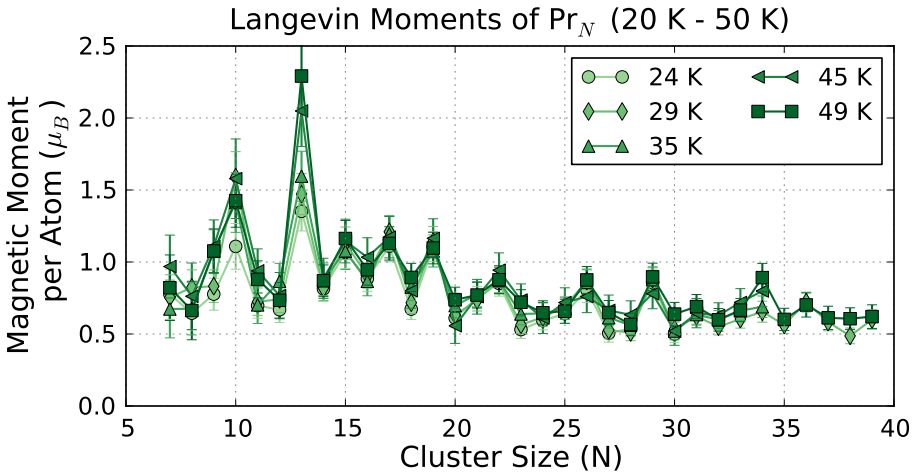

(a) Pr_N Langevin Moments per Atom for $T = 20 - 50$ K

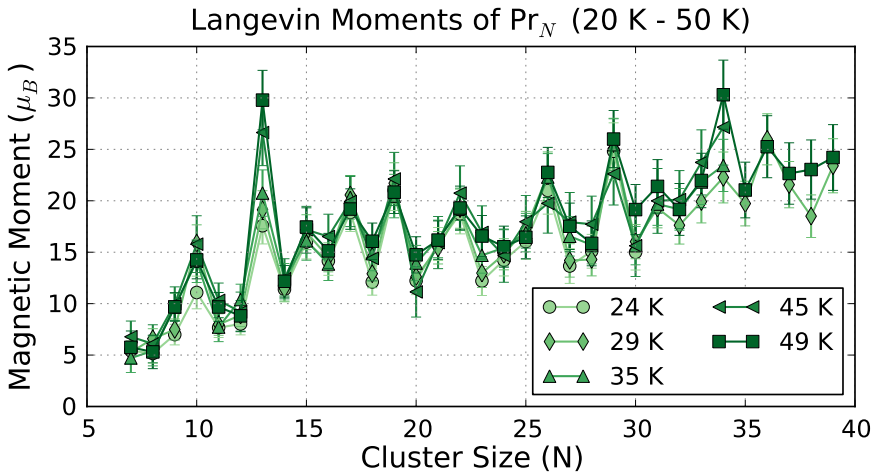

(b) Pr_N Langevin Total Moments for $T = 23, 51$ and 160 K

Figure 5.3: Per atom and total magnetic moments of praseodymium clusters for temperatures 20-50 K. The magnetic moments (derived from the Langevin function) of most Pr clusters show no significant temperature dependence in this range of temperatures. Exceptions include Pr_{10}, Pr_{13}, and Pr_{34}. The field dependence of the magnetization is also consistent with the Langevin form, and several of the series plotted above represent an average over multiple experiments at different fields.

$4f$ levels. All we measure is the *net* magnetic moment.

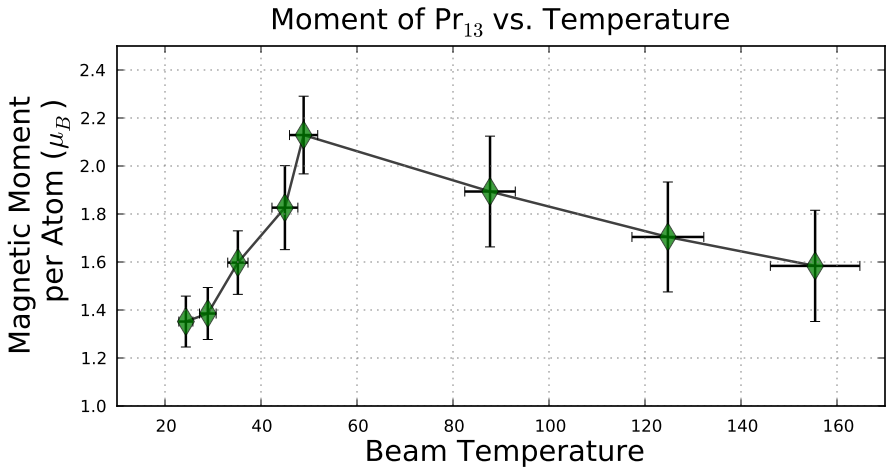

Figure 5.4: Temperature dependence of the Langevin moment of Pr_{13}. This behavior is similar to a model proposed by Cirovski et. al.

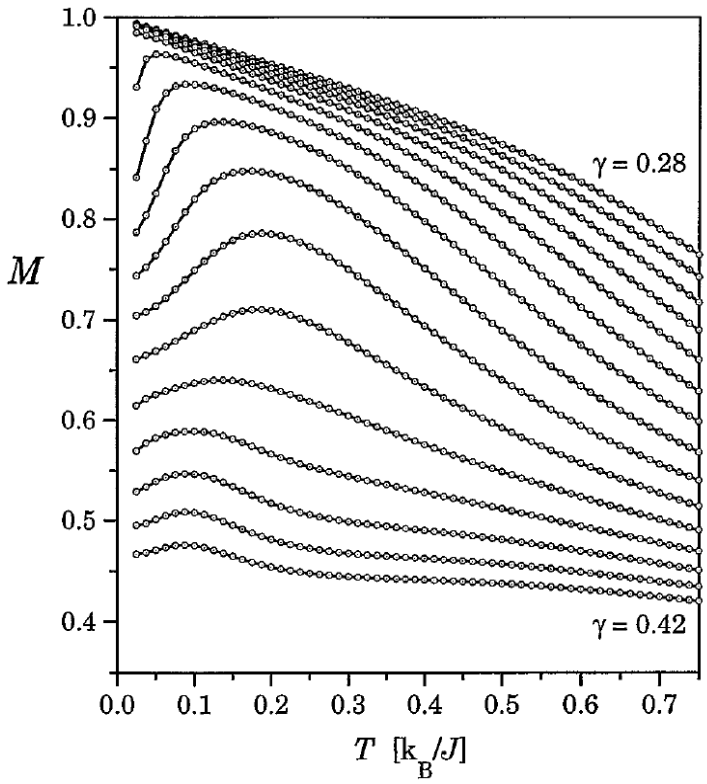

Figure 5.5: Temperature dependence of the magnetization in the model calculated by Cirovski et. al. [32] γ is a parameter of the model which models the ratio of the strength of the nearest neighbor ferromagnetic coupling to the next-nearest neighbor anti-ferromagnetic coupling.

5.2.2 Thulium Clusters

Like Pr_N, Tm_N shows very small per atom magnetic moments (2.5 - 1.0 μ_B/N), well below the atomic value of 7.5 μ_B. Unlike Pr_N however, Tm_N shows a small but significant change in the magnetic moment for temperatures between 20 - 189 K.

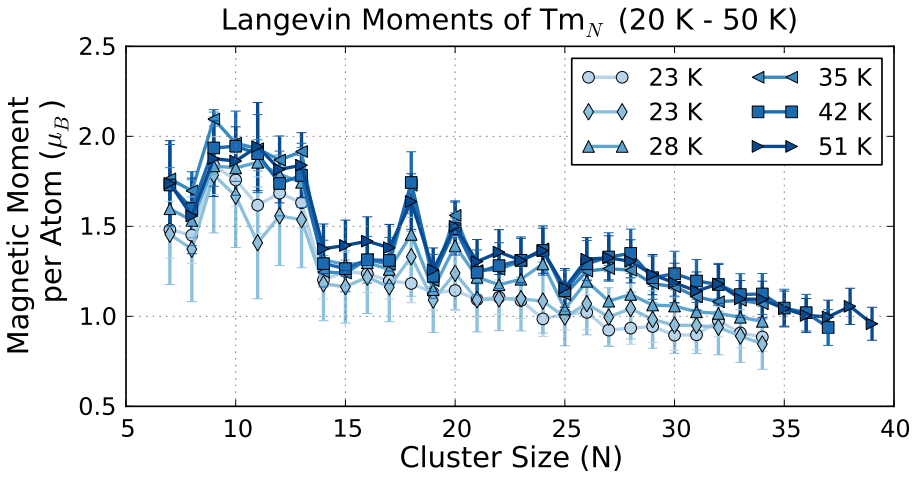

(a) Tm_N Langevin Moments for $T = 20 - 50$ K

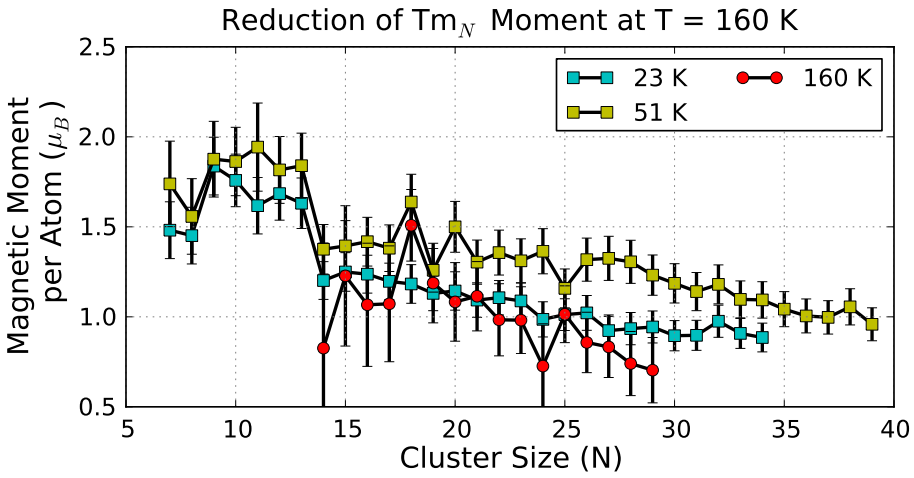

(b) Tm_N Langevin Moments for $T = 23, 51$ and 160 K

Figure 5.6: Temperature dependence of the Langevin moment of Tm_N. There is a small but significant increase in the moment from 20 - 50 K. Some clusters sizes show a larger increase than others. (e.g. Tm_{20} and Tm_{20}. The magnetic moment, measured by the Langevin function decreases once again as the temperature is raised further. At $T = 160$ it returns to its value at 20 K. Note that the changes in the measured magnetic moments are very small, but they vary from cluster size to cluster size. Also the rising and falling of the apparent magnetic moment has been predicted by the geometric frustration model given in [114, 32]

5.2.3 Holmium and Terbium

Ho_N and Tb_N show similar size dependence in their magnetic moments with local minima at the same cluster sizes. Many of these local minima have been previously observed in Gd, Tb, and Dy clusters [35, 26]. This close parallel between the different elements suggests that these clusters have similar structures.

If we refer to Figure 4.33 in the previous chapter which measured the change in the electric dipole moment of Tb_N when a single oxygen atom was added we find that the dipole moments of Tb_NO_1 has local minima at the same cluster sizes (N = 17, 22, and 27) that the magnetic moment of pure Tb_N clusters shows a local minima.

Attachment of an oxygen atom should distort the charge distribution inside of the cluster, as the remaining non-oxidized conduction electrons attempt to screen the charge inhomogeneities of the oxygen atom. Our conclusion is: the cluster sizes which have reduced magnetic moments relative to their neighbors (N = 11, 17, 22, 27) are also more effective than their neighbors at screening out the charge inhomogeneities caused by attachment of an oxygen atom. This relation completely fails for N = 11.

Tb_N shows a large reduction in μ for temperatures above 120 K. This has been explained by [35, 26] as a transition from locked moment to superparamagnetic behavior. However our interpretation is different. We do not observe the two-sided deflections which would be expected of locked-moment behavior at low temperature. This suggests that some other dynamical process is determining the deflection dynamics. The detailed theory remains to be worked out.

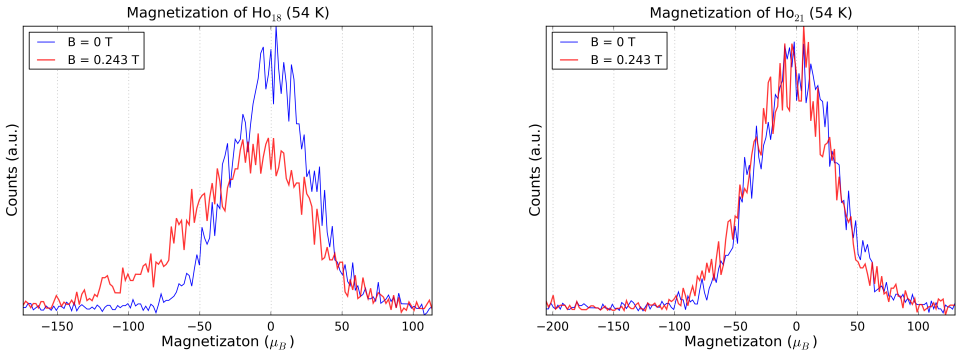

Figure 5.7: Magnetic deflection profiles of two Ho clusters showing the single sided deflections.

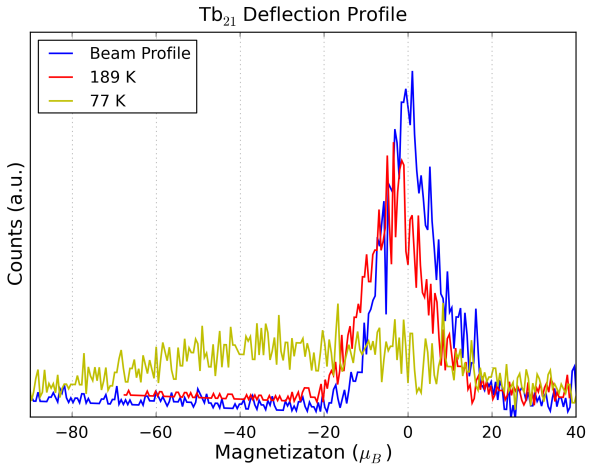

Figure 5.8: Magnetization distribution for Tb_{21} taken at 77 K and 189 K. This illustrates the large change in magnetic response that takes place as the temperature is increased. The width of the profile is reduced, and the magnetic moment (calculated by the Langevin function is reduced by a factor of 3.

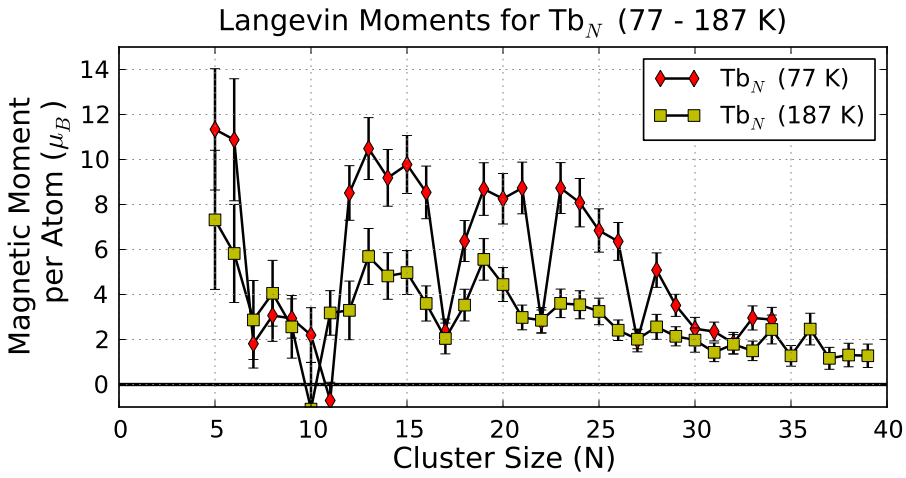

Figure 5.9: Temperature dependence of the Langevin moments for Tb_N for Tb_N clusters.

5.2.4 Effect of Oxygen Doping

Doping with oxygen has little effect on the magnetism of rare earth clusters. (Figure 5.10) Exceptions include Tb_7 and Tb_{21}. Tb_7 also acquires a large electric dipole moment when oxygen is attached, and its magnetic moment is greatly enhanced. Oxygen gives a slight enhancement to the electric dipole of Tb_{21} and reduces the magnetic response.

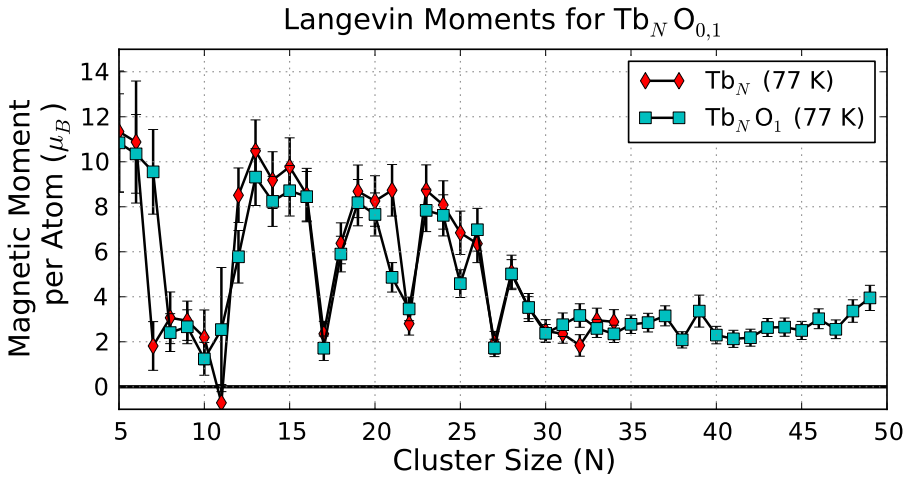

Figure 5.10: Langevin magnetic moments for $Tb_N O_{0,1}$ clusters measured at 77 K.

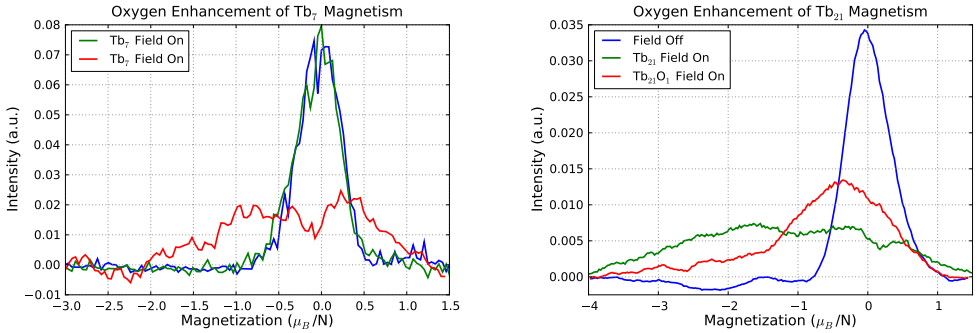

Figure 5.11: Deflection profiles for two Tb clusters which show a large change in magnetism upon oxygen doping. Tb_7 has a tiny moment while while Tb_7O_1 shows a large enhancement to $6\mu_B$ / atom. Tb_{21} shows a large reduction in its magnetic moment upon the addition of a single oxygen atom. These two are exceptions - oxygen shows no effect on most of the Tb_N clusters measured. This is similar to the earlier findings of ref. [26]

5.3 Previous Work

Previous experimental studies have explored the properties of Gd_N [44, 45, 35, 26, 59] Dy_N [122, 123, 26, 35], and Tb_N clusters [35, 26]

The conclusions of the previous studies cited above were not all in agreement with one another. Refs.[44, 45, 35, 26] described the deflection profiles as consisting of two populations - one "locked-moment" population with a long broad tail, and a superparamagnetic population which was narrow in width and followed the Langevin law. The relative fraction of these two populations changed with temperature, with the SP fraction dominating at higher temperatures. The "magic number" sizes (which are the local minima in Figure 5.1) were claimed to be superparamagnetic at all temperatures. There also reported some addition observations which could not be explained within this framework, such as magnetic moments that increased with temperature.

A major difficulty with applying the locked moment model to the analysis of the Tb, or Ho deflection profiles is that the locked moment model (see Chapter. 3) predicts two-sided deflections especially in the low field. This does not even qualitatively agree with the experimentally observed profiles which are all single sided.

Gerion et. al. in Ref. [59] challenged the two species conclusion by noting that the central peak in the low-temperature profiles for Gd_{22} described in [35] does not follow the superparamagnetic response ($M \propto B/T$). This suggests that there is some other mechanism responsible for the observed long tails at low temperature.

There were also several theoretical attempts to address these experimental findings [114, 32, 102], and the critical importance of geometric structure on the magnetic properties of these cluster systems was recently studied by López-Urias et. al. [102].

5.4 Overview of Bulk Lanthanide Magnetism

There have been many highly detailed studies of bulk lanthanide magnetism, and many of the known facts are nicely summarized in two excellent books refs.[78, 147].

Table 5.1 summarizes the ionic magnetic moments and the bulk saturation magnetization of the lanthanide elements.

Table 5.1: Summary of atomic and bulk saturation magnetic moments for rare earth metals. Data is taken from various tables found in refs. [6, 78, 147]. T_C is reserved for a true transition to ferromagnetism. T_N refers to a transition to either an antiferromagnetic or a helical antiferromagnet.

Element	μ_{atomic} (μ_B)	μ_{sat}	structure	T_N	T_C
Ce	2.54	0.6	dhcp/fcc	13.7	-
Pr	3.58	2.7	dhcp	0.05	-
Nd	3.62	2.2	dhcp	19.9	-
Pm	3.68	-	dhcp	-	-
Sm	0.85	0.13	rhom	14.0	-
Eu	0.00	5.1	bcc	90.4	-
Gd	7.94	7.63	hcp	-	293
Tb	9.72	9.34	hcp	230	220
Dy	10.64	10.33	hcp	179	89
Ho	10.60	10.34	hcp	132	20
Er	9.9	9.1	hcp	85	20
Tm	7.56	7.14	hcp	58	32
Yb	4.53	9.320	fcc	-	-

5.4.1 Heisenberg Model with Competing Interactions

The simplest model of the magnetism of the 4f elements views them as a prototype of local moment or Heisenberg model of magnetism. In this picture each atomic site has a localized magnetic moment that is coupled by an exchange interaction to the moments of its neighbors. The total spin Hamiltonian has the form:

$$H_{\text{Heisenberg}} = -\sum_{i<j} J_{ij}\mu_i \cdot \mu_j \tag{5.3}$$

μ_i is the local moment on site i, and the summation is over all pairs of atomic sites. This model is very flexible in that the exchange constants J_{ij} are not necessarily equal for all pairs of atomic sites. This allows some pairs of sites to be coupled by ferromagnetic bonds and other pairs of sites to be coupled by anti-ferromagnetic bonds.

There are few exactly soluble cases of this model, so in practice it is simpler to simply run numerical simulations. The simplest case of such a frustrated magnetic lattice is a triangle of local moments with all pairs of moments coupled by an antiferromagnetic bond. All of the exchange bonds cannot be satisfied simultaneously, so the system must compromise. One possibility is to take on a non-collinear arrangement of the spins called a canted arrangement.

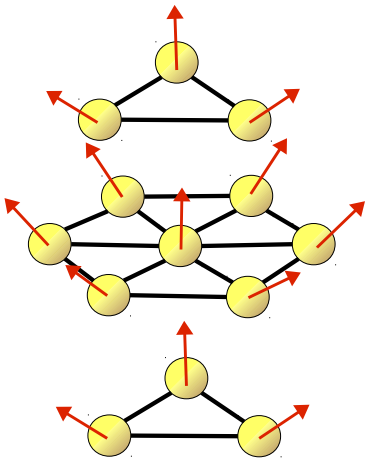

Figure 5.12: Cartoon illustrating the canted spin arrangement for Gd_{13}, described by Pappas et.al.[114]. The non-collinear arrangement of spins is a consequence of the spin frustration that results from competing ferro and anti-ferromagnetic interaction within the cluster. Note that this illustration is only a cartoon. There have been no direct observations of this spin arrangement.

In the bulk lanthanides, the exchange constant J_{ij} between two lattice sites is taken to be a function of the distance between these two sites $J_{ij} = J(|R_i - R_j|)$.

$$J(R) = J_0 \frac{2k_F R\cos(2k_F R) - sin(2k_F R)}{(2k_F R)^4} \tag{5.4}$$

The decaying oscillations in the spin polarization of the conduction electrons is analogous to the Gibbs phenomenon or ringing oscillations that result when one tries to approximate a discontinuity in a function by a sum of a finite bandwidth of sinusoids. In order for

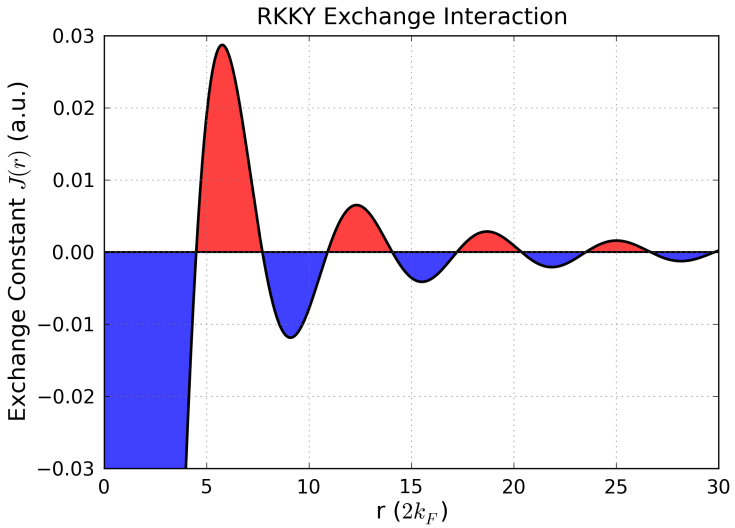

Figure 5.13: Spatial dependence of the indirect exchange (RKKY) interaction in bulk rare earth metals. For spins in the red-shaded are the coupling is ferromagnetic while spin in the blue shaded area experience an antiferromagnetic interaction. In bulk materials this spatial dependence has a key role in the spatially modulated forms of magnetic order which occur. While the assumptions used to derive this specific form are of doubtful validity in a finite cluster, the general principle of an exchange interaction mediated through the conduction electrons should still apply[32, 114]

the conduction electrons to completely cancel the local moment of the ion, it would have create a spin polarization which varies on the length scale of ion. The smallest length scale on which the spin polarization of the conduction electrons can vary is determined by the "bandwidth" of available electronic states near the Fermi level. Because this bandwidth is finite, there will be "ringing".

In a simple cluster, the electronic wavefunctions aren't planewaves - they are at best more like spherical standing waves. So the spatial dependence of the indirect exchange interaction is likely to be very different. Ref. [114] assumed a form where nearest neighbor atoms were ferromagnetically coupled while next nearest neighbor atoms were antiferromagnetically coupled. The existence of magnetic order proves that there is still some exchange coupling, so the RKKY mechanism must still be operative.

5.5 Summary and Conclusions

In conclusion we have developed the following novel findings in rare earth clusters.

- Pr and Tm are both magnetic with small 1 - 2.5 μ_B moments per atom. The atomic moments are 3.6 μ_B and 7.6 μ_B respectively. This suggests that the arrangement of atomic moments in the cluster is such that there is a lot of net cancellation.

- Tb_N and Ho_N show similar size dependent trends, with local minima at the same cluster sizes and a sharp reduction in the apparent magnetic moment at around 200 K.

- The Tb_N clusters which have very low magnetic moments are also the ones that are most effective at screening out distortions of the cluster charge density due to oxygen doping.

CHAPTER VI

SUMMARY AND CONCLUSIONS

Here we state our conclusions and the outlook for future work. We have presented a series of measurements of the electric and magnetic response of metal clusters at low temperature. Our experimental data probes cluster sizes which are large enough so that they are intractable to be studied using quantum chemical methods like density functional theory. To understand these experiments more sophisticated and inspired theoretical methods are needed.

6.1 Dipole Moments and Cluster Metallicity

Our electric deflection experiments have allowed us to measure the polarizabilities and electric dipole moments of 15 elements. These elements have different atomic structures and thus the bonding in these clusters covers many different types. Like the bulk material, Na clusters show metallic bonding where the valence electrons are weakly perturbed by the ionic core potential. The valence electrons of transition metal clusters are partially derived from atomic *d* orbitals and they are expected to be partially localized in directional bonds.

Inside of a finite cluster, the localization of electrons in bonds implies that their motion is restricted, and they are thus unable to screen charge inhomogeneities. This imperfect overlap of the centers of positive and negative charge will give the cluster a nonzero dipole moment.

It is apparent from the experimental record that most metal clusters measured do in fact, have small dipole moments. Na is the exceptionally perfect metal in this sense. Of the transition metals, Co, and Fe clusters come closest to the metallic ideal.

One curious finding that is not yet understood is that the measured dipole moments tend to scale linearly with the number of atoms, so that the dipole moment per atom is constant.

Clusters made of different materials have different values for this constant polarization. It would be very nice to know if this trend holds for clusters with thousands of atoms. Obviously, in the bulk limit all of these materials are metallic conductors so the polarization must converge to zero, but we have apparently not made contact with the bulk limit.

Another experimental finding which is highly relevant to the issue of screening and metallicity is the effect of oxygen doping on the cluster polarizations and dipole moments. The attachment of a single oxygen atom to the cluster surface should significantly distort the distribution of charge inside of the cluster because of oxygen's different electronegativity. A metallic particle with mobile electrons should be able to screen this distortion. In many cases the addition of a single oxygen atom to a metal cluster has very small or no detectable effect on the polarizability or dipole moment. The most outstanding example of this is MnO clusters. We have also observed many cases where oxygen has a dramatic effect on the dipole moments (e.g. Pr and Tb clusters)

6.1.1 Importance of Odd-Even Effects

Odd-Even effects are very common in clusters. The standard explanation given [67] is that a cluster system will distort to break every degeneracy, except for the spin degeneracy which cannot be broken by a shape distortion. This last remaining spin degeneracy implies that the electronic orbitals are filled in pairs, with the odd-N clusters having to fill an empty orbital higher in energy than the highest pair. This type of explanation is plausible for the odd-even alternation observed in the ionization potential of Na clusters where the difference in IP between the even-N and odd-N clusters is as large as 0.1 eV. There have recently been several observations of odd-even effects in the response of large clusters to an applied electric fields. It is unclear whether this explanation can successfully account for these effects.

Nb, V, and Ta clusters have anomalously large dipole moments. But their most exceptional property which appears at low temperature is the strong odd-even alternation of the

dipole moment, which persists up to sizes as large as $N = 120$ in the case of Nb.

Our work has found that Bismuth also shows a consistent odd-even alternation in both it's polarizabilities and dipole moments. (It is unclear whether Bi is displaying the same phenomenon as Nb,V, and Ta.

To make a comparison across the elements of the odd-even alternation we can plot the second differences of the per-atom dipole moments. To illustrate the effect of gold doping on Nb and Ta clusters we also include the comparison of the second differences for these two systems.

6.1.2 Thulium Fluctuating Dipoles

Another issue that needs further study is the large change in the electric response of thulium clusters with temperature. Such large changes in the response at such low temperatures have been observed in electric deflection experiments on Sn clusters, and an explanation based on non-rigid structures was invoked [133]. Far infrared spectroscopy, which directly probes the vibrational modes of a cluster is a promising technique to investigate these structures.

6.2 Rare Earth Cluster Magnetism

Praseodymium clusters were found to magnetic at room temperature where the bulk material remains in a paramagnetic state down to 50 mK. Bulk Pr is non-magnetic because the crystal field splits the f orbitals and quenches the atomic moment. Despite this, the per atom magnetic moments are smaller than the atomic moments which suggests that there is antiferromagnetic or canted arrangement of the spins.

By comparison, Tb and Ho clusters have much larger per atom magnetic moments, with the exception of specific "magic" sizes which have much lower per atom moments.

For future work, other experimental methods should be employed to attempt to find what is unique about these magic sizes. The ionization potentials of lanthanide clusters have not yet been measured, and photoelectron spectroscopy can provide insight into the

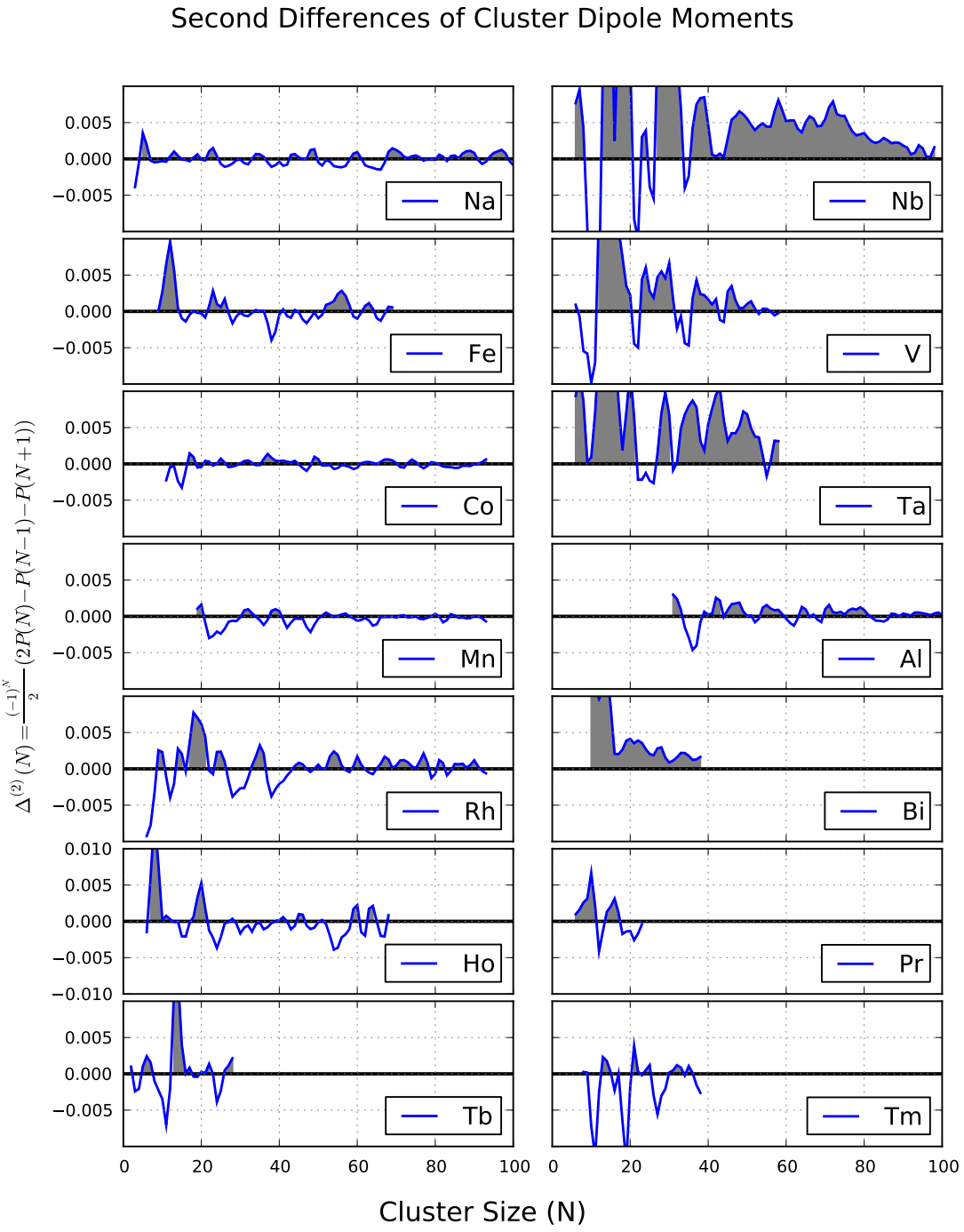

Figure 6.1: Plot of the second differences in the per atom dipole moment for all of the metal cluster systems studied in this thesis. The second difference convention comes from the literature on Nuclear binding energies.

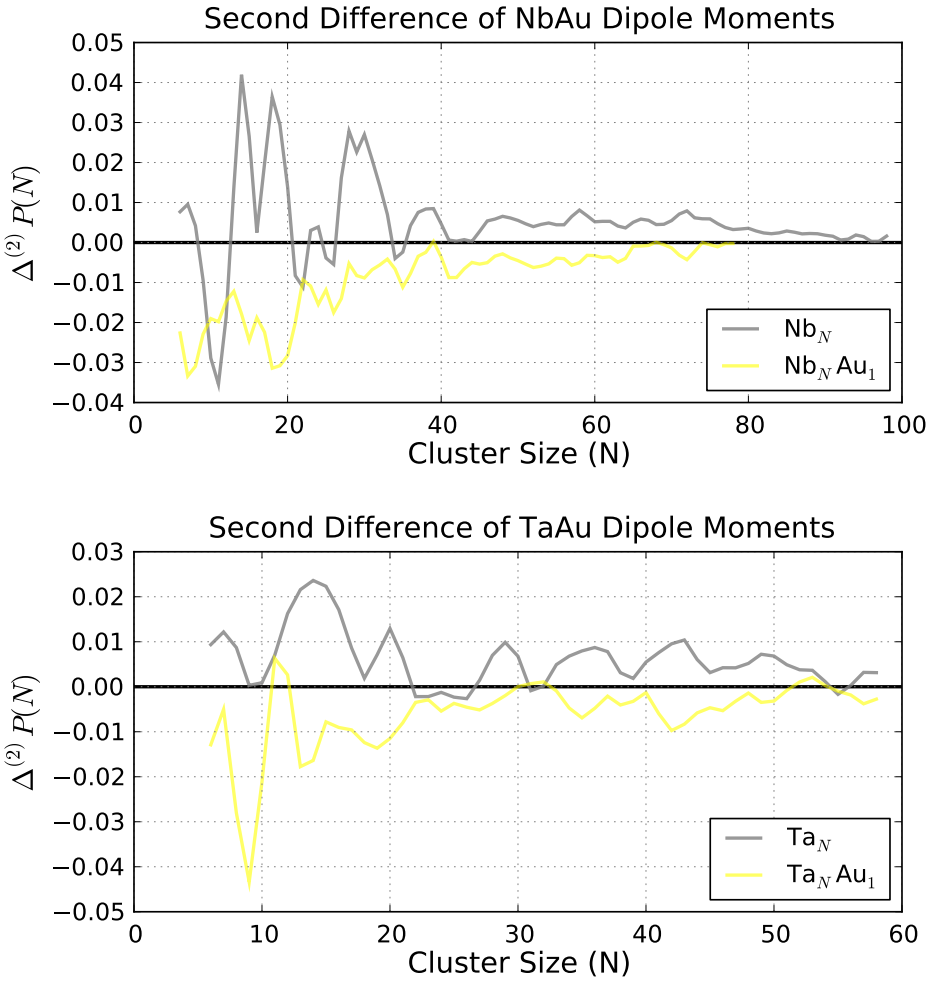

Figure 6.2: Second differences applied to $Nb_N Au$ and $Ta_N Au$ alloy clusters. The addition of a single Au atom inverts the odd even alternation. This is shown in the graphs.

electronic structure and the density of states.

It would also be very interesting to investigate the change in the magnetic behavior of the lanthanide clusters as the are doped with a trivalent non-magnetic impurity like Yttrium.

REFERENCES

[1] Akola, J., Häkkinen, H., and Manninen, M., "Ionization potential of aluminum clusters," *Physical Review B*, vol. 58, no. 7, pp. 3601–3604, 1998. 4.3

[2] Andersen, K., Kumar, V., Kawazoe, Y., and Pickett, W., "Origin of spontaneous electric dipoles in homonuclear niobium clusters," *Physical Review Letters*, vol. 93, no. 24, p. 246105, 2004. 4.2

[3] Andersen, K., Kumar, V., Kawazoe, Y., and Pickett, W., "Origin and temperature dependence of the electric dipole moment in niobium clusters," *Physical Review B*, vol. 73, no. 12, p. 125418, 2006. 4.2, 4.2.1

[4] Antoine, R., Compagnon, I., Rayane, D., Broyer, M., Dugourd, P., Breaux, G., Hagemeister, F., Pippen, D., Hudgins, R., and Jarrold, M., "Electric dipole moments and conformations of isolated peptides," *European Physical Journal D*, vol. 20, no. 3, pp. 583–587, 2002. 2.2.2

[5] Antoine, R., El Rahim, M., Broyer, M., Rayane, D., and Dugourd, P., "Asymmetric top rotors in electric fields. II. Influence of internal torsions in molecular beam deflection experiments," *J. Phys. Chem. A*, vol. 110, no. 33, pp. 10006–10011, 2006. 2.2.2, 3, 4.2, 4.5.1

[6] Ashcroft, N. and Mermin, N., *Solid Stale Physics*. 1976. (document), 1.2.1, 4.1, 4.3, 5.1

[7] Bartels, C., Hock, C., Huwer, J., Kuhnen, R., Schwobel, J., and von Issendorff, B., "Probing the angular momentum Character of the valence orbitals of free sodium nanoclusters," *Science*, vol. 323, no. 5919, p. 1323, 2009. 1.1, 4.1, 4.1.1

[8] Becker, R. and Döring, W., "Kinetic treatment of grain formation in supersaturated vapors," *Annalen der Physik*, vol. 24, no. 719, p. 146, 1935. 2.1.1.1

[9] Becker, R. and Döring, W., *Ferromagnetismus*. Springer, 1939. 2.1.1.1

[10] Bertsch, G., Onishi, N., and Yabana, K., "Magnetization of ferromagnetic clusters," *Zeitschrift für Physik D Atoms, Molecules and Clusters*, vol. 34, no. 3, pp. 213–217, 1995. 2.2.2, 2.2.2, 3.1, 3

[11] Beyer, M. and Knickelbein, M., "Electric deflection studies of rhodium clusters," *Journal of Chemical Physics*, vol. 126, no. 10, pp. 104301–104301, 2007. (document), 2.2.2, 4, 4, 4.24

[12] Billas, I. M. L., Becker, J., Châtelain, A., and de Heer, W. A., "Magnetic moments of iron clusters with 25 to 700 atoms and their dependence on temperature," *Physical Review Letters*, vol. 71, no. 24, pp. 4067–4070, 1993. 1.1, 4.4

[13] Billas, I., Châtelain, A., and de Heer, W. A., "Magnetism from the atom to the bulk in iron, cobalt, and nickel clusters," *Science*, vol. 265, no. 5179, p. 1682, 1994. 1.1, 4.4

[14] Blanc, J., Bonačić-Koutecký, V., Broyer, M., Chevaleyre, J., Dugourd, P., Koutecký, J., Scheuch, C., Wolf, J., and Wöste, L., "Evolution of the electronic structure of lithium clusters between four and eight atoms," *Journal of Chemical Physics*, vol. 96, p. 1793, 1992. 4.1

[15] Blundell, S., Guet, C., and Zope, R., "Temperature dependence of the polarizability of sodium clusters," *Physical Review Letters*, vol. 84, no. 21, pp. 4826–4829, 2000. 4.1.3

[16] Bobadova-Parvanova, P., Jackson, K., Srinivas, S., and Horoi, M., "Structure, bonding, and magnetism in manganese clusters," *Journal of Chemical Physics*, vol. 122, p. 014310, 2005. 4.4

[17] Bohr, A., Mottelson, B., and Pines, D., "Possible analogy between the excitation spectra of nuclei and those of the superconducting metallic state," *Physical Review*, vol. 110, no. 4, pp. 936–938, 1958. 4.1.1

[18] Bondybey, V. and English, J., "Laser induced fluorescence of metal clusters produced by laser vaporization: Gas phase spectrum of Pb," *Journal of Chemical Physics*, vol. 74, p. 6978, 1981. 2.1.1.2

[19] Borggreen, J., Chowdhury, P., Kebaili, N., Lundsbergnielsen, L., Lutzenkirchen, K., Nielsen, M., Pedersen, J., and Rasmussen, H., "Plasma excitations in charged sodium clusters," *Physical Review B*, vol. 48, pp. 17507–17516, Dec 15 1993. 4.1.1

[20] Borggreen, J., Hansen, K., Chandezon, F., Døssing, T., Elhajal, M., and Echt, O., "Absolute separation energies for Na clusters," *Physical Review A*, vol. 62, no. 1, p. 13202, 2000. 4.1.3

[21] Brack, M., "The physics of simple metal clusters: self-consistent jellium model and semiclassical approaches," *Reviews of Modern Physics*, vol. 65, no. 3, pp. 677–732, 1993. 4, 4.1

[22] Brown, J. and Carrington, A., *Rotational Spectroscopy of Diatomic Molecules*. Cambridge Univ Press, 2003. 4.2

[23] Broyer, M., Antoine, R., Benichou, E., Compagnon, I., Dugourd, P., and Rayane, D., "Structure of nano-objects through polarizability and dipole measurements," *Comptes Rendus-Physique*, vol. 3, no. 3, pp. 301–317, 2002. 2.2.2

[24] Broyer, M., Delacretaz, G., Labastie, P., Whetten, R., Wolf, J., and Wöste, L., "Spectroscopy of Na_3," *Zeitschrift für Physik D Atoms, Molecules and Clusters*, vol. 3, no. 2, pp. 131–136, 1986. 4.1.3

[25] Broyer, M., Delacretaz, G., Ni, G., Whetten, R., Wolf, J., and Wöste, L., "Vibronic structure of the Na_3 ground state by stimulated emission spectroscopy," *Physical Review Letters*, vol. 62, no. 18, pp. 2100–2103, 1989. 4.1.3

[26] Bucher, J. and Bloomfield, L., "Magnetism of Free Transition Metal and Rare Earth Clusters," *International Journal of Modern Physics B*, vol. 7, pp. 1079–1114, 1993. (document), 5.2.3, 5.11, 5.3

[27] Bulthuis, J., Becker, J., Moro, R., and Kresin, V., "Orientation of dipole molecules and clusters upon adiabatic entry into an external field," *Journal of Chemical Physics*, vol. 129, p. 024101, 2008. 3.1

[28] Bulusu, S., Li, X., Wang, L., and Zeng, X., "Evidence of hollow golden cages," *Proceedings of the National Academy of Sciences*, vol. 103, no. 22, p. 8326, 2006. 4.6

[29] Buot, F. and McClure, J., "Theory of Diamagnetism of Bismuth," *Physical Review B*, vol. 6, no. 12, pp. 4525–4533, 1972. 4.7

[30] Busani, R., Folkers, M., and Cheshnovsky, O., "Direct observation of band-gap closure in mercury clusters," *Physical Review Letters*, vol. 81, pp. 3836–3839, Nov 2 1998. 1.1

[31] Carpinelli, J., Weitering, H., Plummer, E., and Stumpf, R., "Direct observation of a surface charge density wave," 1996. 4

[32] Cerovski, V., Mahanti, S., and Khanna, S., "Magnetization of Gd_{13} cluster: Anomalous thermal behavior," *European Physical Journal D*, vol. 10, no. 1, pp. 119–122, 2000. (document), 5.2.1, 5.5, 5.6, 5.3, 5.13

[33] Cheng, H., Berry, R., and Whetten, R., "Electronic structure and binding energies of aluminum clusters," *Physical Review B*, vol. 43, no. 13, pp. 10647–10653, 1991. 4.3

[34] Clemenger, K., "Ellipsoidal shell structure in free-electron metal clusters," *Physical Review B*, vol. 32, no. 2, pp. 1359–1362, 1985. 4, 4.1

[35] Cox, A., Douglass, D., Louderback, J., Spencer, A., and Bloomfield, L., "Magnetic properties of rare earth clusters," *Zeitschrift für Physik D Atoms, Molecules and Clusters*, vol. 26, no. 1, pp. 319–321, 1993. 5.2.3, 5.3

[36] Cox, A., Louderback, J., Apsel, S., and Bloomfield, L., "Magnetism in 4d-transition metal clusters," *Physical Review B*, vol. 49, no. 17, pp. 12295–12298, 1994. (document), 1.1, 4.5.1, 4.21, 4.5.1

[37] Cox, A., Louderback, J., and Bloomfield, L., "Experimental observation of magnetism in rhodium clusters," *Physical Review Letters*, vol. 71, no. 6, pp. 923–926, 1993. 4.5.1, 4.5.1

[38] Cui, L., Li, X., and Wang, L., "Photoelectron spectroscopy of AlD (n= 3–15): Observation of chemisorption and physisorption of dideuterium on aluminum cluster anions," *Journal of chemical physics*, vol. 124, p. 054308, 2006. 4.3

[39] de Heer, W. A., "The physics of simple metal clusters: experimental aspects and simple models," *Reviews of Modern Physics*, vol. 65, no. 3, pp. 611–676, 1993. 1.1, 4.1, 4.1.1, 4.1.2

[40] de Heer, W. A. and Kresin, V. V., *Electric and Magnetic Dipole Moments of Free Nanoclusters*. CRC Press, 2010. 2.2.2

[41] de Heer, W., Milani, P., and Châtelain, A., "Nonjellium-to-jellium transition in aluminum cluster polarizabilities," *Physical Review Letters*, vol. 63, no. 26, pp. 2834–2836, 1989. (document), 4.3, 4.15

[42] DEHEER, W., SELBY, K., KRESIN, V., MASUI, J., VOLLMER, M., CHATELAIN, A., and KNIGHT, W., "Collective dipole oscillations in small sodium clusters," *PHYSICAL REVIEW LETTERS*, vol. 59, pp. 1805–1808, OCT 19 1987. 1.1, 4.1.1

[43] Dietz, T., Duncan, M., Powers, D., and Smalley, R., "Laser production of supersonic metal cluster beams," *Journal of Chemical Physics*, vol. 74, pp. 6511–6512, 1981. 2.1.1.2

[44] Douglass, D., Bucher, J., and Bloomfield, L., "Magic numbers in the magnetic properties of gadolinium clusters," *Physical Review Letters*, vol. 68, no. 11, pp. 1774–1777, 1992. 5.3

[45] Douglass, D., Cox, A., Bucher, J., and Bloomfield, L., "Magnetic properties of free cobalt and gadolinium clusters," *Physical Review B*, vol. 47, no. 19, pp. 12874–12889, 1993. 5.3

[46] Doye, J., "A model metal potential exhibiting polytetrahedral clusters," *Journal of Chemical Physics*, vol. 119, p. 1136, 2003. (document), 3.10

[47] Doye, J. and Wales, D., "Polytetrahedral clusters," *Physical Review Letters*, vol. 86, no. 25, pp. 5719–5722, 2001. (document), 3.10

[48] Dugourd, P., Antoine, R., El Rahim, M., Rayane, D., Broyer, M., and Calvo, F., "Molecular dynamics simulations of molecular beam deflection experiments," *Chemical Physics Letters*, vol. 423, no. 1-3, pp. 13–16, 2006. 2.2.2, 3, 4.5.1

[49] Dugourd, P., Compagnon, I., Lepine, F., Antoine, R., Rayane, D., and Broyer, M., "Beam deviation of large polar molecules in static electric fields: theory and experiment," *Chemical Physics Letters*, vol. 336, no. 5-6, pp. 511–517, 2001. 2.2.2, 3.1, 3

[50] Ekstrom, C., Schmiedmayer, J., Chapman, M., Hammond, T., and Pritchard, D., "Measurement of the electric polarizability of sodium with an atom interferometer," *Physical Review A*, vol. 51, no. 5, pp. 3883–3888, 1995. (document), 4.1

[51] El Rahim, M., Antoine, R., Broyer, M., Rayane, D., and Dugourd, P., "Asymmetric top rotors in electric fields: Influence of chaos and collisions in molecular beam deflection experiments," *J. Phys. Chem. A*, vol. 109, no. 38, pp. 8507–8514, 2005. 2.2.2, 3, 4.2, 4.5.1

[52] Fielicke, A., Kirilyuk, A., Ratsch, C., Behler, J., Scheffler, M., von Helden, G., and Meijer, G., "Structure determination of isolated metal clusters via far-infrared spectroscopy," *Physical Review Letters*, vol. 93, Jul 9 2004. 1.1, 4.2.1

[53] Fielicke, A., Ratsch, C., von Helden, G., and Meijer, G., "The far-infrared spectra of neutral and cationic niobium clusters," *Journal of Chemical Physics*, vol. 127, p. 234306, 2007. 4.2.1

[54] Fielicke, A., von Helden, G., and Meijer, G., "Far-infrared spectroscopy of isolated transition metal clusters," *EUROPEAN PHYSICAL JOURNAL D*, vol. 34, pp. 83–88, JUL 2005. 1.1

[55] Finnis, M. and Sinclair, J., "A simple empirical N-body potential for transition metals," *Philosophical magazine. A.*, vol. 50, no. 1, pp. 45–55, 1984. (document), 3.9

[56] Flynn, T. M., *Cryogenic Engineering*. CRC Press, 2005. 2.1.1.3

[57] Friedrich, B., Pullman, D., and Herschbach, D., "Alignment and orientation of rotationally cool molecules," *Journal of Physical Chemistry*, vol. 95, no. 21, pp. 8118–8129, 1991. 3.1

[58] Gerhardt, P., Niemietz, M., Dok Kim, Y., and Ganteför, G., "Fast electron dynamics in small aluminum clusters: non-magic behavior of a magic cluster," *Chemical Physics Letters*, vol. 382, no. 3-4, pp. 454–459, 2003. 4.3

[59] Gerion, D., Hirt, A., and Châtelain, A., "High Curie temperature and possible canted magnetism in free Gd clusters," *Physical Review Letters*, vol. 83, no. 3, pp. 532–535, 1999. 5.3

[60] Goldstein, H., Poole, C., and Safko, J., *Classical Mechanics, 3/e*. Pearson Education. 2.2.2, 2, 3

[61] Gruene, P., Fielicke, A., and Meijer, G., "Experimental vibrational spectra of gas-phase tantalum cluster cations," *Journal of Chemical Physics*, vol. 127, p. 234307, 2007. 4.2.1

[62] Gruene, P., Fielicke, A., Meijer, G., and Rayner, D. M., "The adsorption of co on group 10 (ni, pd, pt) transition-metal clusters," *Physical Chemistry Chemical Physics*, vol. 10, no. 40, pp. 6144–6149, 2008. 1.1

[63] Gruene, P., Rayner, D. M., Redlich, B., van der Meer, A. F. G., Lyon, J. T., Meijer, G., and Fielicke, A., "Structures of neutral au_7, au_{19}, and au_{20} clusters in the gas phase," *Science*, vol. 321, pp. 674–676, AUG 1 2008. (document), 1.1, 4.6, 4.28

[64] Grüner, G., *Density waves in solids*. Westview Press, 2000. 4

[65] Guirado-López, R., Dorantes-Dávila, J., and Pastor, G., "Orbital magnetism in transition-metal clusters: From hundś rules to bulk quenching," *Physical Review Letters*, vol. 90, no. 22, p. 226402, 2003. 4, 4.4

[66] Haberland, H., Hippler, T., Donges, J., Kostko, O., Schmidt, M., and von Issendorff, B., "Melting of sodium clusters: Where do the magic numbers come from?," *Physical Review Letters*, vol. 94, no. 3, 2005. 4.1.1

[67] Häkkinen, H., Kolehmainen, J., Koskinen, M., Lipas, P., and Manninen, M., "Universal shapes of small fermion clusters," *Physical Review Letters*, vol. 78, no. 6, pp. 1034–1037, 1997. 4.1.1, 6.1.1

[68] Häkkinen, H., Moseler, M., and Landman, U., "Bonding in Cu, Ag, and Au clusters: relativistic effects, trends, and surprises," *Physical Review Letters*, vol. 89, no. 3, p. 33401, 2002. 4.6

[69] Hakkinen, H., Yoon, B., Landman, U., Li, X., Zhai, H., and Wang, L., "On the electronic and atomic structures of small au_N^- ($n = 4 - 14$) clusters: A photoelectron spectroscopy and density-functional study," *Journal of Physical Chemistry A*, vol. 107, pp. 6168–6175, AUG 14 2003. 1.1, 4.6

[70] Harding, D., Ford, M., Walshab, T., and Mackenziew, S., "Dramatic size effects and evidence of structural isomers in the reactions of rhodium clusters, Rh_N, with nitrous oxide," *Physical Chemistry Chemical Physics*, vol. 9, pp. 2130–2136, 2007. (document), 1.1, 4.5.3, 4.5.3, 4.25

[71] Herzberg, G. and Longuet-Higgins, H., "Intersection of potential energy surfaces in polyatomic molecules," *Discussions of the Faraday Society*, vol. 35, pp. 77–82, 1963. 4.1.3

[72] Hishinuma, N., "Observation of molecular-beam magnetic resonance of Li_N clusters," *Physical Review A*, vol. 46, no. 11, pp. 7023–7027, 1992. 4.1.3

[73] Hock, C., Bartels, C., Strassburg, S., Schmidt, M., Haberland, H., von Issendorff, B., and Aguado, A., "Premelting and postmelting in clusters," *Physical Review Letters*, vol. 102, JAN 30 2009. 4.1.1

[74] Hoffmann, R., "A chemical and theoretical way to look at bonding on surfaces," *Reviews of Modern Physics*, vol. 60, no. 3, pp. 601–628, 1988. 1.2.1

[75] Hofmann, P., "The surfaces of bismuth: Structural and electronic properties," *Progress in Surface Science*, vol. 81, no. 5, pp. 191–245, 2006. 4.7

[76] Honea, E., Homer, M., Persson, J., and Whetten, R., "Generation and photoionization of cold Na_N clusters; N to 200," *Chemical Physics Letters*, vol. 171, no. 3, pp. 147–154, 1990. 1.1, 4.1.1, 4.1.2

[77] Jackson, J. D., *Classical Electrodynamics 3rd ed.* John Wiley & Sons Inc., 1999. 4.5.3

[78] Jensen, J. and Mackintosh, A., *Rare earth magnetism*. Clarendon, 1991. (document), 5.1, 5.2.1, 5.4, 5.1

[79] Jones, R. O., "Structure and bonding in small aluminum clusters," *Physical Review Letters*, vol. 67, no. 2, pp. 224–227, 1991. 4.3

[80] Khanna, S. and Linderoth, S., "Magnetic behavior of clusters of ferromagnetic transition metals," *Physical Review Letters*, vol. 67, no. 6, pp. 742–745, 1991. 4, 4.4

[81] Khanna, S., Rao, B., Jena, P., and Knickelbein, M., "Ferrimagnetism in Mn_7 cluster," *Chemical Physics Letters*, vol. 378, no. 3-4, pp. 374–379, 2003. 4.4

[82] Kietzmann, H., Morenzin, J., Bechthold, P., Ganteför, G., and Eberhardt, W., "Photoelectron spectra of Nb clusters: Correlation between electronic structure and hydrogen chemisorption," *Journal of Chemical Physics*, vol. 109, p. 2275, 1998. 4.2.1

[83] Kietzmann, H., Morenzin, J., Bechthold, P., Ganteför, G., Eberhardt, W., Yang, D., Hackett, P., Fournier, R., Pang, T., and Chen, C., "Photoelectron spectra and geometric structures of small niobium cluster anions," *Physical Review Letters*, vol. 77, no. 22, pp. 4528–4531, 1996. 4.2.1

[84] Knickelbein, M., "Reactions of transition metal clusters with small molecules," *Annual Review of Physical Chemistry*, vol. 50, pp. 79–115, 1999. 1.1, 4.4, 4.5.3, 4.6

[85] Knickelbein, M., "Electric dipole polarizabilities of Ni," *Journal of Chemical Physics*, vol. 115, p. 5957, 2001. (document), 4, 4.16, 4.4

[86] Knickelbein, M., "Experimental observation of superparamagnetism in manganese clusters," *Physical Review Letters*, vol. 86, no. 23, pp. 5255–5257, 2001. 4.4

[87] Knickelbein, M., "Electric dipole polarizabilities of Nb2-27," *Journal of Chemical Physics*, vol. 118, no. 14, pp. 6230–6233, 2003. 4, 4.2.1

[88] Knickelbein, M., "Electric dipole polarizabilities of copper clusters," *Journal of Chemical Physics*, vol. 120, p. 10450, 2004. 2.2.2, 4

[89] Knickelbein, M., "Magnetic ordering in manganese clusters," *Physical Review B*, vol. 70, no. 1, p. 14424, 2004. 1.1, 4.4

[90] Knickelbein, M. and Menezes, W., "Optical response of small niobium clusters," *Physical Review Letters*, vol. 69, no. 7, pp. 1046–1049, 1992. 4.2.1

[91] Knight, W., Clemenger, K., de Heer, W., and Saunders, W., "Polarizability of alkali clusters," *Physical Review B*, vol. 31, no. 4, pp. 2539–2540, 1985. (document), 4, 4.1.1, 4.4, 4.1.3

[92] Knight, W., Clemenger, K., de Heer, W., Saunders, W., Chou, M., and Cohen, M., "Electronic shell structure and abundances of sodium clusters," *Physical Review Letters*, vol. 52, no. 24, pp. 2141–2143, 1984. (document), 1.1, 4.1, 4.1.1, 4.2

[93] Kostko, O., Huber, B., Moseler, M., and von Issendorff, B., "Structure determination of medium-sized sodium clusters," *Physical Review Letters*, vol. 98, no. 4, p. 43401, 2007. 4.1.1, 4.1.3

[94] Kubo, R., "Electronic properties of metallic fine particles," *J. Phys. Soc. Jpn*, vol. 17, p. 975, 1962. 1.1, 1.2.3

[95] Kummerlöwe, G. and Beyer, M., "Rate estimates for collisions of ionic clusters with neutral reactant molecules," *International Journal of Mass Spectrometry*, vol. 244, no. 1, pp. 84–90, 2005. 1.2.2, 4.5.3

[96] Kusche, R., Hippler, T., Schmidt, M., von Issendorff, B., and Haberland, H., "Melting of free sodium clusters," *European Physical Journal D*, vol. 9, pp. 1–4, DEC 1999. 4.1.1

[97] Lang, N. and Kohn, W., "Theory of metal surfaces: Charge density and surface energy," *Physical Review B*, vol. 1, no. 12, pp. 4555–4568, 1970. 4

[98] Li, X., Wu, H., Wang, X., and Wang, L., "s-p Hybridization and Electron Shell Structures in Aluminum Clusters: A Photoelectron Spectroscopy Study," *Physical Review Letters*, vol. 81, no. 9, pp. 1909–1912, 1998. 1.1

[99] Link, S., El-Sayed, M., Gregory Schaaff, T., and Whetten, R., "Transition from nanoparticle to molecular behavior: a femtosecond transient absorption study of a size-selected 28 atom gold cluster," *Chemical Physics Letters*, vol. 356, no. 3-4, pp. 240–246, 2002. 1.1

[100] Liu, S., Zhai, H., and Wang, L., "Electronic and structural evolution of Co_N clusters ($N = 1 - 108$) by photoelectron spectroscopy," *Physical Review B*, vol. 64, no. 15, p. 153402, 2001. 1.1, 4.4

[101] Longuet-Higgins, H., "The intersection of potential energy surfaces in polyatomic molecules," *Proceedings of the Royal Society of London. Series A*, vol. 344, no. 1637, pp. 147–156, 1975. 4.1.3

[102] López-Urías, F., Díaz-Ortiz, A., and Morán-López, J., "Magnetism at finite temperature in heavy rare-earth clusters," *Physical Review B*, vol. 66, no. 14, p. 144406, 2002. 5.3

[103] Lyon, J. T., Gruene, P., Fielicke, A., Meijer, G., and Rayner, D. M., "Probing c-o bond activation on gas-phase transition metal clusters: Infrared multiple photon dissociation spectroscopy of fe, ru, re, and w cluster co complexes," *JOURNAL OF CHEMICAL PHYSICS*, vol. 131, NOV 14 2009. 4.6

[104] Ma, L., Issendorff, B., and Aguado, A., "Photoelectron spectroscopy of cold aluminum cluster anions: Comparison with density functional theory results," *Journal of Chemical Physics*, vol. 132, p. 104303, 2010. 1.1, 4.3

[105] Martin, T., Bjørnholm, S., Borggreen, J., Bréchignac, C., Cahuzac, P., Hansen, K., and Pedersen, J., "Electronic shell structure of laser-warmed Na clusters," *Chemical Physics Letters*, vol. 186, no. 1, pp. 53–57, 1991. 4.1.1, 4.1.2

[106] Matveentsev, A., Lyalin, A., and Solov'yov, I., "On the applicability of the jellium model to the description of alkali clusters.," *International Journal of Modern Physics E*, vol. 12, no. 1, pp. 81–107, 2003. 4.1

[107] Milani, P., De Heer, W., and Châtelain, A., "Electronic properties of aluminum clusters compared with the jellium model," *Zeitschrift für Physik D Atoms, Molecules and Clusters*, vol. 19, no. 1, pp. 133–135, 1991. 4.3

[108] Milani, P. and de Heer, W., "Relative thermometer for neutral clusters produced in laser-vaporization sources," *Physical Review B*, vol. 44, no. 15, pp. 8346–8348, 1991. 3.6

[109] Milani, P. and Deheer, W., "Improved pulsed laser vaporization source for production of intense beams of neutral and ionized clusters," *Review of Scientific Instruments*, vol. 61, no. 7, pp. 1835–1838, 1990. 2.1.1.2

[110] Milani, P., Moullet, I., and de Heer, W., "Experimental and theoretical electric dipole polarizabilities of Al and Al_2," *Physical Review A*, vol. 42, no. 9, pp. 5150–5154, 1990. (document), 4.1, 4.15

[111] Moro, R., Xu, X., Yin, S., and de Heer, W., "Ferroelectricity in free niobium clusters," *Science*, vol. 300, no. 5623, p. 1265, 2003. 2.2.2, 4.2, 4.2

[112] Moro, R., Yin, S., Xu, X., and de Heer, W., "Spin uncoupling in free Nb clusters: Support for nascent superconductivity," *Physical Review Letters*, vol. 93, no. 8, p. 86803, 2004. 4.2, 4.2

[113] Mott, N., "Metal-insulator transition," *Reviews of Modern Physics*, vol. 40, no. 4, pp. 677–683, 1968. 1.2.1

[114] Pappas, D., Popov, A., Anisimov, A., Reddy, B., and Khanna, S., "Spin Configuration of Gd_{13} Clusters," *Physical Review Letters*, vol. 76, no. 23, pp. 4332–4335, 1996. (document), 5.2.1, 5.6, 5.3, 5.12, 5.13, 5.4.1

[115] Parguez, G., Natali, F., and Brown, S., "Oxidation of bismuth cluster films," *Current Applied Physics*, vol. 8, no. 3-4, pp. 287–290, 2008. 4.7

[116] Parks, E., Nieman, G., Kerns, K., and Riley, S., "Reactions of Ni_{38} with N_2, H_2, and CO: Cluster structure and adsorbate binding sites," *Journal of Chemical Physics*, vol. 107, no. 6, p. 1861, 1997. 1.1

[117] Parks, E., Zhu, L., Ho, J., and Riley, S., "The structure of small nickel clusters. I. Ni_3-Ni_{15}," *J. Chem. Phys*, vol. 100, p. 7206, 1994. 1.1

[118] Pastor, G., Dorantes-Dávila, J., Pick, S., and Dreyssé, H., "Magnetic anisotropy of 3d transition-metal clusters," *Physical Review Letters*, vol. 75, no. 2, pp. 326–329, 1995. 4, 4.4

[119] Pastor, G., Hirsch, R., and Mühlschlegel, B., "Electron correlations, magnetism, and structure of small clusters," *Physical Review Letters*, vol. 72, no. 24, pp. 3879–3882, 1994. 4, 4.4

[120] Pedersen, J., Bjørnholm, S., Borggreen, J., Hansen, K., Martin, T., and Rasmussen, H., "Observation of quantum supershells in clusters of sodium atoms," *Nature*, vol. 353, no. 6346, pp. 733–735, 1991. 1.1, 4.1.1

[121] Persson, J., Whetten, R., Cheng, H., and Berry, R., "Evidence for quantized electronic level structure for 100-1300 electrons in metal-atomic clusters," *Chemical Physics Letters*, vol. 186, no. 2-3, pp. 215–222, 1991. 4.3

[122] Pokrant, S., "Evidence for adiabatic magnetization of cold Dy_N Clusters," *Physical Review A*, vol. 62, no. 5, p. 51201, 2000. 5.3

[123] Pokrant, S. and Becker, J., "Magnetization curves of Dy clusters," *European Physical Journal D*, vol. 16, no. 1-3, pp. 165–168, 2001. 5.3

[124] Puska, M., Nieminen, R., and Manninen, M., "Electronic polarizability of small metal spheres," *Physical Review B*, vol. 31, no. 6, pp. 3486–3495, 1985. 4.1.3

[125] Pyykkö, P., "Theoretical chemistry of gold," *Angewandte Chemie International Edition*, vol. 43, no. 34, pp. 4412–4456, 2004. 4.6

[126] Ramsey, N., *Molecular beams*. Oxford University Press London, 1997. 2.1.4

[127] Rao, B. and Jena, P., "Evolution of the electronic structure and properties of neutral and charged aluminum clusters: A comprehensive analysis," *Journal of Chemical Physics*, vol. 111, p. 1890, 1999. 4.3

[128] Ratsch, C., Fielicke, A., Kirilyuk, A., Behler, J., von Helden, G., Meijer, G., and Scheffler, M., "Structure determination of small vanadium clusters by density-functional theory in comparison with experimental far-infrared spectra," *Journal of Chemical Physics*, vol. 122, no. 12, 2005. 4.2.1

[129] Rayane, D., Allouche, A., Benichou, E., Antoine, R., Aubert-Frecon, M., Dugourd, P., Broyer, M., Ristori, C., Chandezon, F., Huber, B., and others, "Static electric dipole polarizabilities of alkali clusters," *European Physical Journal D*, vol. 9, no. 1, pp. 243–248, 1999. 4, 4.1.3

[130] Reddy, B., Khanna, S., and Dunlap, B., "Giant magnetic moments in 4d clusters," *Physical Review Letters*, vol. 70, no. 21, pp. 3323–3326, 1993. 4.5.1

[131] Richtsmeier, S., Parks, E., Liu, K., Pobo, L., and Riley, S., "Gas phase reactions of iron clusters with hydrogen. I. Kinetics," *Journal of Chemical Physics*, vol. 82, p. 3659, 1985. 1.1

[132] Saunders, W., Clemenger, K., de Heer, W., and Knight, W., "Photoionization and shell structure of potassium clusters," *Physical Review B*, vol. 32, no. 2, pp. 1366–1368, 1985. 1.1

[133] Schäfer, S., Assadollahzadeh, B., Mehring, M., Schwerdtfeger, P., and Schäfer, R., "Structure and Electric Properties of Sn_N Clusters ($N = 6 - 20$) from Combined Electric Deflection Experiments and Quantum Theoretical Studies," *Journal of Physical Chemistry A*, vol. 112, no. 48, pp. 12312–12319, 2008. 2.2.2, 4, 4, 6.1.2

[134] Schäfer, S., Heiles, S., Becker, J., and Schäfer, R., "Electric deflection studies on lead clusters," *Journal of Chemical Physics*, vol. 129, p. 044304, 2008. 1.2.6, 3(b), 2.2.2, 4, 4

[135] Schäfer, S. and Schäfer, R., "Dielectric response of germanium clusters," *Physical Review B*, vol. 77, no. 20, p. 205211, 2008. 2.2.2, 4, 4

[136] Schmidt, M. and Haberland, H., "Optical spectra and their moments for sodium clusters, Na_n^+, with $3 \leq n \leq 64$," *European Physical Journal D*, vol. 6, no. 1, pp. 109–118, 1999. 4.1.1, 4.1.1, 4.1.3

[137] Schmidt, M., Kusche, R., Kronmuller, W., von Issendorff, B., and Haberland, H., "Experimental determination of the melting point and heat capacity for a free cluster of 139 sodium atoms," *Physical Review Letters*, vol. 79, no. 1, pp. 99–102, 1997. 4.1.1

[138] Schmidt, M., Kusche, R., Von Issendorff, B., and Haberland, H., "Irregular variations in the melting point of size-selected atomic clusters," *Nature*, vol. 393, no. 6682, pp. 238–240, 1998. 4.1.1

[139] Schnell, M., Herwig, C., and Becker, J., "Analysis of Semiconductor Cluster Beam Polarization Taking Small Permanent Dipole Moments into Account," *Zeitschrift für Physikalische Chemie*, vol. 217, no. 8, pp. 1003–1030, 2003. 3.1

[140] Schriver, K., Persson, J., Honea, E., and Whetten, R., "Electronic shell structure of group-IIIA metal atomic clusters," *Physical Review Letters*, vol. 64, no. 21, pp. 2539–2542, 1990. 1.1, 4.3

[141] Schulze, M., Gourley, S., Brown, S., Dunbar, A., Partridge, J., and Blaikie, R., "Electrical measurements of nanoscale bismuth cluster films," *European Physical Journal D*, vol. 24, no. 1, pp. 291–294, 2003. 4.7

[142] Selby, K., Kresin, V., Masui, J., Vollmer, M., de Heer, W., Scheidemann, A., and Knight, W., "Photoabsorption spectra of sodium clusters," *Physical Review B*, vol. 43, no. 6, pp. 4565–4572, 1991. 1.1, 4.1.1

[143] Selby, K., Vollmer, M., Masui, J., Kresin, V., de Heer, W., and Knight, W., "Surface plasma resonances in free metal clusters," *Physical Review B*, vol. 40, no. 8, pp. 5417–5427, 1989. 1.1, 4.1.1

[144] Senz, V., Fischer, T., Oelssner, P., Tiggesbäumker, J., Stanzel, J., Bostedt, C., Thomas, H., Schöffler, M., Foucar, L., Martins, M., and others, "Core-hole screening as a probe for a metal-to-nonmetal transition in lead clusters," *Physical Review Letters*, vol. 102, no. 13, p. 138303, 2009. 1.2.6, 3(a)

[145] Smirnov, B. M., *Plasma Processes and Plasma Kinetics*. Wiley, 2007. 2.1.1.1, 4.1.2

[146] Solov'yov, I., Solov'yov, A., and Greiner, W., "Structure and properties of small sodium clusters," *Physical Review A*, vol. 65, no. 5, p. 53203, 2002. (document), 4.1, 4.7, 4.1.3

[147] Taylor, K. and Darby, M., *Physics of rare earth solids*. Chapman and Hall, 1972. (document), 5.4, 5.1

[148] Thomas, O., Zheng, W., Xu, S., and Bowen Jr, K., "Onset of metallic behavior in magnesium clusters," *Physical Review Letters*, vol. 89, no. 21, p. 213403, 2002. 1.1, 1.2.3

[149] Tikhonov, G., Kasperovich, V., Wong, K., and Kresin, V., "A measurement of the polarizability of sodium clusters," *Physical Review A*, vol. 64, no. 6, p. 63202, 2001. (document), 4, 4.1.1, 4.4, 4.1.3

[150] Townes, C. and Schawlow, A., *Microwave spectroscopy*. Dover, 1975. 4

[151] van den Brink, J. and Khomskii, D., "Multiferroicity due to charge ordering," *Journal of Physics: Condensed Matter*, vol. 20, p. 434217, 2008. 4

[152] Vega, A., Dorantes-Davila, J., Balbas, L., and Pastor, G., "Calculated sp-electron and spd-hybridization effects on the magnetic properties of small Fe_N clusters," *Physical Review B*, vol. 47, no. 8, pp. 4742–4746, 1993. 4, 4.4

[153] von Issendorff, B. and Cheshnovsky, O., "Metal to insulator transitions in clusters.," *Annual Review of Physical Chemistry*, vol. 56, p. 549, 2005. (document), 1.2.3, 1.2.3, 1.1

[154] Wales, D. J., *Energy Landscapes*. Cambridge University Press, 2003. 4

[155] Weast, R. C. R. C., *CRC handbook of chemistry and physics*. CRC press Boca Raton, FL, 1988. 4

[156] Whetten, R., Cox, D., Trevor, D., and Kaldor, A., "Correspondence between electron binding energy and chemisorption reactivity of iron clusters," *Physical Review Letters*, vol. 54, no. 14, pp. 1494–1497, 1985. 1.1

[157] Whetten, R., Zakin, M., Cox, D., Trevor, D., and Kaldor, A., "Electron binding and chemical inertness of specific Nb clusters," *Journal of Chemical Physics*, vol. 85, p. 1697, 1986. 1.1

[158] Wiley, W. and McLaren, I., "Time-of-Flight Mass Spectrometer with Improved Resolution," *Review of Scientific Instruments*, vol. 26, p. 1150, 1955. 2.1.5.1

[159] Wolf, J., Delacrétaz, G., and Wöste, L., "First observation of an electronically excited state of Li_3," *Physical Review Letters*, vol. 63, no. 18, pp. 1946–1949, 1989. 4.1.3

[160] Wong, K., Vongehr, S., and Kresin, V., "Work functions, ionization potentials, and in between: Scaling relations based on the image-charge model," *Physical Review B*, vol. 67, no. 3, p. 35406, 2003. 1.1

[161] Wrigge, G., Hoffmann, M., and Issendorff, B., "Photoelectron spectroscopy of sodium clusters: Direct observation of the electronic shell structure," *Physical Review A*, vol. 65, no. 6, p. 63201, 2002. 4.1.1

[162] Wrigge, G., Hoffmann, M., von Issendorff, B., and Haberland, H., "Ultraviolet photoelectron spectroscopy of nb-4(-) to nb-200(-)," *EUROPEAN PHYSICAL JOURNAL D*, vol. 24, pp. 23–26, JUN 2003. 4.2.1

[163] Wu, H., Desai, S., and Wang, L., "Evolution of the electronic structure of small vanadium clusters from molecular to bulklike," *Physical Review Letters*, vol. 77, no. 12, pp. 2436–2439, 1996. 1.1

[164] Wurl, A., Hyslop, M., Brown, S., Hall, B., and Monot, R., "Structure of unsupported bismuth nanoparticles," *European Physical Journal D*, vol. 16, no. 1, pp. 205–208, 2001. 4.7

[165] Xia, C., Yin, C., and Kresin, V., "Photoabsorption by Volume Plasmons in Metal Nanoclusters," *Physical Review Letters*, vol. 102, no. 15, p. 156802, 2009. 1.1, 4.1.1

[166] Xing, X., Yoon, B., Landman, U., and Parks, J., "Structural evolution of Au nanoclusters: From planar to cage to tubular motifs," *Physical Review B*, vol. 74, no. 16, p. 165423, 2006. 1.1, 4.6

[167] Xu, X., Yin, S., Moro, R., and de Heer, W., "Magnetic moments and adiabatic magnetization of free cobalt clusters," *Physical Review Letters*, vol. 95, no. 23, p. 237209, 2005. 3.1, 4.5.1

[168] Xu, X., Yin, S., Moro, R., and de Heer, W., "Distribution of magnetization of a cold ferromagnetic cluster beam," *Physical Review B*, vol. 78, no. 5, p. 54430, 2008. (document), 3.1, 3.5, 3.11, 4.5.1, 4.5.1

[169] Xu, X., Yin, S., Moro, R., Liang, A., Bowlan, J., and de Heer, W., "Nonclassical dipoles in cold niobium clusters," *Physical Review B*, vol. 75, no. 8, p. 85429, 2007. 4.2, 4.2, 4.2

[170] Yannouleas, C., Broglia, R., Brack, M., and Bortignon, P., "Fragmentation of the photoabsorption strength in neutral and charged metal microclusters," *Physical Review Letters*, vol. 63, no. 3, pp. 255–258, 1989. 4.1.1

[171] Yi, J., Oh, D., Bernholc, R., and others, "Structural transitions in aluminum clusters," *Chemical Physics Letters*, vol. 174, no. 5, pp. 461–466, 1990. 4.3

[172] Yin, S., Xu, X., Liang, A., Bowlan, J., Moro, R., and de Heer, W., "Electron Pairing in Ferroelectric Niobium and Niobium Alloy Clusters," *Journal of Superconductivity and Novel Magnetism*, vol. 21, no. 5, pp. 265–269, 2008. (document), 4.2, 4.2, 4.2, 4.2.2, 4.12

[173] Yoon, B., Hakkinen, H., Landman, U., Worz, A., Antonietti, J., Abbet, S., Judai, K., and Heiz, U., "Charging effects on bonding and catalyzed oxidation of co on au_8 clusters on mgo," *Science*, vol. 307, no. 5708, pp. 403–407, 2005. 1.1, 4.6

[174] Yoon, B., Koskinen, P., Huber, B., Kostko, O., von Issendorff, B., Hakkinen, H., Moseler, M., and Landman, U., "Size-dependent structural evolution and chemical reactivity of gold clusters," *ChemPhysChem*, vol. 8, no. 1, pp. 157–161, 2007. 4.6

[175] Yoon, B. and Landman, U., "Electric field control of structure, dimensionality, and reactivity of gold nanoclusters on metal-supported mgo films," *PHYSICAL REVIEW LETTERS*, vol. 100, FEB 8 2008. 4.6

[176] Zheng, J., Nicovich, P., and Dickson, R., "Highly fluorescent noble-metal quantum dots.," *Annual review of physical chemistry*, vol. 58, p. 409, 2007. 4.6

VITA

John Bowlan was born May 31 1980 in Memphis TN.